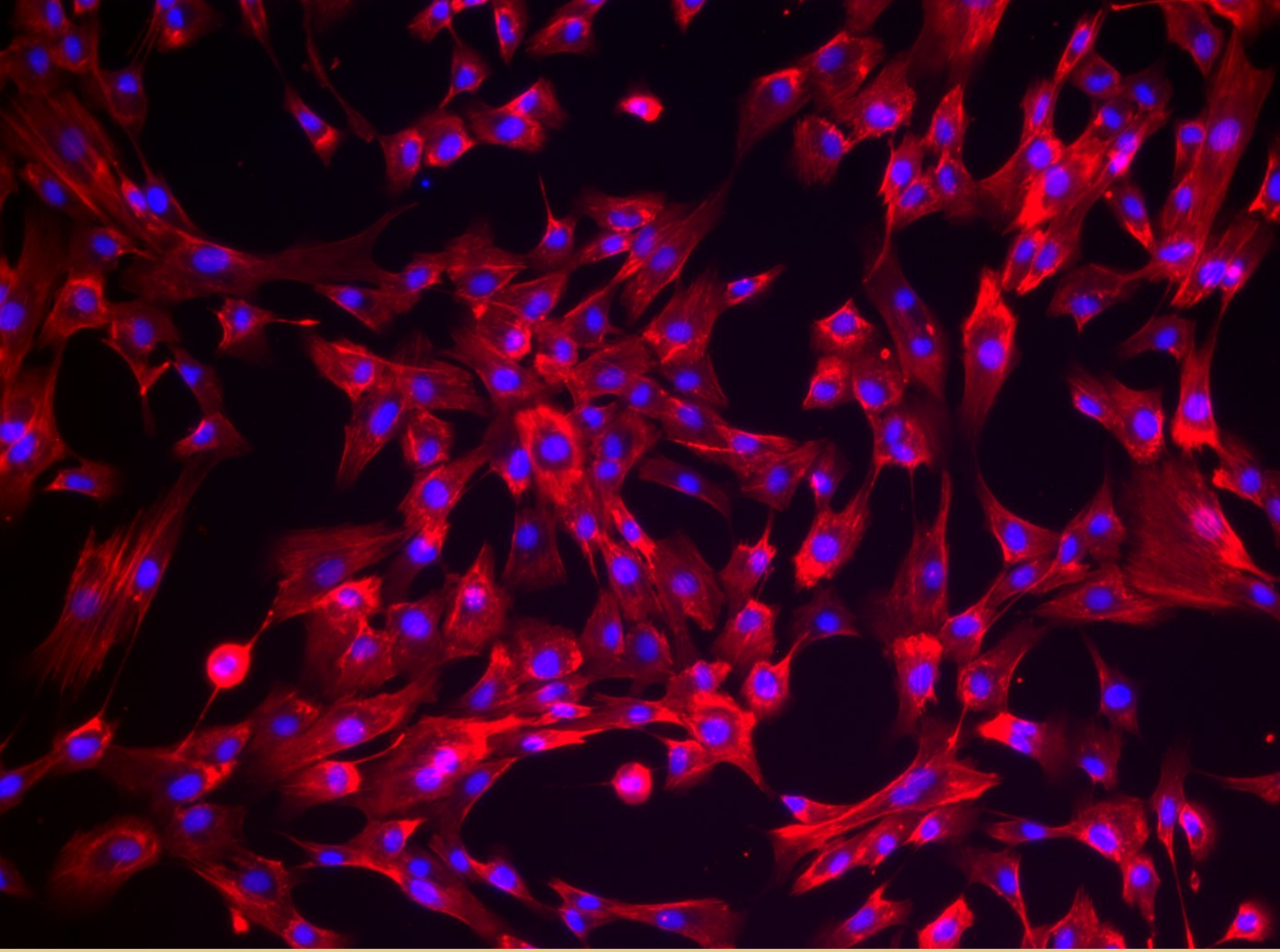

João Ramos

Mechanically-Driven Pattern Formation in Cell Cultures

Dissertation presented to the Physics Department at the University of Coimbra to obtain the Master's degree in Physics.

October of 2016

· U C ·

Universidade de Coimbra

Cover Figure: Human fibroblasts with stained actin filaments (red) and nucleus (blue). Image adapted from http://spirochrome.com/product/cytoskeleton-kit/.

• U C •

FCTUC FACULDADE DE CIÊNCIAS
E TECNOLOGIA
UNIVERSIDADE DE COIMBRA

João Ramos

Mechanically-Driven Pattern Formation in Cell Cultures

Dissertation presented to the University of Coimbra in fulfilment of the requirements necessary for obtaining a MSc degree in Physics.

Supervisors:

João Carvalho (CFisUC)

Rui Travasso (CFisUC)

Coimbra, 2016

This project was developed in collaboration with:

CFisUC

Dedicated to my family and friends...

Acknowledgements

Foremost, I would like to express my gratitude for the support, motivation and guidance given to me by my thesis advisors, Prof. João Carvalho and Prof. Rui Travasso, throughout the endeavor underlying this project. Their patience, attention and enthusiasm were pivotal in researching and writing this thesis.

Next, I would like to thank CFisUC for allowing me to use the Navigator cluster without which this work would not have been possible.

Furthermore, I would like to thank my colleagues in the Biological Physics group, with whom I have had the pleasure to work, for all the interesting questions raised and the fruitful discussions had. I would also like to thank my fellow students for their wholehearted company and encouragement. Additionally, I would like to express my gratitude to all my friends, regardless of how far they may be, for their friendship and reassurance.

Last but not least, I would like to express my gratitude to my family for their unrestrained love and support.

"*Complexity is the prodigy of the world. Simplicity is the sensation of the universe. Behind complexity, there is always simplicity to be revealed. Inside simplicity, there is always complexity to be discovered.*"

Gang Yu

Abstract

Cell migration is a fundamental mechanism which enables several biological phenomena, for example, embryogenesis, vasculogenesis, angiogenesis and immune system response, to occur and it is still not fully understood. Complications and diseases often arise from faults during this process. Effectively, cell migration is a hallmark of malignant cancer cells. By studying emergent patterns of cells, it is possible to shed light on this mechanism. Here, a hybrid two-dimensional (2D) model of cell dynamics couples a finite element method (FEM), for extracellular matrix (ECM) deformations, with a cellular Potts model (CPM), for cell movement and adhesion. A model for traction force generation and another for sensing mechanical environmental cues were used to couple the FEM to the CPM. This model was used to study mechanically-driven emergent cell behavior. Image analysis methods were adapted in order to classify and quantify the morphology of resulting patterns. In the context of vasculogenesis, results show that for certain values of cell-cell adhesion and cell traction force there is a maximum on the average number of meshes and that, by lowering cell-cell adhesion cost, the average mesh size increases, while the average number of meshes decreases. Furthermore, mechanical cues coupled with cell-cell adhesion were found to be able to pull multiple cells from a soft substrate into a stiffer substrate. Sprouting angiogenesis was also tested and, even though proliferation is not contemplated in the model, mechanical cues are enough to polarize cells on the surface of a spheroid and start forming sprouts. Cells with larger traction forces lead to longer sprouts, more bifurcations and observation of anastomosis, suggesting that tip cells have a stronger grip on the ECM. Finally, an avascular tumor was simulated. Mechanical feedback accounts for an uneven surface of the tumor. Metastatic cell invasion capabilities increase with traction force and mechanical cues resulting from those cells cause protrusions of normal tumor cells at the surface.

Resumo

A migração celular é um mecanismo fundamental que permite a ocorrência de vários fenómenos biológicos, como por exemplo, embriogénese, vasculogénese, angiogénese e resposta do sistema imunitário, e ainda não é compreendido na sua totalidade. Problemas durante este processo levam muitas vezes ao aparecimento de doenças e complicações. Efectivamente, a migração celular é uma das características distintas de células tumorais malignas. Ao estudar os padrões emergentes de células, é possível desvendar este processo. Um modelo bidimensional de dinâmica celular que une um método de elementos finitos (FEM), para deformações da matriz extracelular (ECM), a um modelo de Potts celular (CPM), para movimento e adesão celular. Um modelo para a produção de forças de tracção e outro para a detecção de sinais mecânicos foram usados para acoplar o FEM ao CPM. Este modelo foi usado para estudar comportamento celular emergente mecânicamente induzido. Métodos de análise de imagem foram adaptados a fim de classificar e quantificar a morfologia dos padrões resultantes. No contexto da vasculogénese, os resultados demonstram que, para certos valores de adesão célula-célula e de forças de tração, existe um valor máximo do número médio de malhas e que, ao diminuir o custo de adesão célula-célula, o tamanho médio de malhas aumenta, enquanto o número médio de malhas diminui. Além disso, sinais mecânicos, juntamente com adesão célula-célula, permitem que células num substrato mais duro puxem várias células do substrato mais mole. A angiogénese (*sprouting*) também foi testada e, apesar da proliferação celular não estar contemplada neste modelo, sinais mecânicos são suficientes para polarizar células à superfície do esferóide, formando *sprouts*. Células com maior força de tração conduzem a *sprouts* maiores, a mais bifurcações e à observação de anastomoses, sugerindo que as *tip cells* se agarram com mais força ao substrato. Finalmente, foi simulado um tumor avascular. O *feedback* mecânico prevê rugosidades à superfície do tumor. A capacidade de invasão de células metásticas aumenta com a força de tração e os sinais mecânicos causados por estas células induzem protrusões de células tumorais normais na superfície do tumor.

Contents

List of Figures

List of Tables

List of Abbreviations

ECM	**E**xtra**c**ellular **M**atrix
CAM	**C**ell **A**dhesion **M**olecule
FA	**F**ocal **A**dhesion
FEM	**F**inite **E**lement **M**ethod
CPM	**C**ellular **P**otts **M**odel
PCG	**P**reconditioned **C**onjugate **G**radient
CG	**C**onjugate **G**radient
MCMC	**M**arkov **C**hain **M**onte **C**arlo
CCA	**C**onnected **C**omponent **A**lgorithm
RNG	**R**andom **N**umber **G**enerator

Chapter 1

Introduction

1.1 Overview

Self-organization is the process by which components of an arbitrary system spontaneously rearrange in a dynamical steady state by local interactions and random fluctuations. These processes typically result from positive or negative feedback of such interactions and the steady state exhibits self-repair to a certain extent [1]. Therefore, self-organization of cell systems plays a fundamental role, not only in the development of a multicellular being, but also in its maintenance. Examples include morphogenesis of the embryo [2], such as the creation of a vascular network *de novo* (vasculogenesis) and from a pre-existing one (angiogenesis) [3] and tissue regeneration [4].

In fact, emergent phenomena of self-organization is the outcome of how cells communicate with each other [5] and with the surrounding environment [6], which is composed mainly of fibrous proteins, also called extracellular matrix (ECM). Specifically, cell communication is mediated through cell-cell adhesion and also by secreting signal molecules. On the other hand, cell-ECM interaction is achieved by focal adhesions (cell-matrix adhesion) through which cells can sense their environment, for example, the stiffness of the substrate and chemical composition.

In particular, because morphological changes require cell movement, cell-cell adhesion, in this context, must not bind two cells irreversibly and, thus, cell contacts must be regularly formed, broken and rearranged. Adhesion in general is performed by transmembrane molecules called CAMs (cell adhesion molecules). Cadherins, a family of molecules of said type, play a major role in mediating cell-cell interaction. In contrast, focal adhesions are comprised of large protein complexes generated by the contact of integrins (another family of CAMs) with the ECM. These complexes also attach to the cytoskeleton, therefore focal adhesions not only provide support for the cell, but can also regulate its behavior. In fact, the ability cells have for sensing tissue stiffness (mechanosensing) and regulating accordingly leads to the process called durotaxis [7], in which the cell migrates towards higher ECM stiffness. Furthermore, durotaxis and mechanosensing also play a role in cell polarization, which is the ability of a cell to transition from an isotropic and symmetric configuration to an anisotropic and asymmetric one.

Additionally, in order for the cell to remain attached to the ECM and maintain its shape

it needs to continuously pull on the substrate. Regulated by focal adhesions, traction forces refer to this phenomena and are also relevant in other processes such as cell movement.

All things considered, cell communication has a rather prevalent mechanical basis. Not only cells adhere to each other, but they also attach to the ECM. The latter implies that the cell applies traction forces on the substrate, deforming it. This leads to a feedback mechanism in which cells change the strain and stiffness of the ECM due to traction forces and other cells respond to those strains by migrating according to durotaxis. Afterwards, new cell positions lead to new traction forces and strains, which translates to new preferred directions of movement and so on.

1.2 Biological Background

Having described the mechanism that is going to be explored, it is now necessary to give a more thorough explanation on the organelles and molecules that take part in this process.

First, there is the cell membrane, also called cytoplasmatic or plasma membrane, that separates the gel-like interior of the cell (cytoplasm), constituted by the cytosol (liquid domain) and the cell's organelles, from the fluid-like exterior. Its functions include protection from the environment, selective permeability of material, structural support through adherence, cell signaling and, by attaching to the cytoskeleton, it provides shape and mechanical resistance to the cell. The cell membrane is organized in two layers (Fig. 1.1) and it is mainly composed of a class of molecules called phospholipids (Fig. 1.2).

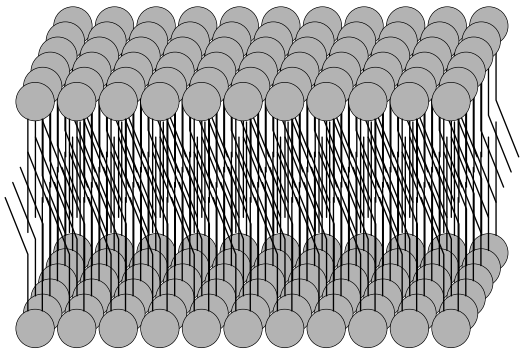

FIGURE 1.1: The self-assembled configuration of the plasma membrane according to the fluid mosaic model [8]. Due to the water affinity properties of the phospholipid, the membrane has two layers in which the polar portion of the molecules is facing outwards.

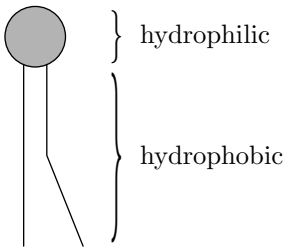

FIGURE 1.2: The structure of a phospholipid. The head (circle) contains a negatively charged phosphate group and the tails (lines) are basically long carbon-carbon chains. Therefore, regarding water affinity, this molecule has a hydrophilic head (high water affinity) and hydrophobic tails (low water affinity).

However, much of the membrane's functionality is largely defined by complementary proteins within and adjacent to it (Fig. 1.3). Proteins are large and complex molecules, made from a sequence of monomers, called amino acids, and are critical to the functionality, regulation and structure of the body's tissues [9].

There are two main groups of membrane proteins. Integral membrane proteins, also called transmembrane proteins, are spread across and pierce through the membrane. These proteins

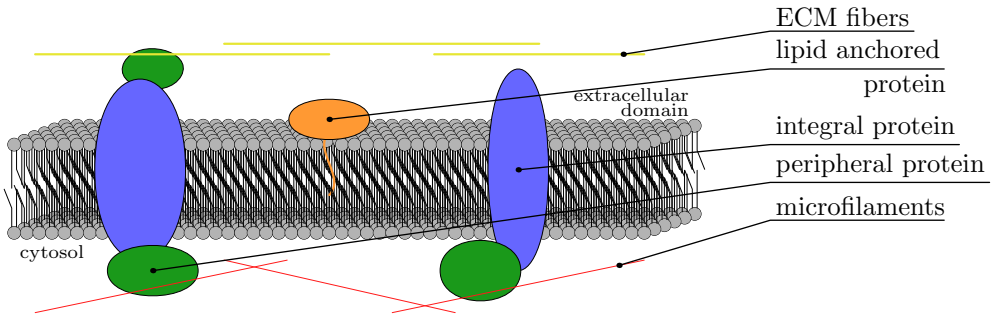

FIGURE 1.3: Diagram showing how proteins are embedded in the cell membrane and how they are classified accordingly. Integral (transmembrane) proteins (in blue) pierce through the membrane. Peripheral proteins (in green) connect directly or indirectly (by attaching to integral proteins). Lipid anchored proteins (in orange), as the name suggests, require a hydrophobic lipid inside the membrane in order to remain attached to the membrane. These proteins provide functionality, which differs according to its type, to the cytoplasmatic membrane.

play a crucial role in adhesion and transport. Peripheral membrane proteins are connected directly to the membrane or indirectly by interacting with transmembrane proteins. They can be present in both sides of the membrane. Additionally, cytoskeletal filaments (mostly actin) connect to the bilayer by means of peripheral (adapter) proteins, providing the cell with greater support and with means to communicate physically with the exterior [10]. Furthermore, proteins in the exoplasmatic domain are often attached to components of the ECM.

Next, there is the cytoskeleton composed of protein filaments that support the nucleus and plasma membranes. Not only does it provide shape and mechanical resistance to the cell, but also allows the cell to apply forces and move. Additionally, it plays a role in cell signaling pathways (the intermediate reactions needed for a cell to respond to stimuli) and is fundamental in cell division.

The filaments that make up the cytoskeleton are classified in three different groups (Fig. 1.4) [11]. Actin filaments, also called microfilaments, are formed near the cell membrane in non-muscle cells and are responsible for connecting the rest of the cytoskeleton to the membrane. Because microfilaments are strong and flexible, they are directly involved in altering the cell's shape. Moreover, by connecting to the membrane proteins, actin filaments play a major role in initiating the reaction chains needed to respond to external stimuli and in both cell-cell and cell-matrix adhesion. Microtubules are hollow tube-like, yet thicker, filaments and are mainly concerned with intracellular transport, cell division and maintaining the structure of the cell. Intermidiate filaments form an internal network, that extends from the nucleus, which provides additional structural support.

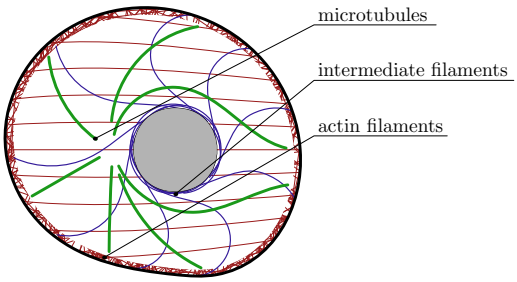

FIGURE 1.4: A schematic representation of how the basic constituents of the cytoskeleton are distributed within the cell. Namely, microtubules (green), intermediate filaments (blue) and actin filaments (red). Actin and microtubules can observed using fluorescence microscopy (Fig. 1.5).

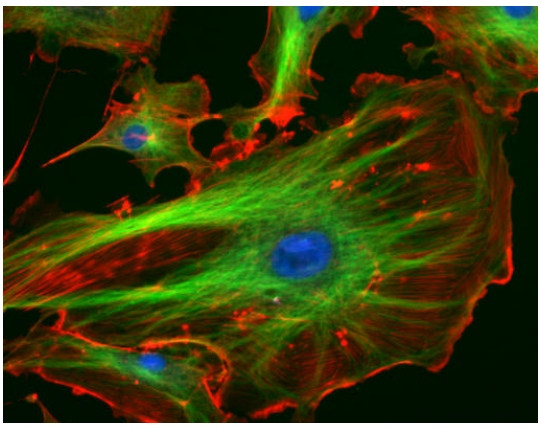

FIGURE 1.5: Image obtained with a fluorescence microscope representing bovine pulmonary artery endothelial cells. The nucleus is marked blue, actin is stained with red and tubulin, of which microtubules are composed, marked green. Example image from the ImageJ-Programmpaket (adapted), available at https://imagej.nih.gov/ij/images/.

Outside the cell there is the extracellular matrix, a collection of molecules in the exoplasmatic domain that serve as a scaffold for the body providing support to the surrounding cells and organizating them into tissues (Fig. 1.6).

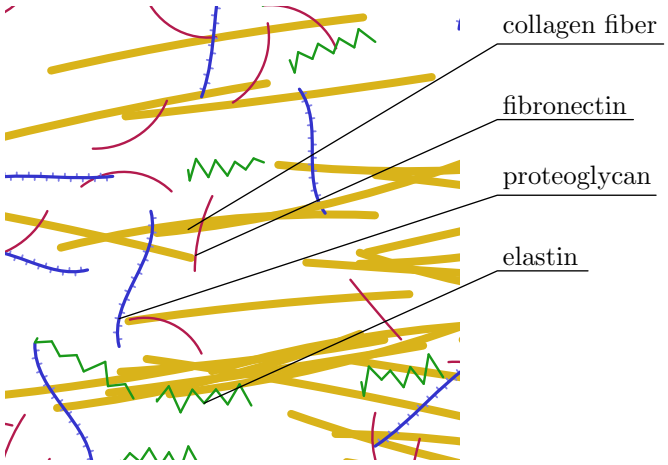

FIGURE 1.6: ECM is composed of fibrous proteins, for example, collagen (in yellow), fibronectin (in red) and elastin (in green), and proteoglycans (in blue). Collagen confers density and stiffness of the matrix. Elastin, as the name implies, is responsible for the elasticity of the ECM. Fibronectin bind to collagen fibers, promoting structural integrity of the ECM, and cell-ECM adhesion sites, hence it is directly implicated in cell adhesion. Proteoglycans are able to bind water and cations.

The molecules that compose the ECM are typically secreted by cells [12]. Collagen fibers provide mechanical strength and resilience to the substrate. Proteoglycans, carbohydrate polymers attached to other ECM molecules, keep the tissue and the surrounding cells hydrated, provide support to cells and can also help trap other molecules, such as growth factors. Soluble multiadhesive matrix proteins, for example fibronectin and laminin, are able to cross-link different components of the ECM and cell-matrix adhesion receptors. Elastin, proteins that confer elasticity to the matrix, that is the ability to return to the original configuration after

being deformed.

Actually, the fibers from the ECM, by attaching to integral membrane proteins, or their adapter proteins, and consequently indirectly to the cytoskeleton, not only adhere to cells by means of focal adhesions (FA), but also are able to coordinate several cell functions, by activating signaling pathways [13]. The resulting responses encompass cell growth, proliferation, gene expression, cell differentiation and migration [14].

1.2.1 Adhesion

Cells, in order to form tissues, adhere to one another and to the substrate they are on and, therefore, adhesion plays a crucial role in morphology. The molecules responsible for adhesion are specialized membrane integral proteins called cell adhesion molecules (CAMs), typically with adapter proteins connected to the actin cytoskeleton [15]. Effectively, there are two types of adhesion according to what the cell is adhering to.

Cell-Cell Adhesion

Although integral proteins typically span the membrane, CAMs often cluster into specialized cell junctions, whose diversity allows for both long lasting and transient adhesion [9]. In addition, CAMs are able to recruit multifunctional adapter proteins to its cytosol-facing surface. These peripheral proteins connect the CAM to microfilaments of the cytoskeleton and gather other molecules that participate in cell signaling pathways, which control protein production and gene expression of the cell. Because of this, the cell's surroundings affect its shape and function.

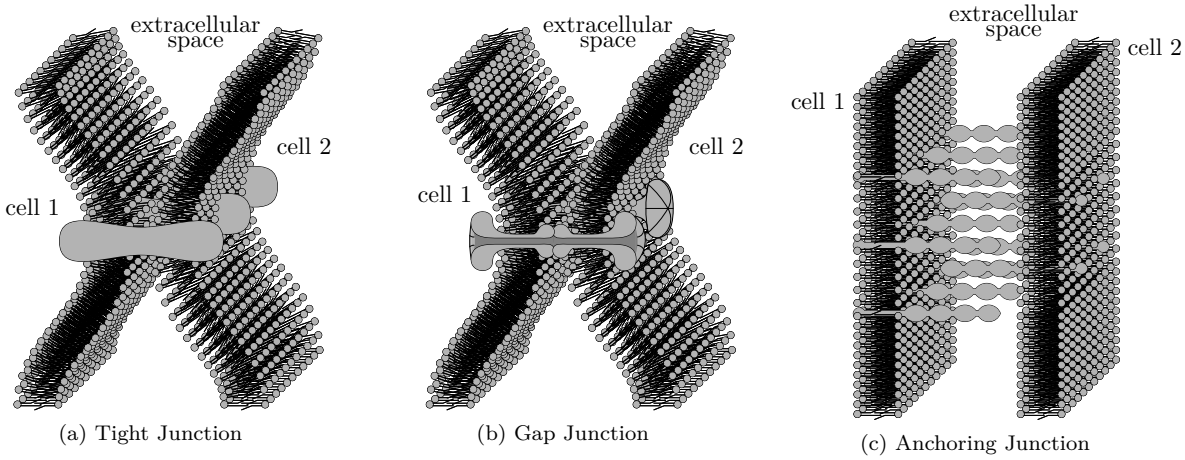

(a) Tight Junction (b) Gap Junction (c) Anchoring Junction

FIGURE 1.7: Diagrams representing three fundamentally different types of cell-cell adhesion junctions.

As mentioned above, CAMs can also bind to other CAMs laterally in the same surface forming clusters. When these clusters attach to other cells they create junctions. There are several types of junctions. Tight junctions (Fig. 1.7a), in which transmembrane proteins are embedded in both cell membranes, form linked rows across the membrane resulting in an impermeable barrier. Gap junctions (Fig. 1.7b) directly connect the cytoplasm of the two

cells through a regulated gate. Anchoring junctions have an extracellular cluster interaction (Fig. 1.7c). Adherens junctions are anchoring junctions in which the CAMs are connected to the actin cytoskeleton and are mainly composed of cadherin molecules. In constrast, desmosomes are made of two specific cadherins and connect to keratin intermediate filaments instead of microfilaments.

Cadherins are key CAMs in cell-cell adhesion (Fig. 1.8), cell signaling and differentiation. The most common cadherins in the cadherin family are the E-, P- and N-cadherins and are referred to as classical cadherins, in fact E-cadherins are greatly expressed during the early stages of development [16].

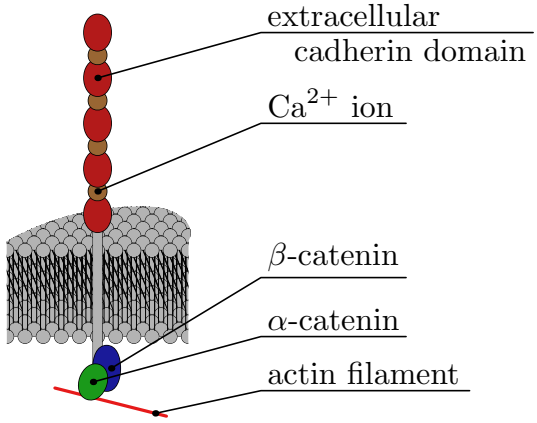

FIGURE 1.8: Diagram of the structure of a cadherin molecule. The extracellular region is above the membrane and the cytosol below it. The extracellular domain contains repeated sequences of proteins with sites for calcium ions Ca^{2+}, hence the name (calcium, Ca, adhesion protein). These ions are essential for cadherins to adhere to other cadherins. On the intracellular end of the cadherin, there are adapter proteins responsible for connecting the cadherin to the cytoskeleton.

The extracellular component of cadherins, made of Ca^{2+} domains (hence the name cadherin) linked together, attach to calcium domain of other cadherins. Inside the membrane, the common proteins that bind the cadherin to the actin cytoskeleton are α- and/or β-catenin and are essential for strong adhesion.

Cell-Matrix Adhesion

Integrins are transmembrane CAMs associated with cell-matrix adhesion, usually surrounded by peripheral macromolecule structures (Fig. 1.9). By clustering, integrins and the corresponding adapter proteins can assemble into focal adhesions (FAs). These integrin-containing proteic structures connect bundles of actin filaments to ligands of the ECM, both physically and functionally [17]. Additionally, integrin molecules can be in an active or inactive configuration. Therefore, by regulating integrin expression or its binding activity (or both), the cell can adjust cell-matrix adhesion strength, ranging from weak and fleeting to strong and long lasting.

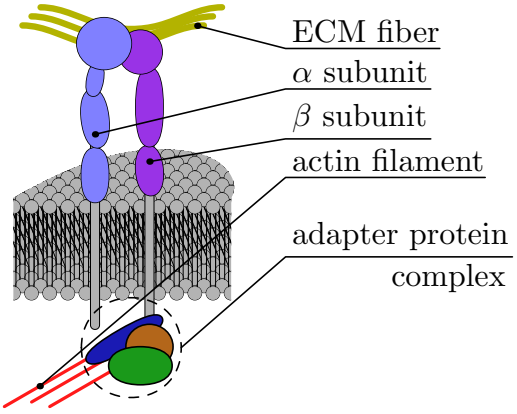

FIGURE 1.9: The structure of an activated integrin. The extracellular α and β subunits grip ECM fibers, namely fibronectin. The intracellular portion of the integrin is connected to several adapter proteins (examples include talin, FAK, vinculin, etc.), which mediate its activation and signal transmittance, which in turn are bound to the cytoskeleton.

Hence, FAs (and, consequently, integrin molecules) are essencial for adhesion to the ECM and for adhesion dependent signaling (mechanosensing), which both cell growth and motility depend on, present in processes such as migration in the embryo (morphogenesis) and inflammatory response [18].

1.2.2 Cell Migration

In order for self-organization to occur, cells must be able to move according to environmental cues. In fact, the cytoskeleton is crucial for this process. Namely, the actin cytoskeleton, by organizing in a wide variety of structures, such as bundles and networks, and possessing filaments of dramatically different lengths, enables the cell to assume, and easily change, shape. Effectively, by regulating actin polymerization and degradation the cell can exert forces, through adhesion, necessary for cell motility.

Polarization of the cell is inevitably necessary for directed movement [19]. Without it, the cell would not be able to discern a direction to move towards. External cues and/or stochastic fluctuations lead to an asymmetry and polarity. Environmental stimuli include the gradient of a chemical concentration (chemotaxis), a stiffness gradient and stretch direction (durotaxis) and the gradient of attractant chemicals bound to the ECM (haptotaxis), for example. On the other hand, fluctuations may lead to the spontaneous emergence of polarity due to positive feedback.

Cell locomotion on a two dimensional surface typically exhibits a sequence of changes in morphology (Fig. 1.10). First, there is an extension of the cell membrane protrusion (leading edge) pushed forward by actin networks due to actin polymerization. Afterwards, at the leading edge actin bundles form focal adhesions and attach the cell to the ECM. Next, the bulk of the cell is propelled forward. Finally, the cell rear adhesions are released, effectively moving the cell forward. Therefore, in order to move, the cell needs to strike a balance between cytoskeleton contraction and traction forces.

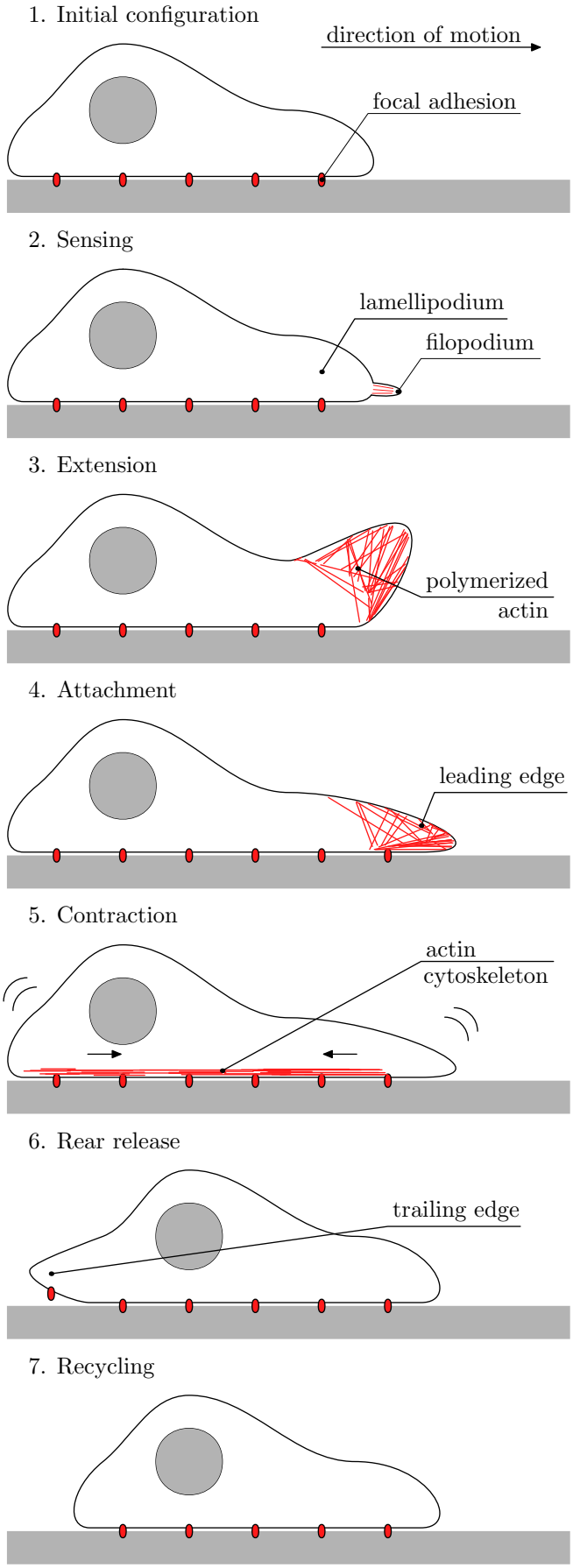

FIGURE 1.10: Diagram representing how a cell is able to move on a substrate. The cell is placed above the ECM and adheres to it by means of FAs. After initially sensing its surroundings and breaking symmetry, the cell rearranges itself forming what is called a lamellipodium, a protrusion on the direction of movement containing actin in a mesh-like configuration. The cell scans its surroundings by creating thin and long protrusions called filopodia. After deciding the direction of the next step, the lamellipodium is extended forward by polymerizing actin. Then, the leading edge attaches to the ECM, by creating a new FA. The actin cytoskeleton contracts (some actin bundles, due to positioning, have a crucial role in this body movement and are also called stress fibers), propelling the cell body forward and the FAs at the trailing edge are released. After going through this process the cell is displaced from its initial configuration and it is able to recycle the, now unused, FA. By repeating this process the cell can keep on moving according to what its surroundings dictate. Figure adapted from [20].

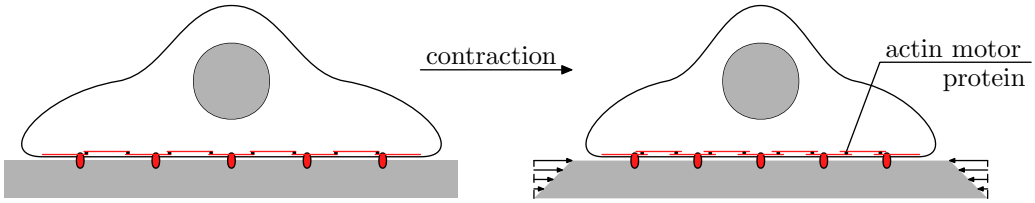

FIGURE 1.11: Diagram explaining how a contraction of actin bundles,by means of actin motor proteins, for example, the myosin family, connected to the cell membrane leads to a force applied to the ECM, when the cell is adhered to it. This force, in turn, causes a deformation in the substrate.

Traction Forces

Typically, cells attach to the ECM in order to survive. Once attached they exert tensile forces on the substrate, called traction forces (Fig. 1.11). These forces are not only needed for cell migration, but also for ECM organization and mechanical signal generation [21].

Actin filament bundles are joined together by specific proteins, which, by consuming energy, are capable of moving along the microfilaments and, because of that fact, are called motor proteins. These proteins are responsible for contracting and extending the actin cytoskeleton. Through FAs, contractile forces are transmitted to the ECM as tensile stress and, as a result, the surrounding matrix is deformed due simply to adhesion. Therefore there is a correlation of cell force traction with focal adhesion size, number and distance from the cell's center.

Mechanosensing and Durotaxis

In stark contrast with traction forces, the process by which a cell senses the mechanical properties of its surroundings, mechanosensing, is still poorly understood. However, both are mediated through focal adhesions and the actin cytoskeleton. This sensing mechanism plays a remarkably important role in cell polarization and migration. Effectively, cells in rigid substrates can become polarized, whereas, in soft substrates, cells tend to become uniformly oriented. Also, direction of strain and stretch help breaking symmetry.

ECM stiffness also influences cytoskeleton mechanical properties and interaction with focal adhesion complexes. Additionally, stiffness alters fibronectin assembly rate inside the cell, therefore, after its secretion, regulating ECM composition.

Cells also exhibit a preferred direction of motion towards higher stiffness, called durotaxis [22]. This process requires the cell to be able to actively sense its surroundings, interpret the mechanical stimuli and react accordingly.

1.3 Motivation

Some of the underlying processes, more specifically sensing of mechanical cues and physical responses responsible for the emergence of patterns, are still not entirely understood and even more so when integrating biochemical signaling pathways. Namely, durotaxis, mechanosensing and traction force generation are phenomena relevant in a wide variety of cell systems, due to

them being intimately related to cell migration. Aside from developmental biology processes, such as vasculogenesis, embryogenesis and morphogenesis, mechanical cues and cell migration are also relevant in other systems, such as, for example, angiogenesis, metastasis development, which is one of the hallmarks of cancer [23], and inflammatory response. Therefore, patterns resulting from cell self-organization shed light onto these mechanisms.

Effectively, defective cell migration leads to errors during morphogenesis, vasculogenesis and other processes dependent on it. By understanding the mechanisms underlying cell migration it is possible to apply that knowledge to the treatment of complications that may arise from the aforementioned phenomena.

In order to understand the role of the cell's mechanical processes, because of the sheer complexity of their biochemical basis, computer models are needed to test theoretical hypothesis [24]. By proposing mechanisms and modeling them afterwards, the simulation results of the model can be compared to experimental results and help disprove the assumptions made. Additionally, simulations can suggest new experiments that may help provide evidence for a particular mechanism. Hence, computer modeling is a theoretical tool that allows to study coupled processes and the feedback loops that might arise from their interaction.

Therefore, simulating models which include the mechanical basis of cell migration, the classical example being pattern formation, provides insight on how the cell interacts physically with its neighborhood and, understanding that interaction, enlightens the biochemical processes needed for coupled mechanisms to occur.

1.4 State of the Art

During the last few decades, many computational models were used in order to simulate cell dynamics. Many different approaches have been taken, from continuum partial differential equations to discrete agent-based models. For instance, single cell migration has been recently described by a mechanical model of a viscoelastic material with active strains on the ECM being applied by the cytoskeleton in soft and stiff substrates [25]. Another approach, using a cellular Potts model (CPM), was proposed for durotaxis induced single cell migration [26]. For multicellular systems, however, including too many details about how a single cell functions proves too computationally intensive, and therefore there is a need for simpler models for cell mechanisms. Discrete models, such as cellular automata models [27], CPM and agent-based multiscale models [28] have been extensively used for describing systems such as sprouting angiogenesis, tumor growth and metastasis, and other systems where cell movement is relevant. Continuum models have also been used for cells, including partial differential equations of cell density [29] and phase-field models [30]. Furthermore, many different mechanical models for the behavior of ECM can be applied, from isotropic linear elastic material models to much more complex biphasic hyperelastic models [31]. Additional details of the ECM can be described, for example taking into account fibril orientation when describing its response to

mechanical stimuli [32].

Pattern formation has been studied with help from such models. For example, a contact inhibited chemotaxis vasculogenesis and angiogenesis model [33], and a multi-scale vasculogenesis CPM including chemotaxis and cytoskeleton remodeling [34]. However, because there are cell systems where patterns form without exhibiting chemotaxis [35], these descriptions may not suffice and other models including, for example, mechanical cues, need to be used. Recently, a two-dimensional model [36] for vasculogenesis was developed and it integrates a finite element model (FEM) for an isotropic elastic material with a CPM, coupling them through a traction force generation model from [37] and a durotaxis model, in order to study mechanically relevant multicellular systems. Its simple approach to cell processes and to mechanical responses allows the simulation of systems with hundreds of cells with relative ease and, for that reason, it is going to be used here in order to study mechanically-driven pattern formation.

Furthermore, efforts have been made in finding empirical evidence to support theoretical models of the signaling mechanisms. In fact, cell migration is still being thoroughly investigated in various contexts through different guidance principles. Studies include the collective tumor cell spreading rigidity dependence [38] and the filopodia mechanical probing mechanism [39], to name a few. Moreover, ECM dependence and processes underlying cell-matrix interactions are also being investigated. Recently, efforts have been made in studying the effect of ECM topology on cell migration using microfabricated substrata [40] and tumor invasion dependence on ECM composition [41], for example. Traction force microscopy is currently being used in order to quantify forces and displacements on the ECM [42], in order to understand the nonlinearity of the ECM's response to mechanical forces. In general, because cell migration as a whole is vastly complex process and underlies cancer metastasis formation, a global research effort is being done in order to progress the understanding of every aspect of this mechanism.

Chapter 2

The Model

The feedback mechanism consists in cells applying traction forces, leading to the deformation the matrix, producing environmental cues, which cells move accordingly to and so on. Therefore the model must capture several distinct behaviors. First, it must account for how the forces acting on the matrix generate displacements, secondly, it must describe how cells migrate not only under the mechanical properties addressed earlier, but also by adhering to one another and to the matrix. In order to complete the cycle, there needs to be a model that, taking into consideration the configuration of the cells, provides insight into the forces being applied to the matrix.

In this chapter, it is going to be described the model proposed by Oers and Rens [36], which encompasses and all of the mentioned components. Starting with an introduction to deformation mechanics, followed by the theoretical framework in which it will be solved. Afterwards, it is going to be presented the model used for cell interactions, mobility and the relation between matrix strain and cell movement. Finally, the model for predicting forces applied to the ECM will be described.

2.1 Mechanics of the ECM

Each element of the ECM will have a displacement due to the force cells exert on the substrate. Therefore, a relationship between these two quantities (displacement and traction forces) is required.

In this work, the deformation of the ECM will be described using continuum mechanics. More specifically, under the assumption of small displacements. For that effect, it will be used the infinitesimal strain theory approach.

Afterwards, the theoretical framework of finite element method (FEM) will be described. It allows for the derivation of a smaller local problem from a possibly large and difficult one, regarding only one element, and to assemble all bits and pieces, in order to recreate a simpler global problem. It is followed by its application to structural mechanics.

2.1.1 Infinitesimal Strain Theory

The aim of this analysis is to relate forces to displacements. A displacement, in this framework, is simply the difference in position between the undeformed and the deformed configurations. First it is going to describe the displacements using the concept of strain, which is a component-wise relative difference in displacement. In the second part, it is going

to be looked into what generates strain, namely stress, tightly related to forces, and how it is written in terms of strain, depending on the material.

Displacements can be decomposed in a rigid-body motion (parallel transport and rotation) and in a deformation. Although one can derive the description of small deformations from a more general framework (finite strain theory), a geometrical and transparent approach is as follows. Suppose there is a vector field $\mathbf{u}(\mathbf{x})$ defined inside a body, which describes the difference in position of an infinitesimal element after some amount of time, that is, $\mathbf{x} \to \mathbf{x}' = \mathbf{x} + \mathbf{u}(\mathbf{x})$ (Fig. 2.1).

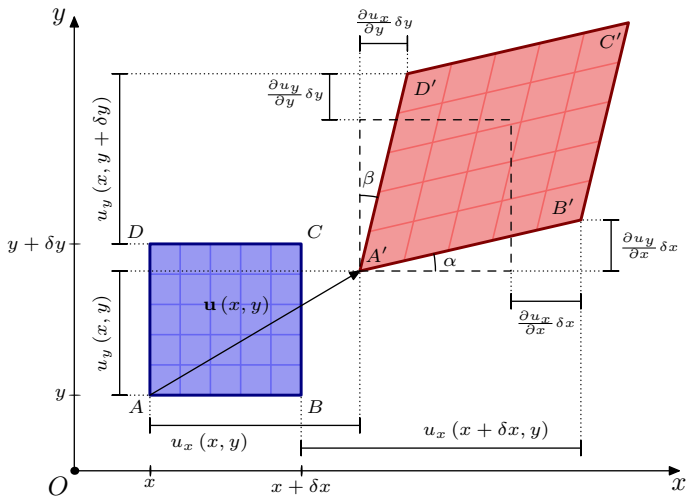

FIGURE 2.1: Diagram of both deformed and undeformed configurations. Under the assumption of infinitesimal displacements, the remaining corners of the initial element can be mapped by expanding the field in a Taylor series until the first order term.

In tensor notation and in the first order assumption, displacements at position $\mathbf{x} + \delta\mathbf{x}$ can be written as

$$u_i(\mathbf{x} + \delta\mathbf{x}) \approx u_i(\mathbf{x}) + \partial_j u_i(\mathbf{x})\,\delta x_j, \tag{2.1}$$

where, the first term represents parallel transport, the second term contains both rotation and deformation.

Effectively, the displacement gradient can be decomposed in a symmetric and an antisymmetric tensors:

$$\partial_j u_i = \frac{1}{2}(\partial_j u_i + \partial_i u_j) + \frac{1}{2}(\partial_j u_i - \partial_i u_j) = \varepsilon_{ij} + \omega_{ij}, \tag{2.2}$$

where u_i simply refers to $u_i(\mathbf{x})$, and $\partial_j u_i$ represents $\frac{\partial u_i}{\partial x_j}$.

Setting aside parallel transport and rotation, the attention will be focused only in the strain tensor,

$$\varepsilon_{ij} = \frac{1}{2}(\partial_j u_i + \partial_i u_j). \tag{2.3}$$

Notes on why ω_{ij} represents pure rotation and in what sense ε_{ij} translates to deformation can be found in appendix A.

Moreover, symmetry of the deformation tensor means that it has 6 independent components (in 3D). Note that the inverse relation of (A.4) is a system of 6 differential equations in order to determine the 3 components of the displacement vector. This over-determined system implies that, in order for the equations to be integrable, the choice of a strain tensor is not arbitrary. Indeed, ε_{ij} needs to satisfy the compatibility equations,

$$\partial_k \partial_l \varepsilon_{ij} + \partial_i \partial_j \varepsilon_{kl} - \partial_j \partial_l \varepsilon_{ik} - \partial_i \partial_k \varepsilon_{jl} = 0, \tag{2.4}$$

which ensures that u_i is single-valued and continuous.

However, there is still the need to relate strain to its source, that is, the applied forces. This relation will include the properties of the object being deformed, because different materials respond differently to the same conditions.

However, it is not useful to think in terms of force. Applying a force to an object needs to take into account the distribution of force over some surface. Therefore, the concept of stress needs to be introduced. Stress is defined as the force per unit area applied on a surface (Fig. 2.2).

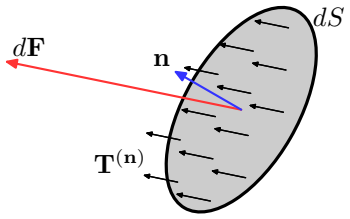

FIGURE 2.2: Illustrated concept of stress.

In order to define the state of stress, under the small deformations approximation, the Cauchy stress tensor is introduced. Consider a surface perpendicular to the vector $\mathbf{n} = n_i$ being applied a stress of $T_j^{(\mathbf{n})}$. The Cauchy stress tensor is defined such that:

$$T_j^{(\mathbf{n})} = \sigma_{ij} n_i, \tag{2.5}$$

and, according to the definition, the force applied on the surface (dS) would be:

$$dF_i = T_i^{(\mathbf{n})}\, dS = \sigma_{ji} n_j\, dS. \tag{2.6}$$

From the concept of stress, assuming the body being deformed is at rest, it is possible to obtain the balance equations, the symmetry of the stress tensor and the energy conservation equation (appendix B). Namely, the energy conservation, for a body occupying volume V and with surface S, reads

$$\oint_S u_i T_i^{(\mathbf{n})}\, dS + \int_V u_i b_i\, dV = \int_V \varepsilon_{ij}\sigma_{ij}\, dV, \tag{2.7}$$

where $T_i^{(\mathbf{n})}$ is the stress applied on the surface S and b_i is the sum of all body forces acting on the object.

The principle of virtual displacements states that the virtual external work of real external forces, T_i and b_i, moving through virtual displacements δu_i is equal to the internal virtual work of real internal stresses σ_{ij} over the virtual strains $\delta\varepsilon_{ij}$, as long as σ_{ij} is in equilibrium with T_i and b_i and $\delta\varepsilon_{ij}$ is compatible with δu_i. In short,

$$\delta W_E = \delta W_I, \tag{2.8}$$

implies that

$$\oint_S \delta u_i T_i^{(\mathbf{n})}\, dS + \int_V \delta u_i b_i\, dV = \int_V \delta\varepsilon_{ij}\sigma_{ij}\, dV. \tag{2.9}$$

An in depth analysis of variational methods for structural mechanics can be found in [43].

Moreover, stress and strain are intimately related by a constitutive equation. For a linear elastic material, that equation is the generalized Hooke's law,

$$\sigma_{ij} = C_{ijkl}\varepsilon_{kl}, \tag{2.10}$$

where C_{ijkl} is called the stiffness tensor. For a linear isotropic elastic material, by exploiting its symmetries, this tensor takes a particular form (appendix C),

$$\sigma_{ij} = \frac{E}{(1+\nu)(1-2\nu)}\left(\nu\delta_{ij}\varepsilon_{kk} + (1-2\nu)\,\varepsilon_{ij}\right), \tag{2.11}$$

where E and ν are mechanical properties, namely, the Young's modulus and the Poisson ratio. Under the assumption that the forces a cell applies to the ECM are parallel to its surface (for example, if perpendicular to $n_i = \delta_{3i}$, $\sigma_{13} = \sigma_{23} = \sigma_{33} = 0$), the expression for the stiffness tensor can be further simplified (appendix C) to, in vector notation for strain and stress,

$$\begin{pmatrix}\sigma_{11}\\ \sigma_{22}\\ \sigma_{12}\end{pmatrix} = \frac{E}{1-\nu^2}\begin{pmatrix}1 & \nu & 0\\ \nu & 1 & 0\\ 0 & 0 & \frac{1}{2}(1-\nu)\end{pmatrix}\begin{pmatrix}\varepsilon_{11}\\ \varepsilon_{22}\\ 2\varepsilon_{12}\end{pmatrix}. \tag{2.12}$$

This assumption is often called the plane stress assumption.

2.1.2 Finite Element Method (FEM)

Overview

This method is a numerical technique that involves subdividing a domain into simpler parts, called finite elements. In this way, it reduces a difficult problem into a large number of simpler ones solved locally, eliminating all spatial derivatives in the process. For a steady state solution, this method results in a set of algebraic equations, that relate adjacent elements, solvable by error minimization. Detailed information about the method and its application to structural mechanics can be found in [44].

Because the subdivision of the integration domain, also called mesh generation, does not necessarily impose the same geometry on every element, it allows for a finer and more precise discretization (that is, mesh refinement adaptation) on regions where the solution might vary considerably, on domain changes and other boundary regions and wherever else precision might be important.

After discretization, the domain becomes composed of nodes, whose connectivity define the aforementioned elements (Fig. 2.3). A quantity $q(\mathbf{x})$ originally defined inside the domain, is now written in terms of $q^{(n)} = q\left(\mathbf{x}^{(n)}\right)$, where $\mathbf{x}^{(n)}$ refers to the position of node n. Inside each element, that quantity needs to be interpolated, in order to approximately obtain $q(\mathbf{x})$. The finer the grid, the more precise this interpolation becomes.

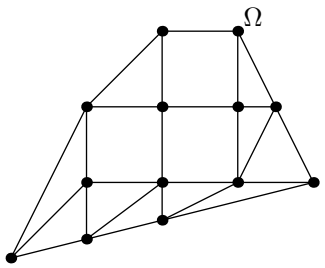

FIGURE 2.3: A domain Ω after mesh generation. It is composed of smaller elements defined by node connections.

The next step is to decouple an element from the global frame of reference and consider a simpler frame on which to map the element onto. Consider an element defined by N nodes on a local frame of reference with local coordinates (ξ, η, ζ). The element's nodes, previously with positions $(x^{(n)}, y^{(n)}, z^{(n)})$, in the local frame of reference are in positions $(\xi^{(n)}, \eta^{(n)}, \zeta^{(n)})$.

It is possible to obtain the interpolation of a quantity, q, by expanding it in a power series inside the element, that is,

$$q(\xi, \eta, \zeta) = c_1 + c_2\xi + c_3\eta + c_4\zeta + c_5\xi^2 + c_6\eta^2 + c_7\zeta^2 + c_8\xi\eta + c_9\xi\zeta + c_{10}\eta\zeta + \ldots, \tag{2.13}$$

where c_1, c_2, c_3, ... are constants yet to be defined. However, having only N nodes, that is, N degrees of freedom, implies that the best approximation that can be achieved this way is by computing the first N terms. This way, it is possible to, by assigning local coordinates to the element's nodes, use the N equations $q\left(\xi^{(a)}, \eta^{(a)}, \zeta^{(a)}\right) = q^{(a)}$, one for each node a, to find out the constants c_1, c_2, ..., c_N (done in appendix D for elements with three and four nodes).

$$q(\xi, \eta, \zeta) = \sum_{i=1}^{N} \phi^{(i)}(\xi, \eta, \zeta)\, q^{(i)}, \tag{2.14}$$

where $\phi^{(i)}$ are functions of the coordinates, called shape functions, yet to be defined and depend solely on geometrical factors, as the name implies. Note that the shape function of every node a, $\phi^{(a)}$, evaluated at every other node b must always yield zero, in order for $q\left(\xi^{(a)}, \eta^{(a)}, \zeta^{(a)}\right) = q^{(a)}$ to hold.

Then, after computing the shape functions for equation (2.14), all the spatial derivatives of q will be applied on those functions instead. That also means that, for each element, the transformation from global to local coordinates must be known.

Making use of index notation, let

$$q_i = \left(q^{(1)}, \ldots, q^{(N_e)}\right), \tag{2.15}$$

$$\phi_i = \phi_i(\xi, \eta, \zeta) = \left(\phi^{(1)}(\xi, \eta, \zeta), \ldots, \phi^{(N_e)}(\xi, \eta, \zeta)\right), \tag{2.16}$$

of a certain element e be vectors of dimension N_e, where N_e is the number of nodes in that element. Using the Einstein summation convention, (2.14) becomes

$$q(\xi, \eta, \zeta) = \phi_i q_i. \tag{2.17}$$

Next, if the problem isn't already in a variational formulation, it needs to be rewritten as such. That is, a problem of the form: find the function $u = u(x_i)$ that, under some boundary conditions, satisfies

$$\hat{A}u = f, \tag{2.18}$$

where $\hat{A}$ is a linear operator (for example, for the Poisson equation $\hat{A} = \nabla^2$) and $f = f(x_i)$ is a known function of the coordinates, that, by multiplying by a test function $v = v(x_i)$ and integrating inside a volume V, becomes the variational (weak) formulation: find $u = u(x_i)$ that, for all v,

$$\int_V v\hat{A}u \, dV = \int_V vf \, dV. \tag{2.19}$$

An example of this procedure for the Poisson equation has been done on appendix E.

After stating the problem in its weak form, using the Ritz-Galerkin method (which belongs to a group of methods called mean weighted residuals), we expand u and v (and even f if need be) using an infinite set of basis functions ψ_i, such that,

$$u = c_i \psi_i, \tag{2.20}$$

$$v = c'_i \psi_i, \tag{2.21}$$

where c_i and c'_i are constants. Equation (2.19) can be rewritten as

$$c'_i \int_V \psi_i \hat{A} \psi_j \, dV \; c_j = c'_i \int_V \psi_i f \, dV, \tag{2.22}$$

for all v, that, is c'_i, where c_i is the unknown. Therefore, the last equation becomes

$$A_{ij} c_j = b_i, \tag{2.23}$$

where,

$$A_{ij} = \int_V \psi_i \hat{A} \psi_j \, dV, \tag{2.24}$$

and,

$$b_i = \int_V \psi_i f \, dV. \tag{2.25}$$

Using a finite number of basis functions, $u \approx c_i \psi_i$, which means (2.23) is an approximation. The symmetric matrix A_{ij} is called the stiffness matrix (not to be conflated with stiffness tensor). Additionally, f can also be expanded on the same basis, $f = f_k \psi_k$, and therefore $b_i = M_{ik} f_k$, where

$$M_{ik} = \int_V \psi_i \psi_k \, dV \; f_k \tag{2.26}$$

is called the mass matrix, and the equation (2.23) becomes

$$A_{ij}c_j = M_{ik}f_k. \tag{2.27}$$

Similarly, the problem for each element e with volume Ω_e, using the shape functions as a basis (such that $u = u_i\phi_i$), has the form

$$\int_{\Omega_e} \phi_i \hat{A}\phi_j \, dV \; u_j = \int_{\Omega_e} \phi_i f \, dV, \tag{2.28}$$

or,

$$A^{(e)}_{ij} u_j = b^{(e)}_i, \tag{2.29}$$

where,

$$A^{(e)}_{ij} = \int_{\Omega_e} \phi_i \hat{A}\phi_j \, dV, \tag{2.30}$$

and,

$$b^{(e)}_i = \int_{\Omega_e} \phi_i f \, dV \left[= \int_{\Omega_e} \phi_i \phi_k \, dV \; f_k \right]. \tag{2.31}$$

However this equation is in regards to only one element e occupying Ω_e with N_e nodes. A global equation of the form,

$$A_{\alpha\beta}U_\beta = B_\alpha, \tag{2.32}$$

where instead of the local indices $i, j = 1, \ldots, N_e$, we have global indices $\alpha, \beta = 0, \ldots, N$ regarding all nodes of the mesh. The vector U_β contains all values of u for each node. One method to obtain this equation is called the direct stiffness method, in where

$$A_{\alpha\beta} = \sum_e A^{(e)}_{ij}, \tag{2.33}$$

is typically sparse and always symmetric and positive definite. Similarly,

$$B_\alpha = \sum_e b^{(e)}_i, \tag{2.34}$$

noting that every node has local indices i, depending on how many elements that node belongs to, and a single global index α. A practical example of an assembly is done in appendix F.

After being assembled, the equation can be solved for U_α using techniques such as conjugate gradient method or, for smaller problems, either LU or Cholesky decompositions.

FEM for Structural Mechanics

The ECM will be modeled as a 2D surface to which cells adhere to, this way, because the forces cells apply to the ECM will be roughly within the ECM plane itself, it is reasonable to apply the plane stress conditions. Additionally, in order to simplify the coupling between the FEM and the cell model (discussed in section 2.2), it is going to be used square elements, of side L, in a grid-like mesh. Each node, n, will have a displacement vector $\mathbf{q}^{(n)}$ and a force vector $\mathbf{f}^{(n)}$.

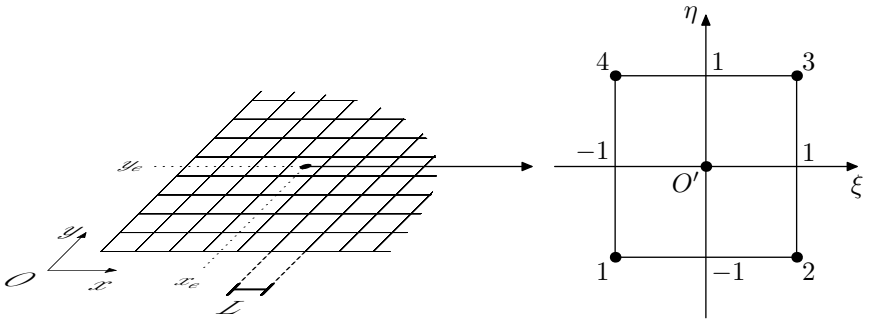

FIGURE 2.4: A grid-like mesh of square elements, of side L, viewed from the global coordinate system (left) and the intended transformation of an element with center (x_e, y_e) to a local frame of eference (right).

For a single element, the equation (2.9) needs to be solved. It is noteworthy to point out that cells apply forces to the ECM through FAs and, consequently, the work done will largely depend on how the distribution of FAs will be modeled. If the FAs are taken to be coincidental with nodes of the FEM mesh, then the work done by a virtual displacement, $\delta\mathbf{u}^{(n)^{\mathbf{T}}}$, is

$$\delta W_E^{(n)} = \delta\mathbf{u}^{(n)^{\mathbf{T}}}\mathbf{f}^{(n)}. \tag{2.35}$$

The internal work, however, is a slightly more contrived. In the local frame of reference of an element e (Fig. 2.4), the displacement field can be interpolated inside the element as

$$\mathbf{u}(\xi,\eta) = \sum_{i=1}^{4} \phi^{(i)}\mathbf{q}^{(i)}, \tag{2.36}$$

where, the shape functions for a square element are,

$$\phi^{(1)} = \phi^{(1)}(\xi,\eta) = \frac{1}{4}(1-\xi)(1-\eta), \tag{2.37}$$

$$\phi^{(2)} = \phi^{(2)}(\xi,\eta) = \frac{1}{4}(1+\xi)(1-\eta), \tag{2.38}$$

$$\phi^{(3)} = \phi^{(3)}(\xi,\eta) = \frac{1}{4}(1+\xi)(1+\eta), \tag{2.39}$$

$$\phi^{(4)} = \phi^{(4)}(\xi,\eta) = \frac{1}{4}(1-\xi)(1+\eta). \tag{2.40}$$

Let $\boldsymbol{\chi}^{(e)}$ represent the local node's displacement components, and $\boldsymbol{\varphi}^{(e)}$ the respective force components,

$$\boldsymbol{\chi}^{(e)} = \begin{pmatrix} q_x^{(1)} \\ q_y^{(1)} \\ q_x^{(2)} \\ q_y^{(2)} \\ q_x^{(3)} \\ q_y^{(3)} \\ q_x^{(4)} \\ q_y^{(4)} \end{pmatrix} \qquad \text{and} \qquad \boldsymbol{\varphi}^{(e)} = \begin{pmatrix} f_x^{(1)} \\ f_y^{(1)} \\ f_x^{(2)} \\ f_y^{(2)} \\ f_x^{(3)} \\ f_y^{(3)} \\ f_x^{(4)} \\ f_y^{(4)} \end{pmatrix},$$

Then, the interpolation can be rewritten as

$$\mathbf{u}(\xi,\eta) = \begin{pmatrix} \phi^{(1)} & 0 & \phi^{(2)} & 0 & \phi^{(3)} & 0 & \phi^{(4)} & 0 \\ 0 & \phi^{(1)} & 0 & \phi^{(2)} & 0 & \phi^{(3)} & 0 & \phi^{(4)} \end{pmatrix} \boldsymbol{\chi}^{(e)} = \mathbb{N}(\xi,\eta)\,\boldsymbol{\chi}^{(e)} \tag{2.41}$$

Furthermore, strain can be written as

$$\boldsymbol{\varepsilon} = \begin{pmatrix} \varepsilon_{11} \\ \varepsilon_{22} \\ 2\varepsilon_{12} \end{pmatrix} = \begin{pmatrix} \partial_x & 0 \\ 0 & \partial_y \\ \partial_y & \partial_x \end{pmatrix} \mathbf{u}(\xi,\eta) = \mathbb{D}\mathbf{u}(\xi,\eta) = \mathbb{D}\mathbb{N}(\xi,\eta)\,\boldsymbol{\chi}^{(e)} = \mathbb{B}(\xi,\eta)\,\boldsymbol{\chi}^{(e)}, \tag{2.42}$$

carefully considering that the differential operators are written in terms of global coordinates and the shape functions in local ones ($\partial_x = \frac{2}{L}\partial_\xi$ and $\partial_y = \frac{2}{L}\partial_\eta$).

Moreover, the constitutive equation for plane stress conditions is

$$\boldsymbol{\sigma} = \begin{pmatrix} \sigma_{11} \\ \sigma_{22} \\ \sigma_{12} \end{pmatrix} = \frac{E^{(e)}}{1-{\nu^{(e)}}^2} \begin{pmatrix} 1 & \nu^{(e)} & 0 \\ \nu^{(e)} & 1 & 0 \\ 0 & 0 & \frac{1}{2}\left(1-\nu^{(e)}\right) \end{pmatrix} \boldsymbol{\varepsilon} = \mathbb{C}^{(e)}\boldsymbol{\varepsilon}, \tag{2.43}$$

where $E^{(e)}$ is the Young's modulus, and $\nu^{(e)}$ the Poisson ratio, of that particular element.

The expression for the internal work of an element e is,

$$\delta W_I^{(e)} = \int_{-1}^{1}\int_{-1}^{1} \frac{L^2}{4}\delta\boldsymbol{\varepsilon}^{\mathbf{T}}\boldsymbol{\sigma}\,d\xi d\eta, \tag{2.44}$$

For this element, the external work is simply the inner product $\delta W_E^{(e)} = \delta{\boldsymbol{\chi}^{(e)}}^{\mathbf{T}}\boldsymbol{\varphi}^{(e)}$. Finally, by substituting the expressions (2.42) and (2.43) in (2.44) and equating internal virtual work to external virtual work, the equation system to be solved is,

$$\mathbb{K}^{(e)}\boldsymbol{\chi}^{(e)} = \boldsymbol{\varphi}^{(e)}, \tag{2.45}$$

where

$$\mathbb{K}^{(e)} = \int_{-1}^{1}\int_{-1}^{1} \frac{L^2}{4}\mathbb{B}^{\mathbf{T}}(\xi,\eta)\,\mathbb{C}^{(e)}\mathbb{B}(\xi,\eta)\,d\xi d\eta, \tag{2.46}$$

is the local stiffness matrix.
The local stiffness matrix is going to be estimated using a gaussian quadrature,

$$\int_{-1}^{1} f(x)\,dx \approx \sum_{i=1}^{n} w_i f(x_i), \tag{2.47}$$

where n is the number of times the integrand will be evaluated, w_i is the weight of the corresponding $f(x_i)$ value. The values w_i and x_i depend on the number n and are given in the table 2.1.

TABLE 2.1: The coordinates x_i and corresponding weights w_i used for the gaussain quadrature as in (2.47), for up to $n = 4$.

n	x_i	w_i
2	$\pm\frac{\sqrt{3}}{3}$	1
3	0	$\frac{8}{9}$
	$\pm\frac{\sqrt{15}}{5}$	$\frac{5}{9}$
4	$\pm\frac{1}{35}\sqrt{525-70\sqrt{30}}$	$\frac{18+\sqrt{30}}{36}$
	$\pm\frac{1}{35}\sqrt{525+70\sqrt{30}}$	$\frac{18-\sqrt{30}}{36}$

Using the estimate with $n = 2$ for both integrals, the matrix becomes

$$\mathbb{K}^{(e)} = \sum_{i=1}^{4} \frac{L^2}{4} \mathbb{B}^{\mathbf{T}}(\xi_i, \eta_i)\, \mathbb{C}^{(e)} \mathbb{B}(\xi_i, \eta_i), \tag{2.48}$$

where ξ_i and η_i are the vectors,

$$\xi_i = \left(-\frac{\sqrt{3}}{3}, \frac{\sqrt{3}}{3}, \frac{\sqrt{3}}{3}, -\frac{\sqrt{3}}{3}\right), \tag{2.49}$$

$$\eta_i = \left(-\frac{\sqrt{3}}{3}, -\frac{\sqrt{3}}{3}, \frac{\sqrt{3}}{3}, \frac{\sqrt{3}}{3}\right). \tag{2.50}$$

If all elements have the same Poisson ratio, then its possible to calculate this matrix only once for some fixed value of the Young's modulus E_0 and then simply multiplying by a factor of $E^{(e)}/E_0$ for the element e.

The next step, is to assemble the global stiffness matrix, using the direct stiffness method

$$\mathbb{K} = \sum_{e} \mathbb{K}^{(e)}, \tag{2.51}$$

which is done in appendix F for a small mesh, and the full equation system becomes,

$$\mathbb{K}\mathbf{q} = \mathbf{f}, \tag{2.52}$$

where $\mathbf{q}$ and $\mathbf{f}$ are the vectors containing every displacement and force components of every node (alternating between x and y components).

Regrading the boundary, it'll be used the Dirichlet boundary conditions with the peripheral nodes having zero displacement, which translates to, in practice, removing rows and columns of all fixed displacements.

For a 2D problem, the maximum number of nonzero elements of the global matrix, per row, is 18, which are the relations between a component and itself, the other component of the same node and both components of the eight nearest neighboring nodes (Fig. 2.5).

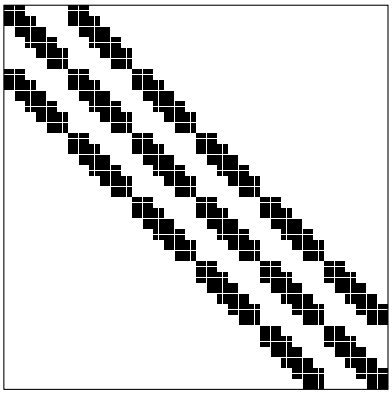

FIGURE 2.5: Distribution of nonzero values of the assembled stiffness matrix, for a 5×5 mesh of square elements. It is a 72×72 matrix. Boundary conditions have yet to be imposed. Even for just 25 elements, this matrix is sparse.

In order to solve the system of equations resulting from equation (2.52), after imposing boundary conditions, it is going to be used a method called Preconditioned Conjugate Gradient (PCG). Due to the algorithmic nature of the method, it is going to be described briefly, when discussing the implementation of the model. However, a more detailed approach can be found in appendix G.

2.2 Cellular Potts Model

In order to simulate cell motility it is used a Cellular Potts Model (CPM) on a square lattice, which coincides with the FEM's elements. This model might be considered a rather complex stochastic cellular automaton (actually bordering on an agent based model).

Overview

The CPM consists of each element i of a lattice having a value $\sigma(i)$ called a tag, or label, mapping the element to a cell, that is, element i belongs to cell $\sigma(i)$. Furthermore, cells $\sigma(i)$ might have different types $\tau(\sigma(i))$ (Fig. 2.6). It is possible, for instance, to assign an adhesion energy to a configuration by looking at each element and its neighborhood.

Effectively, for a system with N cells of M different types, let

$$\mathcal{H}_{\text{adhesion}} = \sum_{\langle ij \rangle} J_{\tau(\sigma(i))\tau(\sigma(j))} \left(1 - \delta_{\sigma(i)\sigma(j)}\right) \tag{2.53}$$

be the energy due to adhesion of the current configuration of the lattice, where $J_{\tau\tau'}$ is the adhesion energy cost between cells of type τ and τ', which is symmetric, and a sum over $\langle ij \rangle$ means a sum over every element i and over every neighbor, j, of i. The factor $(1 - \delta_{\sigma\sigma'})$ means that the energy cost regards only the interfaces of differing cells. Assuming that the entire system is not completely filled with cells, there is the need for a special tag and type, namely, $\sigma = 0$ and $\tau(0) = 0$, in order to represent the absence of cells, that is, the background corresponding to the substrate (adding the type $\tau = 0$ means $J_{\tau\tau'}$ is a $(M+1)\times(M+1)$ matrix).

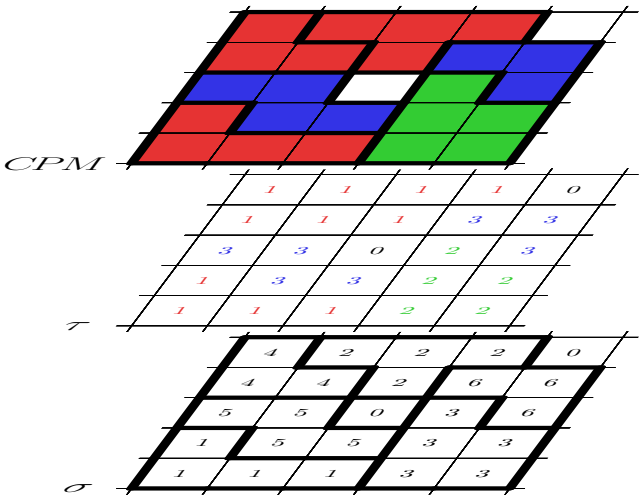

FIGURE 2.6: Schema relating the tag function $\sigma(i)$ on a lattice to the corresponding cell type $\tau(\sigma(i))$ and what that configuration, of σ and τ, is meant to represent in the CPM. In this case, a cell is the set of elements within the bold lines and corresponds to elements with the same value σ and the color of the cell represents its type τ.

However, in order for a tag σ to represent a cell, the region corresponding to the inverse mapping from cell σ to its elements should be simply connected. Not taking connectivity into account, can lead to configurations without biological relevance. Moreover, regarding cell shape, the volume of a cell on a lattice is simply

$$V(\sigma(i)) = \sum_j \delta_{\sigma(i)\sigma(j)}. \tag{2.54}$$

Cells typically have a preferred volume, called the cell target volume, which might depend on cell type, V_τ^T. Therefore, it must correspond to an energy minimum. A simple form for the energy, in this case, is a parabola with minimum at $V = V_\tau^T$. This way, the term in the Hamiltonian for the whole system corresponding to this effect might be written as,

$$\mathcal{H}_{\text{volume}} = \sum_{\sigma=1}^{N} \lambda_{\tau(\sigma)} \left(\frac{V(\sigma) - V_{\tau(\sigma)}^T}{V_{\tau(\sigma)}^T} \right)^2, \tag{2.55}$$

where λ_τ is a parameter which describes the level of energy cost of deviations from the target volume for a cell of type τ.

Other terms of the Hamiltonian might include surface restrictions, chemotaxis terms or, in this case, mechanical response terms regarding durotaxis, which depend on how movement will be modeled.

However, before addressing movement, the neighborhood of i, $\langle ij \rangle$, must be defined. In fact, there are multiple definitions that can be used, such as the Von Neumann and the Moore neighborhoods (Fig. 2.7). For this model, specifically, it is going to be used the Moore's neighborhood.

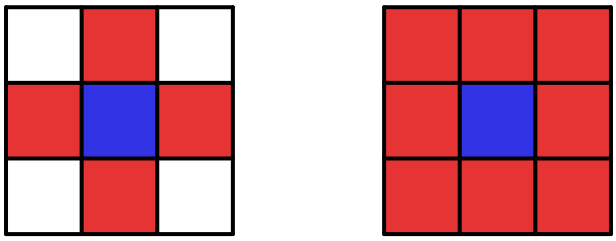

Von Neumann Moore

FIGURE 2.7: Two different ways of defining the neighborhood of an element. The blue element represents the pixel in question and the red regions represent its neighbors.

In order to, at least, attempt to describe movement, there needs to be a sequence of configurations, each of which closely depending on the one before it that resembles the expansions and retractions cells exhibit during migration.

The process often used is to copy the value $\sigma(j)$, from element j, called the source, into the element i, the target ($\sigma(i) \leftarrow \sigma(j)$), reaching a new configuration with a different energy (Fig. 2.8).

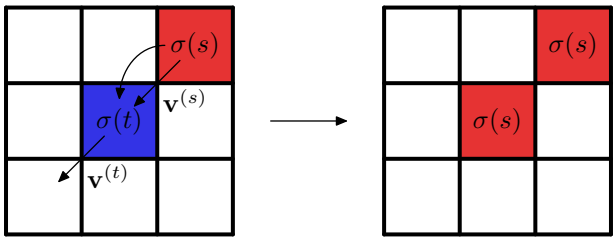

FIGURE 2.8: A CPM step. It consists of a source element s with tag $\sigma(s)$, being copied into a target element t. Therefore, if $\sigma(s) \neq 0$, the source's cell expands towards the target cell according to the vector $\mathbf{v}^{(s)}$ and, if $\sigma(t) \neq 0$, the target's cell retracts in the direction of $\mathbf{v}^{(t)}$.

Let t designate the target element, and s the source. It is possible to simplify the variation of energy due to adhesion,

$$\Delta\mathcal{H}_{\text{adhesion}} = \sum_{\langle ti \rangle} \left[J_{\tau(\sigma(s))\tau(\sigma(i))} \left(1 - \delta_{\sigma(s)\sigma(i)}\right) - J_{\tau(\sigma(t))\tau(\sigma(i))} \left(1 - \delta_{\sigma(t)\sigma(i)}\right) \right], \tag{2.56}$$

and regarding volume,

$$\begin{aligned} \Delta\mathcal{H}_{\text{volume}} = (1 - \delta_{0\sigma(t)}) \frac{\lambda_{\tau(\sigma(t))}}{V^{T^2}_{\tau(\sigma(t))}} \left[\left(V(\sigma(t)) - 1 - V^T_{\tau(\sigma(t))} \right)^2 - \left(V(\sigma(t)) - V^T_{\tau(\sigma(t))} \right)^2 \right] \\ + (1 - \delta_{0\sigma(s)}) \frac{\lambda_{\tau(\sigma(s))}}{V^{T^2}_{\tau(\sigma(s))}} \times \left[\left(V(\sigma(s)) + 1 - V^T_{\tau(\sigma(s))} \right)^2 - \left(V(\sigma(s)) - V^T_{\tau(\sigma(s))} \right)^2 \right], \end{aligned} \tag{2.57}$$

which can be simplified to,

$$\begin{aligned} \Delta\mathcal{H}_{\text{volume}} = (1 - \delta_{0\sigma(t)}) \frac{\lambda_{\tau(\sigma(t))}}{V^{T^2}_{\tau(\sigma(t))}} \left[1 - 2 \left(V(\sigma(t)) - V^T_{\tau(\sigma(t))} \right) \right] \\ + (1 - \delta_{0\sigma(s)}) \frac{\lambda_{\tau(\sigma(s))}}{V^{T^2}_{\tau(\sigma(s))}} \left[1 + 2 \left(V(\sigma(s)) - V^T_{\tau(\sigma(s))} \right) \right], \end{aligned} \tag{2.58}$$

where it is implied that there is no energy variation associated with background expansion and contraction.

Including Durotaxis

With the coordinates of elements t and s it is easy to define the direction of movement (Fig. 2.8). Let $\mathbf{v}^{(s)}$ be a unit vector that represents the direction of source's cell expansion and $\mathbf{v}^{(t)}$ the unit vector depicts the direction of the target's cell retraction. It is easy to see that for any such iteration, $\mathbf{v}^{(s)} = \mathbf{v}^{(t)} = \mathbf{v}$. Having calculated the displacements in each node, it is easy to recover the strain at the center of each element through equation (2.42) at $(\xi = 0, \eta = 0)$. Let $\lambda_1^{(e)}$ and $\lambda_2^{(e)}$ be the eigenvalues and $\mathbf{v}_1^{(e)}$ and $\mathbf{v}_2^{(e)}$ the eigenvectors of the strain tensor calculated at the center of element e, by solving the equation (A.7). In order to describe durotaxis, there must be a lower energy for cell expansions in each of those directions and an energy gain when a cell retracts from them. Therefore, the variation of the Hamiltonian should be of the form

$$\Delta\mathcal{H}_{\text{durotaxis}} = \Delta\mathcal{H}_{\text{durotaxis}}^{\text{retraction}} - \Delta\mathcal{H}_{\text{durotaxis}}^{\text{expansion}}. \tag{2.59}$$

Under the assumption that each element senses the mechanical properties of its adjacent elements, the target's cell senses strain in the source element and the source's cell senses strain in the target element. Each of the terms in equation (2.59) could be described by

$$\Delta\mathcal{H}_{\text{durotaxis}}^{\text{expansion}} = (1 - \delta_{0\sigma(s)}) \left[f(\lambda_1^{(t)})(\mathbf{v} \cdot \mathbf{v}_1^{(t)})^2 + f(\lambda_2^{(t)})(\mathbf{v} \cdot \mathbf{v}_2^{(t)})^2 \right], \tag{2.60}$$

and

$$\Delta\mathcal{H}_{\text{durotaxis}}^{\text{retraction}} = (1 - \delta_{0\sigma(s)}) \left[f(\lambda_1^{(s)})(\mathbf{v} \cdot \mathbf{v}_1^{(s)})^2 + f(\lambda_2^{(s)})(\mathbf{v} \cdot \mathbf{v}_2^{(s)})^2 \right], \tag{2.61}$$

where $f(\lambda)$ is positive and returns the energy associated with the ECM stiffness, that is, the Young's modulus E the cell perceives.

Empirically, most biological tissues exhibit a phenomenon called strain stiffening, in which the Young's modulus increases with the extension of the substrate. However the ECM was described as a linear elastic isotropic material which does not exhibit this effect. In this model, strain stiffening will be implemented only at the CPM level, when evaluating stiffness, that is, in the $f(\lambda)$ function. Given an element with stiffness E_0, the strain stiffening, for small strains, is

$$E(\lambda) = \max \left\{ E_0 \left(1 + \frac{\lambda}{\epsilon_0} \right), E_0 \right\} \tag{2.62}$$

where ϵ_0 is a stiffening parameter. For low E, focal adhesions can't mature, leading to null durotaxis contribution, however, after a certain value of rigidity FAs start to develop until they reach maximum maturity. Therefore, because durotaxis depends on the number and size of the FAs, $f(E(\lambda))$ should have a similar behavior. For that effect, the expression for f that's going to be used is a sigmoid function,

$$f(E) = \frac{\alpha}{1 + e^{-\beta(E - E_{1/2})}}, \tag{2.63}$$

although it might be described by other expressions for f.

The total variation of energy, in a given CPM step, is simply,

$$\Delta\mathcal{H} = \Delta\mathcal{H}_{\text{adhesion}} + \Delta\mathcal{H}_{\text{volume}} + \Delta\mathcal{H}_{\text{durotaxis}}, \tag{2.64}$$

given by equations (2.56), (2.58) and (2.59).

Transition Between Configurations

Assuming that the system is in thermal equilibrium with its surroundings, that is, there is a heat reservoir, it may exchange energy with it. That way, the total energy within the system may vary. Furthermore, the probability distribution over all configurations is such that it maximizes entropy. Let the average energy of the system of N different configurations be

$$\langle E\rangle = \sum_{n=1}^{N} p_n E_n, \tag{2.65}$$

where E_n is the energy of state n and p_n is the probability of the system being in that state, and abides by

$$\sum_{n=1}^{N} p_n = 1. \tag{2.66}$$

The entropy of a system (in statistical mechanics) is given by

$$S = -\sum_{n=1}^{N} p_n \ln(p_n). \tag{2.67}$$

Introducing the average energy expression and the normalization of p_n as restrictions, the entropy becomes,

$$S^* = -\sum_{n=1}^{N} p_n \ln(p_n) - \alpha\left(\sum_{n=1}^{N} p_n - 1\right) - \beta\left(\sum_{n=1}^{N} p_n E_n - \langle E\rangle\right), \tag{2.68}$$

where α and β are Lagrange multipliers. Maximizing entropy requires differentiating the last expression with respect to p_n and equating it to zero, that is,

$$\sum_{n=1}^{N} \left[-\ln(p_n) - 1 - \alpha - \beta E_n\right] = 0, \tag{2.69}$$

Therefore, for each configuration, its probability is

$$p_n = e^{-1-\alpha-\beta E_n} \propto e^{-\beta E_n}, \tag{2.70}$$

where β defines the magnitude of energy fluctuations. In fact, if $\beta \to 0$, any configuration becomes equally probable and exhibits high fluctuations; if $\beta \to +\infty$, every probability goes to (at first glance) zero. However, because probability must be normalized, the state with less

energy is infinitely more probable than any other and, thus, is the only accessible configuration of the system, and, therefore, it has no energy fluctuations. The same argument could be made if it was chosen a plus sign, only then the system would prefer higher energies instead of lower ones, which does not actually happen. This probability distribution is called the Boltzmann distribution and has a central role in statistical mechanics.

Because of this, not all CPM steps are equally probable. Promoting the configuration to a random variable, it is possible to describe the stochastic nature of biology by using a Markov chain. This chain is characterized by the states of the system and the transition probabilities between them. Let $p(x|x')$ be the probability of transition from the configuration x' to x. Starting a Markov chain with a certain initial probability distribution $p^{(0)}(x)$, the posterior probability distributions are

$$p^{(n+1)}(x) = \sum_{x'} p^{(n)}(x')p(x|x'). \tag{2.71}$$

By the ergodicity argument, after a large number of steps, if a stationary distribution exists, the system will converge to $\pi(x)$, such that,

$$\pi(x) = \sum_{x'} \pi(x')p(x|x'). \tag{2.72}$$

Additionally, another condition sufficient to ensure invariance is the reversibility condition, also called detailed balance,

$$\pi(x)p(x'|x) = \pi(x')p(x|x'). \tag{2.73}$$

Fortunately, the process by which a new configuration, for a Markov chain, is randomly selected can be separated into the random choice of a candidate, according to some probability distribution $q(x', x)$, and to randomly accept it, according to some other distribution, $\alpha(x', x)$, such that it preserves the reversibility condition. That is, the conditional probability becomes

$$p(x'|x)_{\text{MH}} = q(x', x)\alpha(x', x), \tag{2.74}$$

this strategy for picking a new configuration is called the Metropolis-Hastings algorithm, and the reversibility condition is, accordingly,

$$\pi(x)q(x', x)\alpha(x', x) = \pi(x')q(x, x')\alpha(x, x'). \tag{2.75}$$

Therefore, in order to maintain the reversibility, the probability of acceptance is given by

$$\alpha(x', x) = \begin{cases} 1 & \text{if } \pi(x)q(x', x) \geq \pi(x')q(x, x') \\ \frac{\pi(x')q(x,x')}{\pi(x)q(x',x)} & \text{if } \pi(x)q(x', x) < \pi(x')q(x, x') \end{cases}, \tag{2.76}$$

or simply,

$$\alpha(x', x) = \min\left\{1, \frac{\pi(x')q(x, x')}{\pi(x)q(x', x)}\right\}. \tag{2.77}$$

Notably, if the candidate choice probability distribution is such that $q(x', x) = q(x, x')$, then the acceptance probability is,

$$\alpha(x', x) = \min\left\{1, \frac{\pi(x')}{\pi(x)}\right\}. \tag{2.78}$$

Thus, the strategy used for taking a CPM step is to choose randomly, with equal probability, a target element and a random source in its neighborhood, also with equal probability, as a candidate transition. By having the new configuration chosen this way, the condition $q(x', x) = q(x, x')$ is met. Afterwards, the step is taken, or not, according to (2.78), where $\pi(x)$ and $\pi(x')$ are the probability of those configurations in conditions of equilibrium, that is, using the Boltzmann distribution. Therefore the acceptance rate is simply,

$$\alpha(x', x) = \min\left\{1, \frac{\pi(x')}{\pi(x)}\right\} = \min\left\{1, \frac{e^{-\beta E_{x'}}}{e^{-\beta E_x}}\right\} = \min\left\{1, e^{-\beta\Delta\mathcal{H}}\right\}, \tag{2.79}$$

where $\Delta\mathcal{H}$ is calculated through equation (2.64).

Additionally, by using energy constants in units of β the acceptance rate can be rewritten as

$$\alpha(x', x) = \min\left\{1, e^{-\Delta\mathcal{H}}\right\}. \tag{2.80}$$

The Metropolis-Hastings algorithm is one of many Markov chain Monte Carlo (MCMC) methods for sampling from probability distribution functions.

However, in order to relate a CPM step to a time step, in MCMC methods it is typically performed a certain number of steps at a time, called a Monte Carlo step. Because, biologically, every region in space can take a step simultaneously, a Monte Carlo step is usually taken to be either a sweep across all the lattice and to do a CPM step (copy attempt) for every possible element, or, for every element in the lattice, a random CPM step. For the reason that biological systems' stochasticity plays a fundamental role, the latter option is used in this model.

2.3 Traction Forces

The only missing piece in the model is how cells apply forces to the matrix, specifically to the nodes of the FEM's elements under conditions of plane stress, that is, parallel to the ECM. Under the assumption that the traction force exerted by a cell can be predicted by its shape, a rather simple model can be used. In this specific case, following the predictive model proposed by Lemmon and Romer [37], each node belonging to a cell pulls every other node of the same cell with a force proportional to the distance between nodes.

The force applied to node n by cell σ is,

$$\mathbf{f}_n^{(\sigma)} = \mu_{\tau(\sigma)} \sum_{m\in\sigma} \mathbf{d}_{nm}, \tag{2.81}$$

where μ_τ is the force per unit length a node, of cell of type τ, pulls on another node of the same cell, and $\mathbf{d}_{nm}$ is the vector difference in positions of nodes n and m, that is, $\mathbf{x}_m - \mathbf{x}_n$ (Fig. 2.9). Effectively, the cell force constant should be in units of stress, however, in order

to simplify, the constant used here already takes into consideration the thickness of the ECM, which was chosen to be $t = 10$ μm, and it is scaled in order for $\mu = 1$ to correspond to a force of 10^{-5} $\mu\text{N}\mu\text{m}^{-1}$.

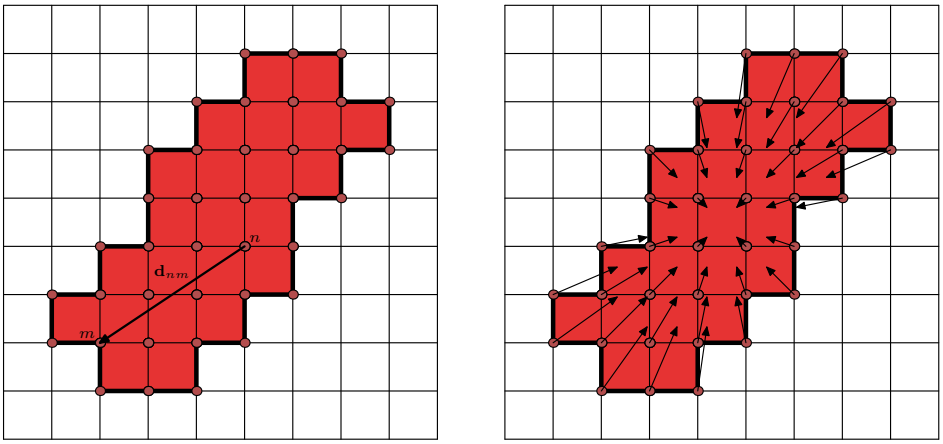

FIGURE 2.9: Schematic representing how the force acting on node n is calculated. The expression from equation (2.81) means that node n is pulled towards every other node m, belonging to the same cell, with force $\mu_{\tau(\sigma)}\mathbf{d_{nm}}$. On the right, its represented the resulting distribution of forces acting upon the ECM due to that cell.

The total force applied to a node n, if it belongs to different cells, is simply,

$$\mathbf{f}_n = \sum_{\sigma} \mathbf{f}_n^{(\sigma)}. \tag{2.82}$$

This way, it becomes a simple procedure and ties the hybrid model together. All that is left is to place the forces, conveniently indexed, inside a vector, $\mathbf{f}$, for the FEM, and to solve for displacements.

Chapter 3

Implementation and Analysis

In this chapter it will be discussed the implementation of the studied model, which is a hybrid model consisting of a discrete CPM coupled with a continuous FEM model for elasticity, summarized in Fig. 3.1. This is followed by the description of the analysis tools used, not only in the conceptualization of the CPM, but also in the post-process parsing of data, namely, the Connected Component Analysis (CCA).

Firstly, it must be stated the initial state of tags. A straightforward way to add cells is to simply flip the tag of a single element from zero to whatever tag that has not been used yet. However such states result in a large number of thermalisation CPM steps, because cells also need to reach volumes around the average value, before resembling a viable configuration. Alternatives include flipping a patch, with a volume around the target one, instead of a single element, but problems also arise from overlapping with other patches, being out of bounds and there is also the ambiguity related to the initial shape of a particular patch (rasterized circles, squares, rectangles, random shapes, ...). To add initial cells, the prior approach is used here, because of its simplicity. Also, during this initialization, cell types must be assigned and parameters must also be defined.

After the CPM is initialized, the FEM must also be set up, that is, the global stiffness matrix must be assembled. First, however, each element must have a defined value of the Young's modulus and Poisson ratio, and undergo the calculation of its individual stiffness matrix, which, in order to save memory, is immediately added on to the global stiffness matrix. In order to reduce the memory used by the matrix, the sparse notation is used when referring to the global matrix and its symmetry allows for further compaction. Furthermore, because fixed displacement boundary conditions are going to be used, the global matrix will be reduced, that is, simplified accordingly, which is explained in detail in the FEM section of this chapter.

The main loop is chosen to be one CPM Monte Carlo step followed by force calculation and FEM calculation. However, for the CPM to precede the FEM, displacements must be estimated. Therefore, before the main loop, there should be a calculation of the forces that the initial configuration of cells apply to the ECM, followed by a single FEM calculation. However, we have chosen to skip that step and to replace it with initial null displacements. It is convenient because it saves up code repetition before the main loop, and also because it reduces the number of FEM calculation steps, the bottleneck of the model. Furthermore, it makes the implementation more simple and less cluttered. In exchange, however, the first

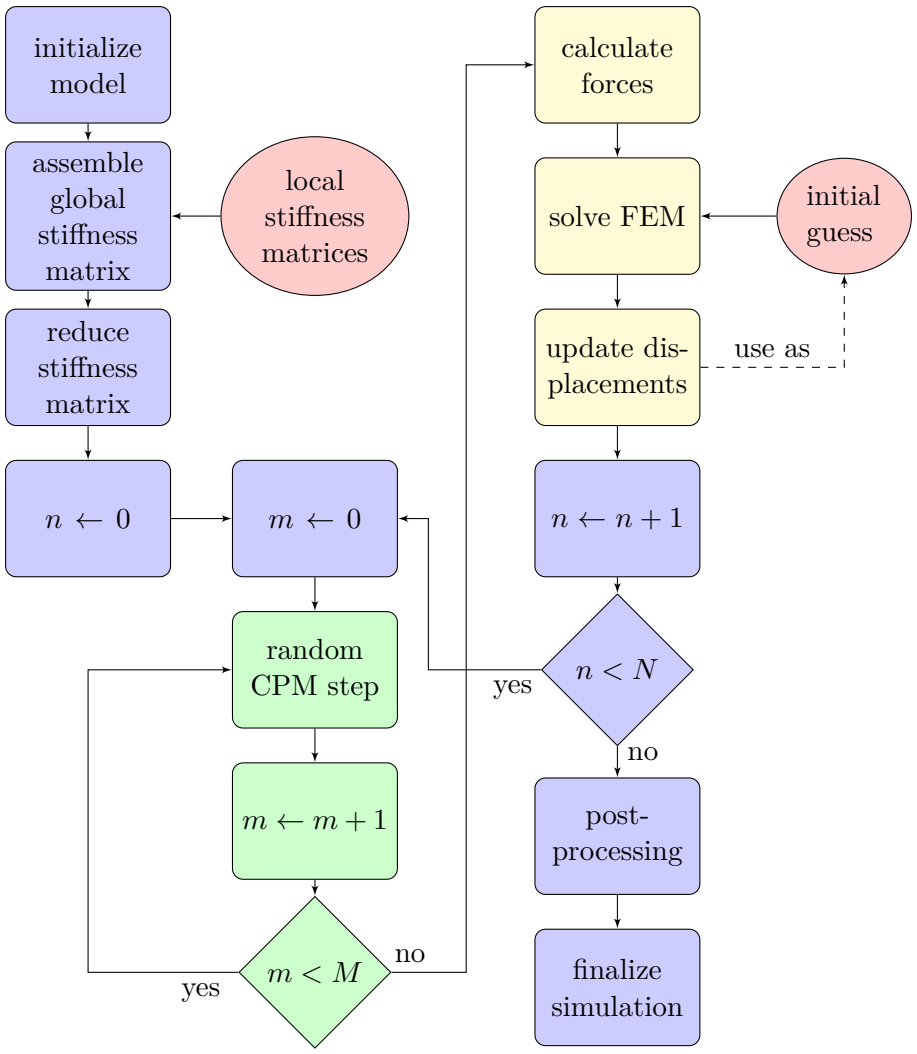

FIGURE 3.1: Flowchart representing the main components of the model's implementation. Initialization includes setting the initial cell tags and corresponding types, elements' mechanical properties and the parameters of each cell type. Then the global stiffness matrix is assembled from each element's local stiffness matrix, calculated according to its mechanical properties using equation (2.48). The resulting matrix can be simplified (reduced) under certain boundary conditions. Each iteration n consists of M CPM copy attempts (which is a Monte Carlo step/sweep, when M is equal to the number of elements in the domain), calculation of the force applied to the ECM and solving the FEM equations using the previous displacements as an initial guess (or a null vector if $n = 0$). After N iterations, information is extracted from the resulting configuration and the simulation ends.

Monte Carlo step is, at first glance, compromised. That is not the case, because, by choosing single element cells as an initial condition, the forces these cells apply are small, leading to a negligible durotaxis energy term, completely outweighed by the volume term of any acceptable CPM step at this stage, rendering the durotaxis term, in the first iteration, utterly irrelevant.

3.1 CPM model

In each iteration of the main loop, a Monte Carlo step, a fixed number of CPM copy attempts, as described in section 2.2, is taken. A Monte Carlo step usually has a number of CPM attempts equal to the number of elements, allowing for each element undergo change independently. Due to the stochastic nature of the processes being studied, it has been chosen to take CPM steps with random targets and sources. Each CPM copy attempt (Fig. 3.2) has three distinct stages.

First, the random target and random source, from the target's neighborhood, are selected (excluding target elements on the boundary). Then, this particular step undergoes a selection process by which it is discarded if it is deemed unacceptable. It is disregarded if:

- Target and source belong to the same cell, corresponding to a redundant step;

- Target is a cell and:
  - Target cell will break;

  - Target cell would vanish, that is, target element is the cell's only element (target volume is 1).

Finally, if deemed acceptable, the step is taken according to the acceptance probability discussed in section 2.2, that is, the energy variation, $\Delta\mathcal{H}$, is calculated and, if it is negative, the step is accepted, or else, if it is positive, the copy is accepted with probability $e^{-\Delta\mathcal{H}}$.

The target cell's connectivity is checked using CCA, which will be discussed in the last section of this chapter. Here, breaking connectivity refers to a step that, given a target cell element, results in two or more separate domains with the same tag (Fig. 3.3).

However, it is not always necessary to resort to CCA. A simple preliminary check is to inspect if the target's neighborhood is connected even with the target not belonging to the cell. If they are connected with each other regardless of the target, the step does not compromise connectivity, however, if the neighborhood is not connected if not for the target, connectivity is not ensured and the CCA needs to be applied.

3.2 FEM model

Stepping back a bit, regarding the grid upon which this model is built, a single index is used for elements and another for nodes. In a $N \times M$ element grid, the index of an element starts

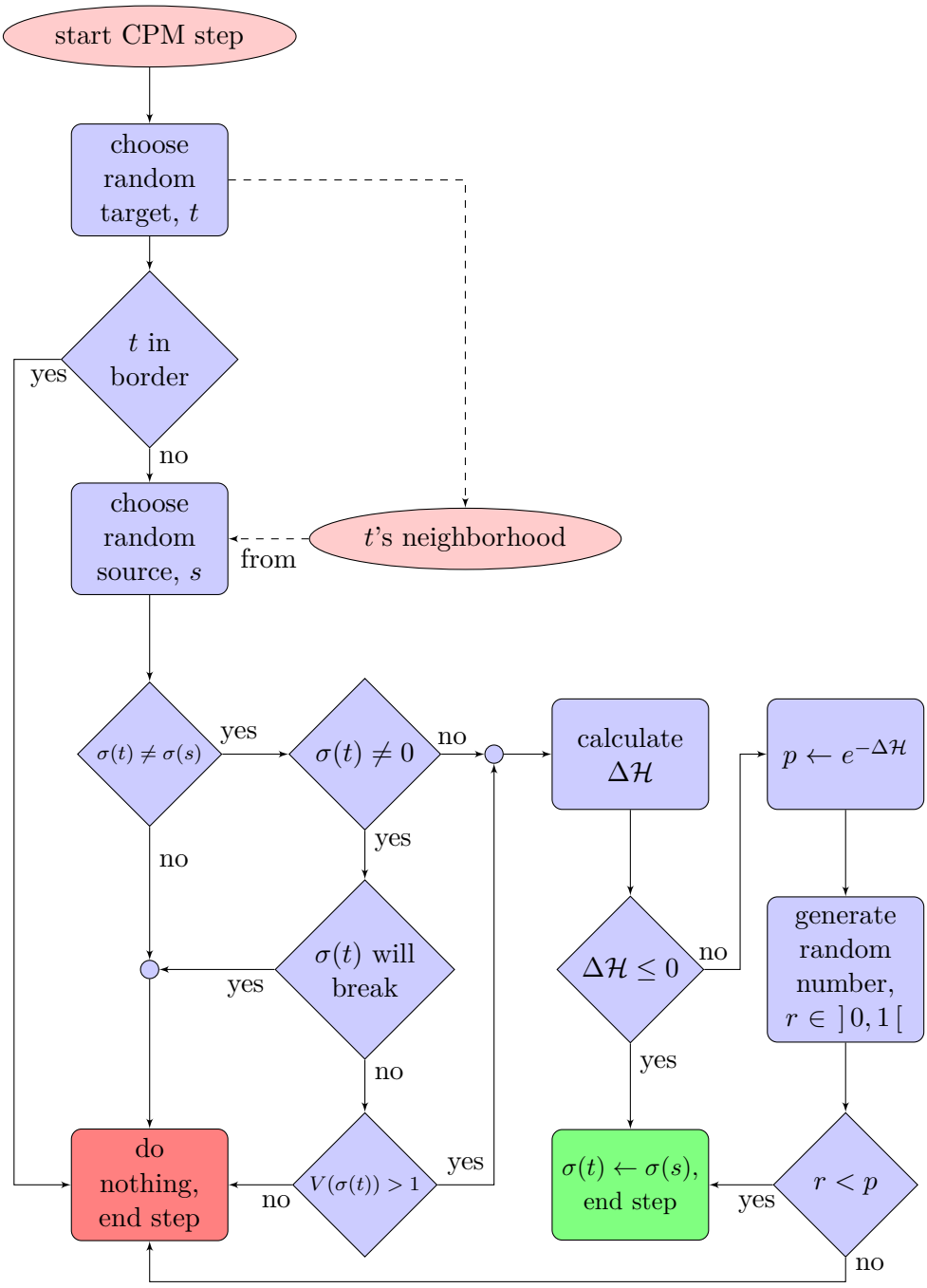

FIGURE 3.2: Flowchart representing the process of a randomly taken CPM step. Boundary is immediately excluded, in order for the target's (t) neighborhood to be defined. The source (s) is randomly taken from the neighborhood of t. If the tag is the same ($\sigma(t) = \sigma(s)$), the initial and final states would be the same and, as such, it is redundant. If t is a cell ($\sigma(t) \neq 0$), then additional checks have to be made, namely, respecting connectivity and making sure the cell doesn't vanish. After initial checks have been made and the move is not discarded *a priori*, energy difference ($\Delta\mathcal{H}$) is calculated. If favorable ($\Delta\mathcal{H} \leq 0$), the move is automatically accepted, if not, the probability ($p = e^{-\Delta\mathcal{H}}$) of the step being taken is calculated, and is accepted accordingly.

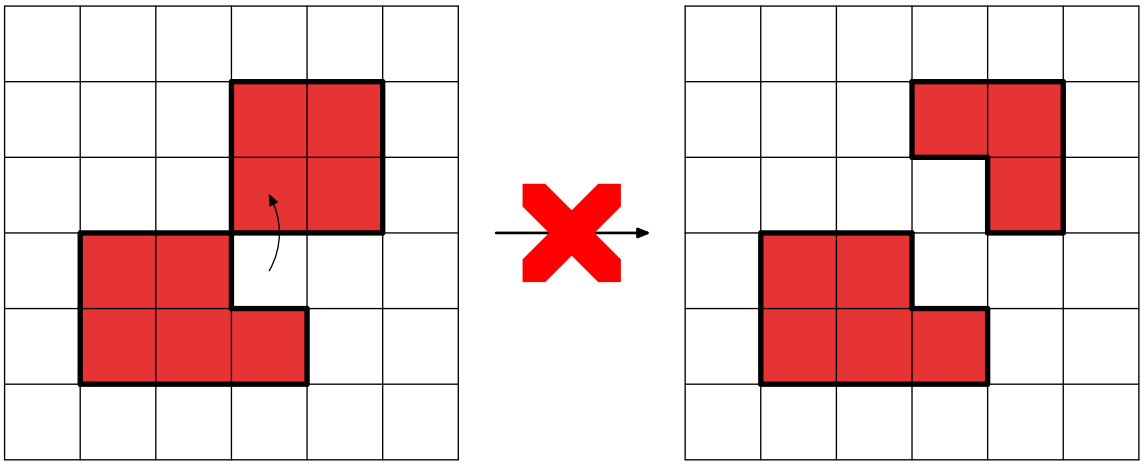

FIGURE 3.3: Example of a CPM step (the arrowhead is in the target element and the arrow's origin element is the source) that would break connectivity. If the two regions on the right were connected by any other means aside from the target, then the move would have been permitted. However, that is not the case and, therefore, this move is prohibited. In order to check if a move breaks connectivity, a Connected Component Analysis (CCA) algorithm, discussed in section 3.3, is used.

at 0 and the last index is $N \times M - 1$. Single index to matrix indices relations are obtained by using the integer division operation ($\text{int}\,(a/b)$) and the *modulus* operation ($a\%b$). Let i and j denote the matrix indices (position) of an element ($i = 0, 1, \ldots, N-1$ and $j = 0, 1, \ldots, M-1$), the single index can be built as $k = iM + j$ and, because it is unique for each i and j, it can be extracted from k, $i = \text{int}\,(k/M)$ and $j = k\%M$. For nodes, although the grid is of size $(N+1) \times (M+1)$, the relation is analogous, with $M+1$ instead of M. The force and displacement vectors have two components, therefore, in order for the assembled stiffness matrix to be two-dimensional, each degree of freedom must have one unique index. Let k denote the index of a node, the index corresponding to that node's displacement projection along the x-axis is $2k$ and along the y-axis is $2k+1$. An example of the resulting labeling is presented on Fig. 3.4.

A relation of indices from local to global is needed for the assembly of the global stiffness matrix. Using this labeling, it is easy to see that for an element index e, with position $i = \text{int}\,(e/M)$ and $j = e\%M$, its global nodes have positions $(i, j), (i+1, j), (i+1, j+1), (i, j+1)$ (in the order of local nodes). By reverting back to a single index, one can define a vector (using the element index as a parameter) relating an index, representing a local degree of freedom, to the respective component, representing the global index.

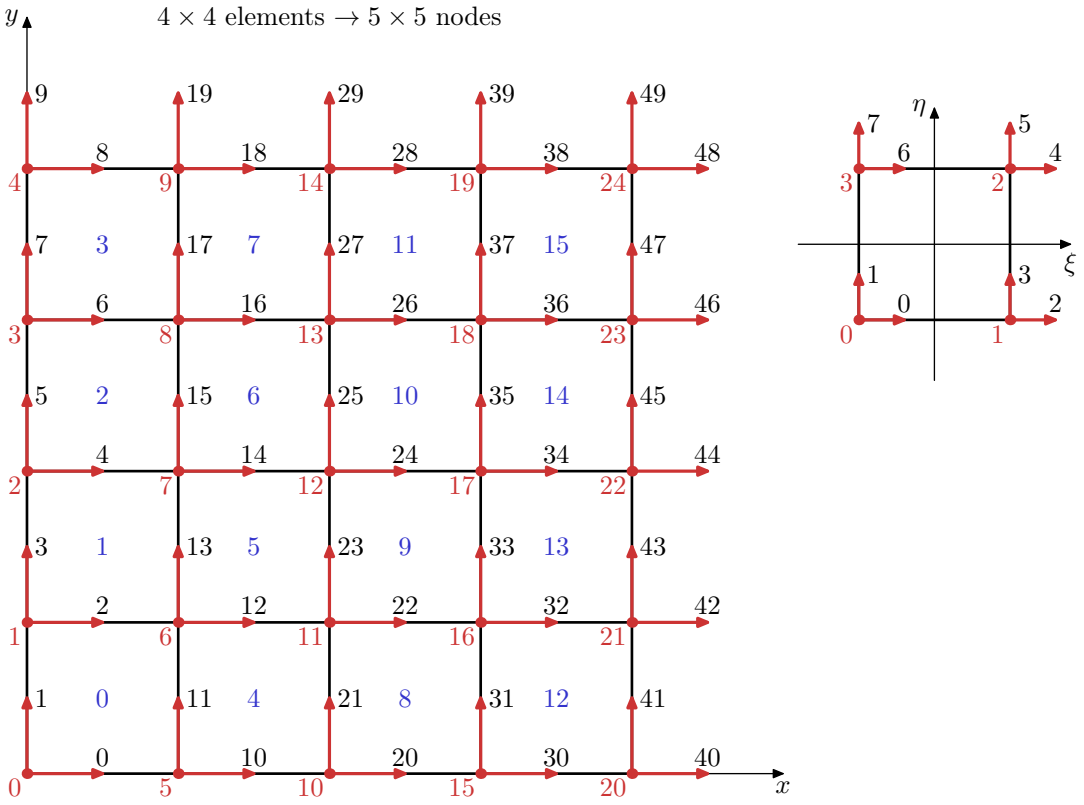

FIGURE 3.4: Domain configuration of $N \times M$ elements, $(N+1) \times (M+1)$ nodes, with $N = M = 4$. The indexation chosen, for elements (blue), nodes (red) and degrees of freedom (black), is a single index, implying a contiguous memory storage. For comparison, the local frame of reference used in the derivation of the FEM equations is also represented. For global stiffness matrix assembly a correspondence between local and global indices is needed (for a certain element). For the calculation of the force vector, there needs to be a correspondence between a global node and the global element it belongs to, in order to discern what cells that node belongs to.

Let that vector, that takes as a parameter the element index e, be

$$\mathbf{T}_I(e) = \underbrace{\begin{pmatrix} 2&0&0&0\\ 2&0&0&0\\ 0&2&0&0\\ 0&2&0&0\\ 0&0&2&0\\ 0&0&2&0\\ 0&0&0&2\\ 0&0&0&2 \end{pmatrix} \underbrace{\left[\begin{pmatrix} 1&0\\ 0&1\\ 0&1\\ 1&0 \end{pmatrix} \underbrace{\left[\underbrace{(e+\operatorname{int}(e/M))}_{\text{lower left corner node}} \begin{pmatrix} 1\\1 \end{pmatrix} + \begin{pmatrix} 0\\ M+1 \end{pmatrix} \right]}_{\text{and the node on its right}} + \begin{pmatrix} 0\\0\\1\\1 \end{pmatrix} \right]}_{\text{and the nodes above them (in the local node order)}} + \begin{pmatrix} 0\\1\\0\\1\\0\\1\\0\\1 \end{pmatrix}}_{\text{even/odd}\leftrightarrow\text{x/y degrees of freedom indices}},$$

i.e.:

$$\mathbf{T}_I(e) = \begin{pmatrix} 2\left[e+\operatorname{int}(e/M)\right] \\ 2\left[e+\operatorname{int}(e/M)\right]+1 \\ 2\left[e+\operatorname{int}(e/M)+M+1\right] \\ 2\left[e+\operatorname{int}(e/M)+M+1\right]+1 \\ 2\left[e+\operatorname{int}(e/M)+M+2\right] \\ 2\left[e+\operatorname{int}(e/M)+M+2\right]+1 \\ 2\left[e+\operatorname{int}(e/M)+1\right] \\ 2\left[e+\operatorname{int}(e/M)+1\right]+1 \end{pmatrix}. \tag{3.1}$$

This way, following an example from Fig. 3.4, for element $e = 10 = 2 \times 4 + 2$

$$\mathbf{T}_I(10) = \begin{pmatrix} 24\\25\\34\\35\\36\\37\\26\\27 \end{pmatrix}.$$

Therefore, for the element e let $\mathbf{u} = \mathbf{T}_I(e)$, the local matrix elements $K_{ij}^{(e)}$ correspond directly to element $K_{u_i u_j}$ of the global matrix, $\mathbb{K}$.

Because theelements have all the same shape, the only difference between the local stiffness matrices comes from the values of ν and E. If ν is kept constant, the stiffness matrix can be calculated only once for some E_0 and, because it is proportional to the Young's modulus, simply multiplied by some factor to give the stiffness matrix of an element of Young's modulus, E.

Therefore, for constant ν, the local stiffness matrix is calculated for some E_0 (for an hypothetical element e_0). Then, for each element, the contribution of $\mathbb{K}^{(e)} = \frac{E^{(e)}}{E_0}\mathbb{K}^{(e_0)}$ is added to element $K_{u_i u_j}$, where $\mathbf{u} = \mathbf{T}_I(e)$. If ν is not constant, for each element, a stiffness matrix must be calculated (for $\nu^{(e)}$ and $E^{(e)}$).

ALGORITHM 1: Algorithm for the assembly of the stiffness matrix. In a $N \times M$ element grid there are $(N+1)\times(M+1)$ nodes, hence $\mathcal{N} = 2(N+1)(M+1)$ degrees of freedom. For each element, the local stiffness matrix ($\mathbb{K}^{(e)}$) is calculated. Let $\mathbf{T}_I(e)$ be the vector that relates local matrix indices (0 through 7) to the corresponding global ones (0 through $\mathcal{N}-1$) of a given element e. The elements of $\mathbb{K}^{(e)}$ are added into the global matrix $\mathbb{K}$ with the correct indices. If one chooses to take advantage of the sparse nature of $\mathbb{K}$, then appropriate changes to the algorithm are needed.

Data: the size of the element grid, $N \times M$; the Young's modulus for each element, $E^{(e)}$; the Poisson's ratio for each element $\nu^{(e)}$; the length of the square element's side, L;
Result: the assembled total stiffness matrix $\mathbb{K}$;
$\mathcal{N} \leftarrow 2\,(N+1)\,(M+1)$;
allocate matrix $\mathbb{K}$ of size $\mathcal{N} \times \mathcal{N}$;
fill $\mathbb{K}$ with zeros;
for $e \leftarrow 0, 1, \ldots, N \times M - 1$ **do**
  calculate the (8×8) matrix $\mathbb{K}^{(e)}$, (2.48), with $E = E^{(e)}$, $\nu = \nu^{(e)}$ and L;
  let $\mathbf{u}$ be a vector of size 8;
  $\mathbf{u} \leftarrow \mathbf{T}_I\,(e)$;
  for $i \leftarrow 0, 1, \ldots, 8$ **do**
    for $j \leftarrow 0, 1, \ldots, 8$ **do**
      $K_{u_i u_j} \leftarrow K_{u_i u_j} + K^{(e)}_{ij}$, according to (2.51) and (appendix F);
    end
  end
end

After assembling the global stiffness matrix (Algorithm 1), size $\mathcal{N}\times\mathcal{N}$, where $\mathcal{N}$ is the number of degrees of freedom, it can be simplified under fixed displacement boundary conditions. If index n is a fixed value, the equation becomes

$$\begin{pmatrix} K_{0\,0} & \cdots & K_{0\,n-1} & K_{0\,n} & K_{0\,n+1} & \cdots & K_{0\,\mathcal{N}-1} \\ \vdots & \ddots & \vdots & \vdots & \vdots & \ddots & \vdots \\ K_{n-1\,0} & \cdots & K_{n-1\,n-1} & K_{n-1\,n} & K_{n-1\,n+1} & \cdots & K_{n-1\,\mathcal{N}-1} \\ K_{n\,0} & \cdots & K_{n\,n-1} & K_{n\,n} & K_{n\,n+1} & \cdots & K_{n\,\mathcal{N}-1} \\ K_{n+1\,0} & \cdots & K_{n+1\,n-1} & K_{n+1\,n} & K_{n+1\,n+1} & \cdots & K_{n+1\,\mathcal{N}-1} \\ \vdots & \ddots & \vdots & \vdots & \vdots & \ddots & \vdots \\ K_{\mathcal{N}-1\,0} & \cdots & K_{\mathcal{N}-1\,n-1} & K_{\mathcal{N}-1\,n} & K_{\mathcal{N}-1\,n+1} & \cdots & K_{\mathcal{N}-1\,\mathcal{N}-1} \end{pmatrix} \begin{pmatrix} q_0 \\ \vdots \\ q_{n-1} \\ q_n \\ q_{n+1} \\ \vdots \\ q_{\mathcal{N}-1} \end{pmatrix} = \begin{pmatrix} f_0 \\ \vdots \\ f_{n-1} \\ f_n \\ f_{n+1} \\ \vdots \\ f_{\mathcal{N}-1} \end{pmatrix} \xrightarrow[\text{becomes}]{\text{if } f_n \text{ is known,}}$$

$$\begin{pmatrix} K_{0\,0} & \cdots & K_{0\,n-1} & K_{0\,n+1} & \cdots & K_{0\,\mathcal{N}-1} \\ \vdots & \ddots & \vdots & \vdots & \ddots & \vdots \\ K_{n-1\,0} & \cdots & K_{n-1\,n-1} & K_{n-1\,n+1} & \cdots & K_{n-1\,\mathcal{N}-1} \\ K_{n+1\,0} & \cdots & K_{n+1\,n-1} & K_{n+1\,n+1} & \cdots & K_{n+1\,\mathcal{N}-1} \\ \vdots & \ddots & \vdots & \vdots & \ddots & \vdots \\ K_{\mathcal{N}-1\,0} & \cdots & K_{\mathcal{N}-1\,n-1} & K_{\mathcal{N}-1\,n+1} & \cdots & K_{\mathcal{N}-1\,\mathcal{N}-1} \end{pmatrix} \begin{pmatrix} q_0 \\ \vdots \\ q_{n-1} \\ q_{n+1} \\ \vdots \\ q_{\mathcal{N}-1} \end{pmatrix} = \begin{pmatrix} f_0 - K_{0\,n}q_n \\ \vdots \\ f_{n-1} - K_{n-1\,n}q_n \\ f_{n+1} - K_{n+1\,n}q_n \\ \vdots \\ f_{\mathcal{N}-1} - K_{\mathcal{N}-1\,n}q_n \end{pmatrix}.$$

Effectively it reduces the number of rows and columns of the stiffness matrix (Fig. 3.5), hence this process is called reduction. In the course of this study, the boundary conditions will simply be that of null displacements, therefore, no alteration to the right-hand side of the equation is needed.

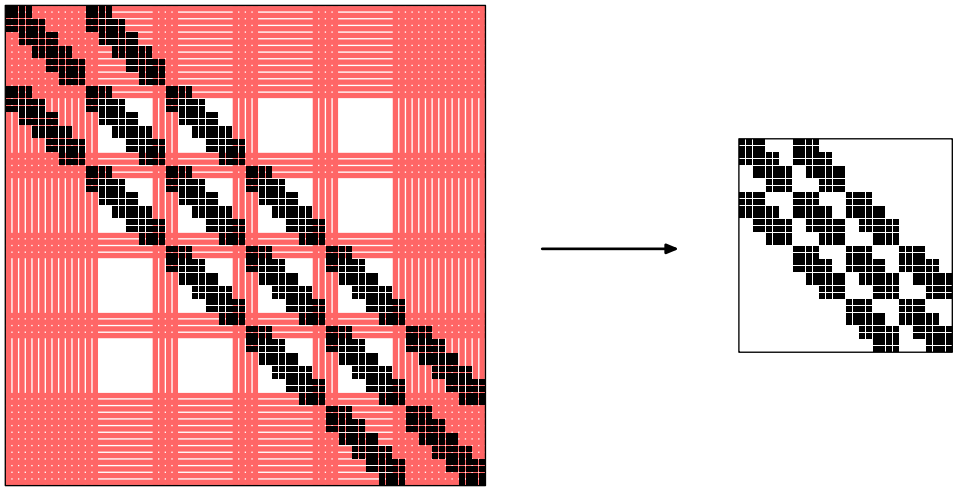

FIGURE 3.5: Using the example from Fig. 2.5, which is a 5×5 element grid (6×6 nodes), corresponding to a stiffness matrix of size 72×72. The nonzero elements of the global stiffness matrix are represented as black squares. If the displacements at the border are known, $2 \times 6 \times 6 - 2 \times 4 \times 4 = 40$ degrees of freedom are already fixed and don't need to be solved. After reduction, the stiffness matrix is the size of the remaining degrees of freedom, which, in this example, is 32. The colored rows/columns represent the removed degrees of freedom.

Inside the main loop, after the Monte Carlo step, the forces are calculated according to the model of section 2.3. For each cell, each node is checked whether it belongs to that cell and, if it does, it is added to a list that, after checking the whole grid, for each node on the list it is summed up all the contributions to the force applied on that particular node by every other node on that same list. This process is more thoroughly described in algorithm 2.

In order to ascertain if a certain node n belongs to a cell σ, the node's surrounding elements, to which n belongs to, need to be checked for that particular tag. If at least one of those elements has the tested tag, σ, then n belongs to σ.

Therefore, a correspondence between node n and its four adjacent elements is needed and takes the form of, for example,

$$\mathbf{T}_{II}(n) = \underbrace{\begin{pmatrix} 1 & 0 \\ 0 & 1 \\ 1 & 0 \\ 0 & 1 \end{pmatrix} \underbrace{\left[\begin{pmatrix} 1 \\ 1 \end{pmatrix} \underbrace{(n - \operatorname{int}(n/(M+1)))}_{\text{top right element}} - \begin{pmatrix} 0 \\ M \end{pmatrix} \right]}_{\text{and the element on its left}} - \begin{pmatrix} 0 \\ 0 \\ 1 \\ 1 \end{pmatrix}}_{\text{and the elements below them}},$$

$$\mathbf{T}_{II}(n) = \begin{pmatrix} n - \text{int}\left(n/\left(M+1\right)\right) \\ n - \text{int}\left(n/\left(M+1\right)\right) - M \\ n - \text{int}\left(n/\left(M+1\right)\right) - 1 \\ n - \text{int}\left(n/\left(M+1\right)\right) - M - 1 \end{pmatrix}, \tag{3.2}$$

noting that its validity rests on the fact that the node n is not a boundary node. Taking an example from Fig. 3.4, node $n = 16 = 3(4+1)+1$ belongs simultaneously to elements

$$\mathbf{T}_{II}(16) = \begin{pmatrix} 13 \\ 9 \\ 12 \\ 8 \end{pmatrix}.$$

ALGORITHM 2: Implementation of the traction force model, in order to obtain the force vector. The force vector, initially null, is built from the contributions of each cell, one at a time. Firstly, the node grid is scouted for nodes belonging to the current cell and are added to a list. Afterwards, the contribution of each node pulling on each other node, in the same cell, is added to the force vector, one pair at a time. $\mathbf{T}_{II}(n)$ is simply a vector containing the indices of the elements that contain the node n.

Data: the size of the element grid, $N \times M$; the CPM tags, $\sigma(e)$; the cell types $\tau(\sigma)$; the traction force constants μ_τ;
Result: the force vector $\mathbf{f}$;
fill vector $\mathbf{f}$, of size $2 \times N \times M$, with zeros;
for *each cell,* σ **do**
  let l be an empty list;
  for *each node,* n*, not at a boundary* **do**
    $\mathbf{v} \leftarrow \mathbf{T}_{II}(n)$;
    for $i \leftarrow 0, 1, 2, 3$ **do**
      $e \leftarrow \mathbf{v}_i$;
      if $\sigma(e) = \sigma$ **then**
        add n to list l;
        go to next node;
      end
    end
    for *each node,* n_1*, of* l **do**
      for *every other node,* n_2*, of* l **do**
        $\Delta x \leftarrow L\left(\text{int}\left(\frac{n_2}{M+1}\right) - \text{int}\left(\frac{n_1}{M+1}\right)\right)$;
        $\Delta y \leftarrow L(n_2 \% (M+1) - n_1 \% (M+1))$;
        $f_{2n_1} \leftarrow f_{2n_1} + \mu_{\tau(\sigma)} \Delta x$;
        $f_{2n_1+1} \leftarrow f_{2n_1+1} + \mu_{\tau(\sigma)} \Delta y$;
      end
    end
  end
end

After calculating the forces applied on the ECM, the equation $\mathbb{K}\mathbf{q} = \mathbf{f}$ is solved for $\mathbf{q}$, using a PCG solver. This solver is described in the algorithm 3 using the present displacements as an initial guess. The preconditioning matrix used is simply the diagonal of $\mathbb{K}$. Moreover, by taking advantage of the symmetry and sparseness of the matrix $\mathbb{K}$, the steps which involve the product of a matrix by a vector can be optimized.

ALGORITHM 3: Given the stiffness matrix, $\mathbb{K}$ and the force vector, $\mathbf{f}$, the PCG proceeds according to this algorithm, using the diagonal of $\mathbb{K}$ as the preconditioner. As a result it calculates the displacements on each node. As an initial guess, it uses the previously calculated displacements. Because the stiffness matrix is typically sparse and symmetric, the algorithm might change slightly according to how memory is stored.

Data: the force vector, $\mathbf{f}$; the stiffness matrix, $\mathbb{K}$; the initial guess vector, $\mathbf{x_0} = \mathbf{q}$, that is, the previous displacements; the maximum number of iterations, n; the desired precision, δ;

Result: the displacement vector $\mathbf{q}$, equal to the resulting vector $\mathbf{x}$;

using the preconditioning matrix: $\mathbb{M} \leftarrow \mathrm{diag}\,(\mathbb{K})$;

$\mathbf{r_0} \leftarrow \mathbf{f} - \mathbb{K}\mathbf{x_0}$;

$\mathbf{p_0} \leftarrow \mathbb{M}^{-1}\mathbf{r_0}$;

$\epsilon_0 \leftarrow \mathbf{r_0^T}\mathbb{M}^{-1}\mathbf{r_0}$;

$\epsilon \leftarrow \mathbf{f^T}\mathbb{M}^{-1}\mathbf{f}$;

$i \leftarrow 0$;

while $\delta < \frac{\epsilon_i}{\epsilon}$ *and* $i < n$ **do**

  $\mathbf{q_i} \leftarrow \mathbb{K}\mathbf{p_i}$;

  $\alpha_i \leftarrow \frac{\epsilon_i}{\mathbf{p_i^T q_i}}$;

  $\mathbf{x_{i+1}} \leftarrow \mathbf{x_i} + \alpha_i \mathbf{p_i}$;

  $\mathbf{r_{i+1}} \leftarrow \mathbf{r_i} - \alpha_i \mathbf{p_i}$;

  $\mathbf{z_i} \leftarrow \mathbb{M}^{-1}\mathbf{r_{i+1}}$;

  $\epsilon_{i+1} \leftarrow \mathbf{r_{i+1}^T z_i}$;

  $\beta_i \leftarrow \frac{\epsilon_{i+1}}{\epsilon_i}$;

  $\mathbf{p_{i+1}} \leftarrow \mathbf{z_i} + \beta_i \mathbf{p_i}$;

  $i \leftarrow i + 1$;

end

the next guess: $\mathbf{x_0} \leftarrow \mathbf{x_i}$;

return: $\mathbf{q} \leftarrow \mathbf{x_i}$;

3.3 Connected Component Analysis

As already mentioned, cell connectivity needs to be preserved in each CPM step. Not only that, but assessing the morphology of the cell structures that arise (in the post-processing block of the implementation), can also (and will be) be measured through connectivity. For that reason, the tool used for mapping of connections is explained here.

Essentially, CCA, also called connected component labeling, identifies and uniquely labels connected sets of pixels according to heuristic rules, specific to the issue at hand. Furthermore, being CCA an applied concept of graph theory, a less ambiguous definition of connected pixel sets is available, that is, a group of pixels in which any two elements connected through at least one path, not including any pixel outside this set. In this case, a path is simply a set of connections, and a connection between pixels is being neighbors of one another.

However, a distinction has to be made between foreground and background pixels. These connected components refer to foreground pixels only, whereas the background is established by what is not being parsed. The first step of a CCA is to process the image into a binary background/foreground mask. The criteria by which a pixel is deemed to be part of background is entirely dependent on the problem the CCA is helping to solve. It offers a great deal of versatility on the range of its applicability and even more so when skewing the concept of neighborhood.

The algorithm used for the CCA, in this implementation, is a simple two-pass algorithm (Fig. 3.6). As the name indicates, it consists of sweeping the grid twice. The first sweep assigns new labels to foreground pixels, or the same label as already labeled neighbors. The second pass builds the connection map of pixel sets.

By keeping track of the resulting connections, it is possible to extract useful information, such as the number and size of the pixel sets.

If there are foreground pixels at the edges of the grid, any number of extra background pixel layers can be added to the edges of the grid, such that no neighbor is left undefined.

3.3.1 During the CPM step

Suppose a CPM step with target, t, might leave a cell $\sigma(t)$ disconnected. The procedure that is going to be used is to simply choose the elements with tag $\sigma(t)$, save for the target, t, as the foreground pixels. If, after the CCA, using the Moore's neighborhood (first neighbors), there is only one pixel set, the cell is connected.

3.3.2 Classifying Cell Structures

In order to classify the cell structures, by choosing the foreground as a pixel belonging to any cell, that is, an element with any tag different from zero, and skipping the first step, using the tags as labels, it is possible to map how the cells are connected. The choice of neighborhood could be loose, in the sense that it is possible to extend the range at which cells are considered connected. However it is going to be used the Moore's neighborhood, in order to take into account the fact that there is a considerable energy cost when adhering, and, by choosing otherwise, it risks obscuring transitions between bound and unbound configurations.

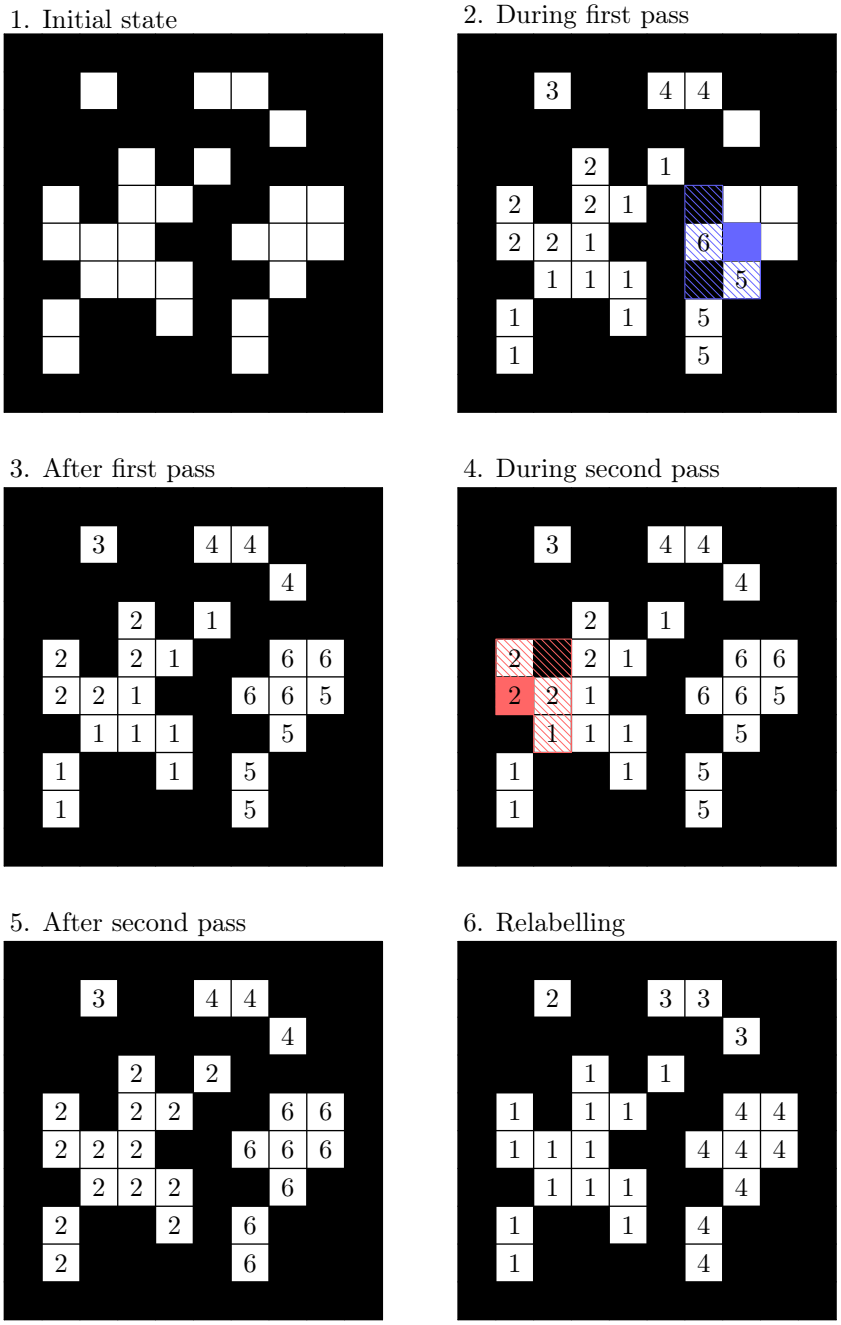

FIGURE 3.6: Given an initial state as a boolean value mask, according to what's taken to be the background, CCA allows to check how many sets of connected pixels there are in an image and the size of each set. It is used during the simulation and to interpret data. The CCA algorithm presented here, called the two-pass algorithm, is by no means the only one and it serves simply as a working example. Overlaying a label grid over the initial state and reserving the label 0 for the background, the first pass consists of giving labels to each foreground pixel. The label will represent the set to which that pixel belongs to. If the current pixel has a neighbor with a (nonzero) label, then it gets that label, if, however, there are no labeled neighbors, it gets a new label. If it has more than one labeled neighbor, it gets either label. The purpose of the second grid sweep is to merge adjacent sets. Finally, information about the size and number of sets is extracted. Relabeling is optional and done for convenience.

The first category in which structures fall into is dispersed cells. By establishing a predetermined amount of cells to be the maximum value for which they are still considered dispersed, a cell structure is classified accordingly. Which, in this case, that number was chosen to be $n < 5$. If it is not dispersed it might be a cluster or a network. The process used to separate both categories is to gauge the density, ρ, of the structure inside its circumscribed circumference. For example, taking a value proportional to the optimal circle packing density for $n = 5$, $\rho_0 \approx 0.685$ [45], and adjusting the proportionality constant γ. If $\rho > \gamma\rho_0$ then the structure is a cluster, if not, it is a mesh-like structure. The value $\gamma = 0.35$ was chosen to be as low as possible, while still being able to retain shapes resembling vessels.

3.3.3 Counting and Measuring Meshes

With the purpose to analyze the meshes (number and size) of a cell network, simply considering the pixels with tag zero as the foreground and the rest as background does not work, because all measures will be affected by the empty space outside possible cell structures, while only the domains inside are relevant. In order to push the outer pixels to the background, the whole grid must undergo an intermediate step. Making use of the aforementioned foreground selection and labeling the outer edges of the grid with the label 2, we propagate the new label to every neighboring label on the foreground, until all labels converge to a single value. Then, we flip all labels from two to zero, pushing them to the background. Finally, the CCA is applied to that result (using the first neighbors of the Moore's neighborhood).

Due to the stochastic nature of the model, cells may not form perfect enclosures and a pixel may make a large difference in this analysis. Before checking the outer pixels, some diffusion steps of the labels zero ensures that the smaller gaps are closed. Although a different number of steps might be run for this process, two were taken.

After extracting the results, each mesh smaller than the average volume (area, in this case) of a cell is ignored.

Chapter 4

Cell Culture Morphology

In the course of this chapter, for every result presented, if a parameter is not explicitly stated when referring to that result, the default parameter is used instead, presented in table 4.1.

Using the default parameters, it is possible to observe vessel-like structures. Namely, by using randomly placed cells as an initial condition, it is possible to simulate vasculogenesis (Fig. 4.1), which will be studied in more detail in section 4.1 using the previously mentioned quantitative methods.

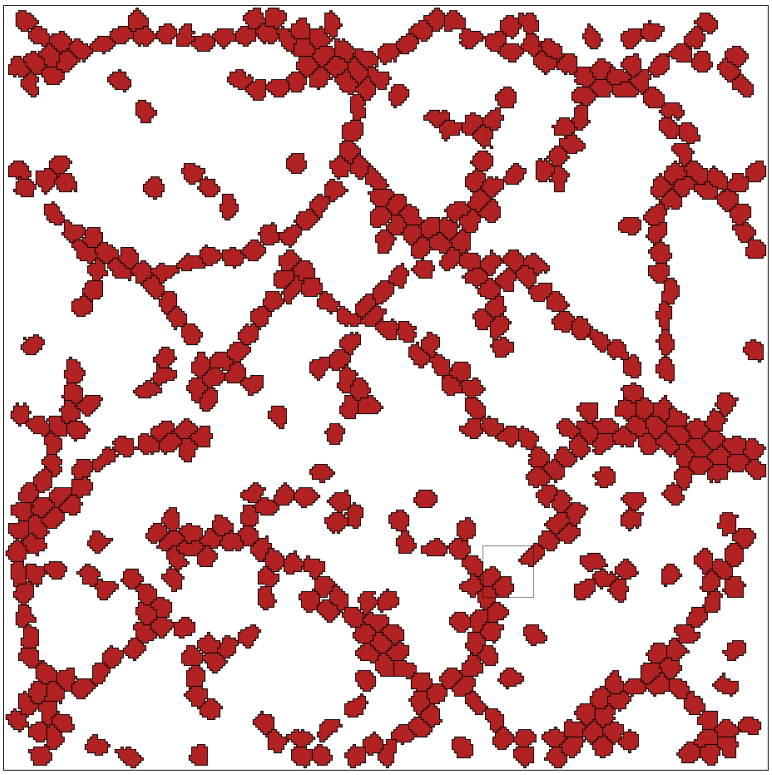

FIGURE 4.1: A simulation for five hundred cells on a 300×300 element grid, ran with the default parameters (Table 4.1). The cells are represented by enclosed colored regions, corresponding to the same σ. The color of a region corresponds to a cell type (white is reserved for the background), which means there is cells of only one type. Image obtained after five thousand Monte Carlo steps with cells initially placed randomly and with volume of one element. The smaller square is going to be zoomed in order to observe the quantities: forces (Fig. 4.2), displacements (Fig. 4.3), strains (Fig. 4.4) and tensions (Fig. 4.5). It can be observed that, under these parameters, a network of cells is an emergent pattern of the model.

TABLE 4.1: Table containing the default value of the model parameters. The indices i and j refer to cell types $i, j = 1, 2, \ldots$. Cell force constant, with units Nm^{-1} ($\mu\mathrm{N}\mu\mathrm{m}^{-1}$), is a scaled parameter such that $\mu = 1\ \mathrm{Nm}^{-1}$ corresponds to a stress of $1 \times 10^{-3}\ \mathrm{nN}\mu\mathrm{m}^{-2}$ applied to a substrate of thickness 10 μm.

Parameter	Symbol	Default Value	Units
Element side length	L	2.5	μ m
Target Volume	V_i^T	$\pi(4L)^2$	μ m^2
Volume Constraint	λ_i	500	—
Cell-ECM energy cost	J_{i0}	1.25	per side
Cell-cell energy cost	J_{ij}	2.5	per side
Strain stiffening steepness	ϵ_0	0.1	—
Durotaxis maximum value	α	10	per side
Threshold stiffness value	$E_{1/2}$	1.5×10^4	Pa
Steepness of guidance energy	β	5×10^{-4}	Pa^{-1}
Cell force constant	μ_i	1	$\mu\mathrm{N}\mu\mathrm{m}^{-1}$
Young's modulus	E	1×10^4	Pa
Poisson ratio	ν	0.45	—
Accuracy of the PCG	δ	1×10^{-5}	—

First, however, it is studied how the physical quantities relate to each other. Using the previous example, zooming in on the marked area of Fig. 4.1, it is possible to represent the forces cells apply to the ECM (Fig. 4.2), the displacements of each of the grid's nodes (Fig. 4.3), the strain each element is under (Fig. 4.4) and the corresponding stress (Fig. 4.5).

Furthermore, parameters, such as cell-cell adhesion cost, cell force and cell-ECM adhesion cost, can be interpreted biologically, for example, because cell-cell adhesion is mediated through cadherin family proteins, a drop in cell adhesion (that is, a rise in cell-cell adhesion cost) can be interpreted as a drop in cadherin expression or the presence of some chemical acting towards deactivating CAM structures.

Likewise, cell-ECM adhesion can be linked to integrin expression and inhibition, or the number of binding sites on the surrounding medium, cell force to the number of FAs and their maturation, also closely related to integrin expression and signaling, or even actin, and myosin (motor proteins), expression/organization. Additionally, durotaxis parameters are also linked to the mechanosensing process, which is mediated through integrin expression, activation and signaling, and by actin expression.

4.1 Vasculogenesis

Changing the cell's properties will lead to different outcomes. Namely, in the case of random initial configuration, it might lead, or not, to the formation of vessel-like structures. In order to explore the stability of the cell culture morphology, the parameters are changed and, subsequently, checked whether or not a vascular network emerges.

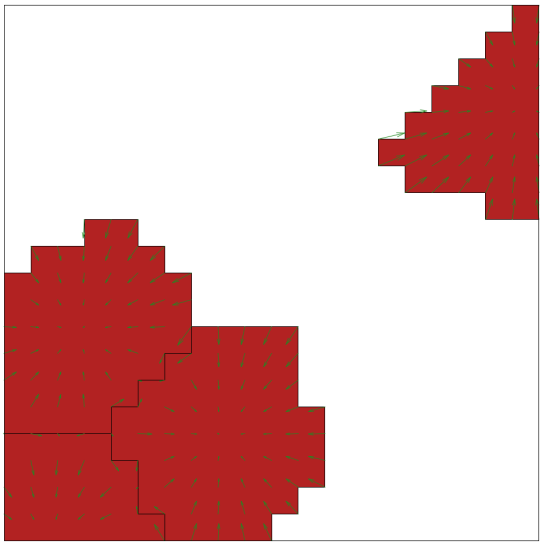

FIGURE 4.2: Zoom of the previous figure, where the forces cells apply to the ECM are represented as green vectors. For scaling purposes, each side of an element corresponds to a force magnitude of $10^{-3}N$.

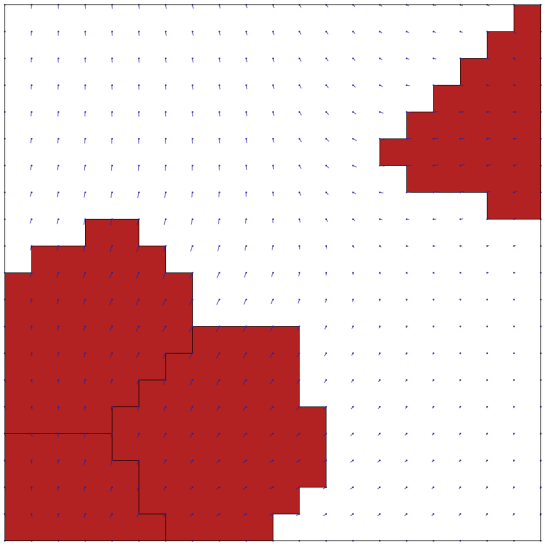

FIGURE 4.3: This figure represents each node in the undeformed configuration as a blue circle and its displacement as a blue line.

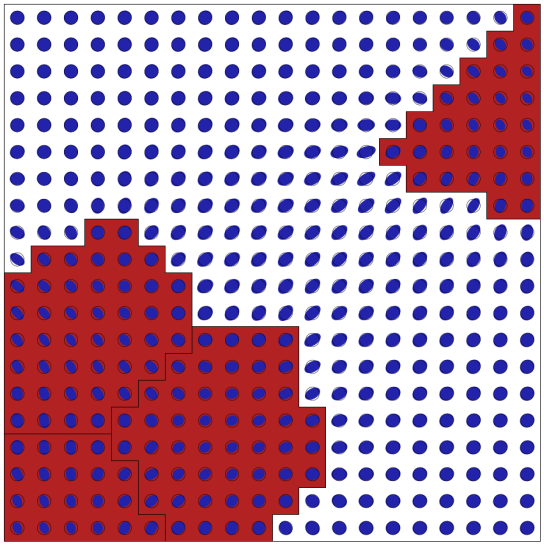

FIGURE 4.4: Representation of the strain tensor on the center of each element, by eigenvalue decomposition as in Fig. A.3. The circumference represents the null deformation tensor. Eigenvalues were amplified tenfold.

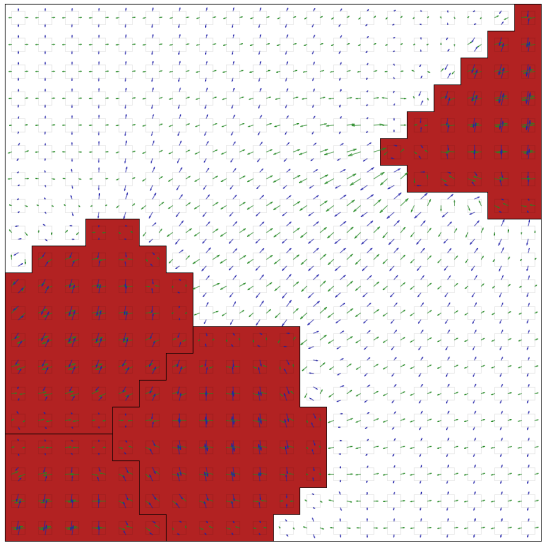

FIGURE 4.5: Representation of the stress tensor at the center of each element. The square inside each element represents an infinitely small portion at the center of the corresponding element. The green vectors represent the stress components on the sides normal to the x-axis, that is, it is the vector $(\sigma_{11}, \sigma_{12})$ for the right side of the square (and its symmetric on the opposing surface). Similarly, the blue vectors represent $(\sigma_{21}, \sigma_{22})$ on the surface above the square (and the symmetric on the bottom). For comparison purposes, the size of a side of an element corresponds to a magnitude of $10^3 N/m^2$.

For that effect, it is going to be used the CCA, previously described, namely the classification of cell structures (Fig. 4.6 and Fig. 4.7) and the quantification of network meshes (Fig. 4.6 and Fig. 4.8). The former is discussed in subsection 4.1.1 and the latter in subsection 4.1.2.

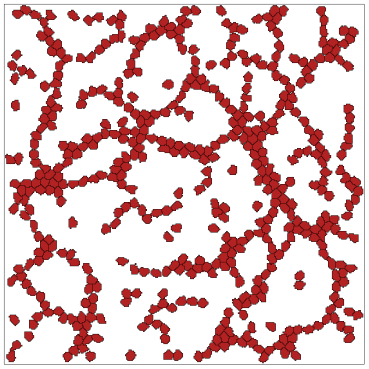

FIGURE 4.6: Result of a simulation under the same conditions of Fig. 4.1. This result illustrates an example of the classification and quantification methodology discussed in the previous chapter.

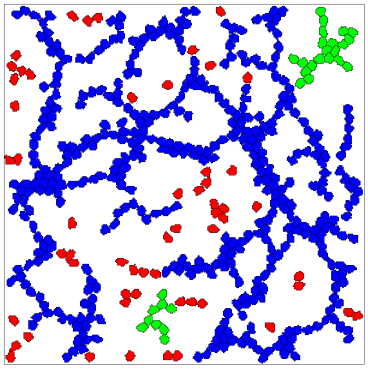

FIGURE 4.7: Classification process result for simulation result in Fig. 4.6. The colour represents the category of the cell structure a cell belongs to. Red cells are dispersed, green cells are clustered and blue cells are distributed in a meshlike fashion. In this case, two cells are considered connected if they have elements in immediate proximity, that is, no range tolerance applied.

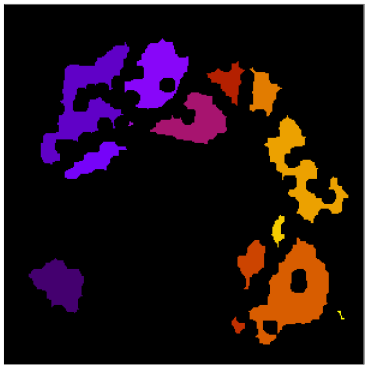

FIGURE 4.8: CCA result for figure (4.6), where each set is represented in a different colour. After that, the number of sets is counted and their size measured. If the size of a set is smaller than the target volume, then that set is eliminated in the measurements.

4.1.1 Phase Diagram of Cell Structure Classification

The parameters chosen to vary were cell-cell adhesion, due to its structural role, and the traction force parameter, in order to investigate how the structure's integrity varies according to different mechanical cues.

All results, in this section, were obtained on a 300×300 element grid with five hundred cells of a single type ($\tau = 1$) and using the default parameters aside from the two that are being varied, that is, μ_1 and J_{11}. For each set of randomly generated values of cell-cell adhesion and traction force, ten simulations were run, the results from each CCA application were obtained and their average was computed. For each aforementioned application, a total of five hundred data points were obtained.

The randomly generated values for those two parameters are on the intervals $\mu_1 \in]0, 5[$ and $J_{11} \in]1.25, 3.75[$.

The classification results of cell structures are present in Fig. 4.9, where each colour corresponds to different fraction ratios between the various categories of cells (Fig. 4.10). In this case, the categories chosen were the fractions of dispersed, clustered and meshlike cells as the fraction of red, green and blue, respectively, of each colour (using the RGB format).

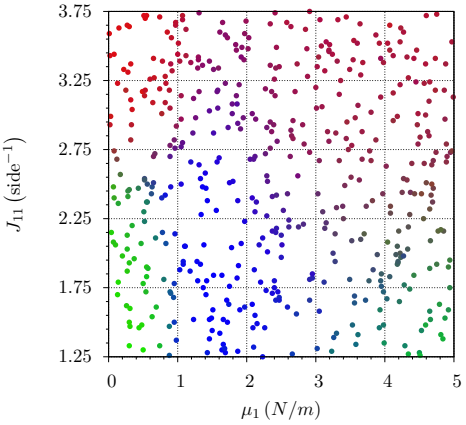

FIGURE 4.9: Classification fractions as a function of cell-cell adhesion and traction force. Each data point corresponds to an average over ten simulations, of five thousand Monte Carlo steps each, with the same parameters of μ_1 and J_{11}, but with different random number generator (RNG) seeds. There are a total of five hundred points in this graph. The colour of each point corresponds to the obtained average fractions of cell structures (dispersed cells, clusters or network-like organization), according to Fig. 4.10. From the result one can observe that in order for vasculogenesis to occur, according to the model, traction force cannot be too weak nor too strong. Furthermore, if cell-cell adhesion is too low (higher J) vessel structures form less frequently.

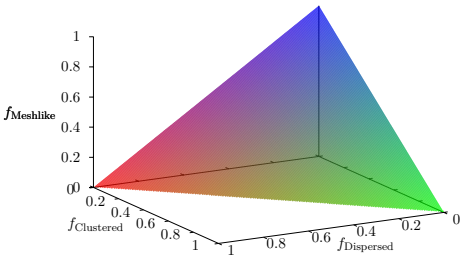

FIGURE 4.10: If cells are exclusively classified in a number (n) of categories, the point $(f_1, f_2, \ldots, f_i, \ldots f_n)$ must be restricted to the condition of $1 - \sum_{i=1}^{n} f_i = 0$. In the case of the three categories proposed, it corresponds to the points restricted on a plane defined by $1 - f_{\text{Displaced}} - f_{\text{Clustered}} - f_{\text{Meshlike}} = 0$. Furthermore, using the RGB colour code and associating each of the three colours (red, green and blue) to the three categories (displaced, clustered and meshlike, respectively), each point on the plane of possible results has a unique colour associated to it.

It can be drawn from the data the fact that the formation of vessel-like structures requires a mechanical interaction and cannot be accomplished by adhesion alone. In that particular case, cell structures are either clustered or dispersed.

With increasing traction force, a relatively sharp transition occurs for μ_1 slightly lower than 1 Nm^{-1}. That value appears to correspond to the force needed for durotaxis to take effect. The transition leads to the emergence of vessel-like structures. If the adhesion cost is low enough, almost all cells are classified as a network. However, at high values of adhesion there is a mixed region, where dispersed cells coexist with vessel-like structures.

Increasing traction force past $\mu_1 \approx 3$ Nm^{-1} leads to a smooth decrease in the fraction of meshlike cell structures and the reappearance of clusters. Meshlike structures start to decrease, because cells start to lose polarization. Polarization, according to the model, happens due to mechanical feedback which relies on the anisotropy shape of the cell in order to activate the sensing mechanism in only one direction. By increasing traction force, this disparity is overridden, depolarizing cells and the durotaxis term behaves similar to a central attractive bias towards the cell. Therefore, the fraction of clusters starts increasing with the traction force.

In order for vasculogenesis to occur consistently, according to the simulation, the parameters should be within the intervals $\mu_1 \in [1, 2.5]$ and $J_{11} \in]1.25, 2.5]$.

4.1.2 Vascular Network Mesh Structure

Next, morphology was analyzed using the CCA method on the meshes of cells structures (Fig. 4.8). From each simulation, the average number of meshes, $\langle N_{\text{mesh}} \rangle$, (Fig. 4.11) and the average size of meshes, $\langle A \rangle$, (Fig. 4.12) were obtained for the same region of parameters.

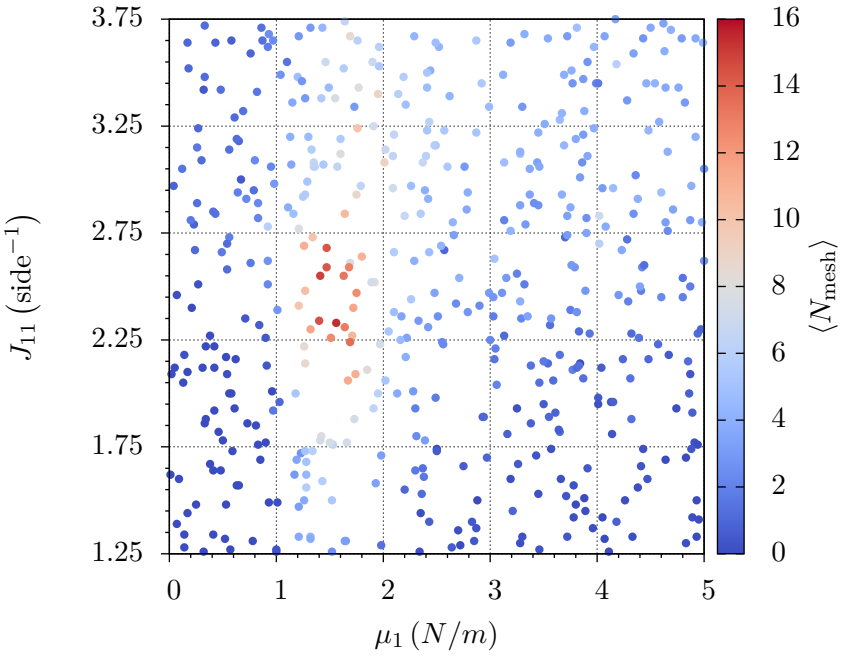

FIGURE 4.11: Average number of mesh as a function of cell-cell adhesion and traction force. Each data point corresponds to an average over ten simulations, of five thousand Monte Carlo steps each, with the same parameters of μ_1 and J_{11}, but with different RNG seeds. There are a total of five hundred points in this graph.

The average number of meshes as a function of cell-cell adhesion and traction force has a well-defined maximum at $\mu_1 = 1.50 \pm 0.20$ and $J_{11} = 2.50 \pm 0.20$. Moderate values of average mesh number can also be found for different values of J_{11}, making the regulation of traction force critical for the formation of vessel-like structures, as it was already implied in the classification result.

At large values of traction force, for higher values of adhesion cost, the problem of cell depolarization, and subsequent destruction of vascular-like structures, diminishes, leading to a higher tolerance of mesh formation, although very low in number, also hinted by the low fraction of meshlike structures in Fig. 4.9. The average mesh number reaches a plateau for high values of adhesion cost, because durotaxis is present and the gaps are closed by the CCA regardless, making adhesion value relevant only for impeding clustering, at high μ_1 values.

Regarding mesh size (Fig. 4.12), the optimal traction force occupies, roughly, the interval $\mu_1 \in]1, 2[$ and the mesh area decreases with increasing adhesion cost. Once again, the traction force needs to be tightly regulated in order to form vessel-like structures. The area decreasing with adhesion cost implies that adhesion plays a fundamental role in large scale pattern emergence, although its effect is purely local. Otherwise, if only traction force would

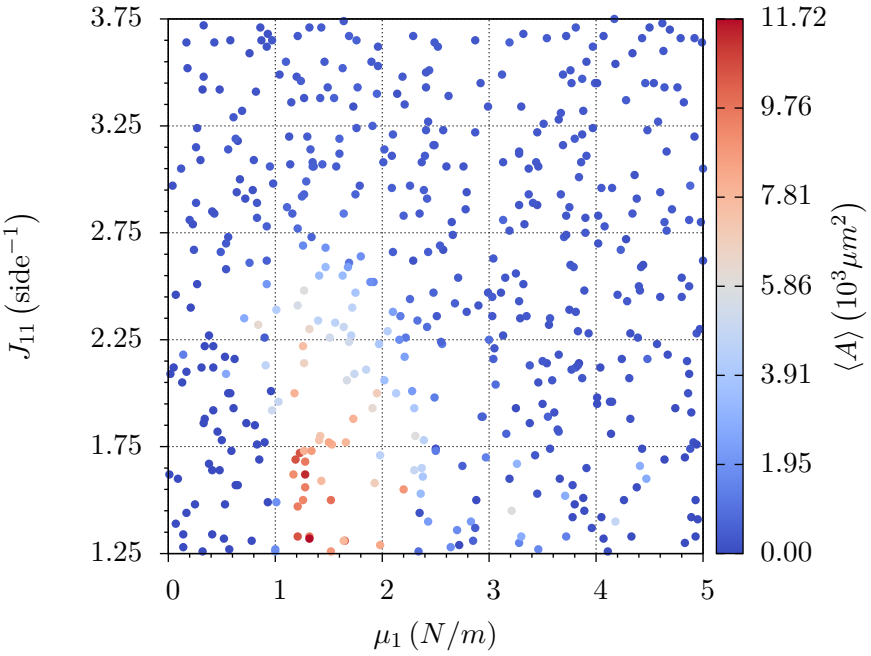

FIGURE 4.12: Average mesh area as a function of cell-cell adhesion and traction force. Each data point corresponds to an average over ten simulations, of five thousand Monte Carlo steps each, with the same parameters of μ_1 and J_{11}, but with different RNG seeds. There are a total of five hundred points in this graph.

need to be regulated, then, at high adhesion cost, the cells could maintain the vessel structures unconnected and the CCA procedure would close all remaining gaps, which would imply a smooth transition from low to high adhesion cost. As such, because there is a relatively sharp transition at $J_{11} \approx 2.75$ and it coincides with the transition from cluster to dispersed in Fig. 4.9 at $\mu_1 = 0$ (from preferably connected to preferably disconnected), adhesion is critical to large scale pattern formation.

Additionally, the cell structures at high J_{11} and regulated μ_1 (a mixed state of dispersed cells and vessel-like cell structures) are morphological significant. However, because they don't create overarching vessel networks when filling in the gaps, that is, large scale patterns are rather small in size and create very small meshes, if at all. In fact, the traction force would be the only force drawing them together. As such, there are two stable states: one where the adhesion cost inhibits the formation of larger groups of cells, with low cell concentration; and another, where cells, due to fluctuations, are able to connect along the strain on the ECM to other cells. This lowers the energy barrier, until the structure size, which has a vessel-like shape rendering the concentration of cells limited and the traction force effects unable to overlap, reaches an equilibrium point, where the rates of cell detachment and attachment are equal. The rate of attachment, aside from adhesion, traction force, strain and durotaxis, is related to the cell concentration surrounding the structure. Likewise, the detachment rate is related to the surface area of the structure. Therefore, for the same values of J_{11} and μ_1, by changing cell concentration, the model predicts that it should be possible to alter the ratio of the mix.

Furthermore, according to the result of Fig. 4.11 and Fig. 4.12, using this set up, by changing the adhesion constant, there is a trade-off between mesh size and number, allowing

for some degree of versatility on the types of systems that can be simulated using this model.

4.2 ECM With Space Dependent Rigidity

One advantage of using the FEM for dealing with structural mechanics is that it is possible to change the material properties of each individual element with relative ease. Doing this, however, would imply behaviors that do not coincide with a linear isotropic elastic material and, therefore, it is an approximation. As such, it allows for the study of two dimensional cell mobility over the ECM with position dependent rigidities. In turn, this allows to study how migration depends on stiffness variations and, for example, how cells move over two mechanically distinct materials.

Two different ECM space-dependent stiffnesses were tested. Firstly, the ECM with a constant gradient of stiffness. Secondly, the interface between two materials was tested. Every simulation in this section is done with default values, except for the Young's modulus. The size of the element grid is 300×300, the initial conditions are random (as in the previous section) and the simulation ends after five thousand Monte Carlo steps. The Young's modulus will be written in terms of the reference value $E_0 = 1 \times 10^4$ Pa.

4.2.1 Stiffness Gradient

The model was simulated for a substrate with constant stiffness rate of change along the horizontal axis. By changing the maximum and minimum values, $E_{\max}$ and $E_{\min}$, at the respective edges of the grid, the rigidity of the ECM is uniquely defined for each element. The values for both extremes were chosen such that the center of the grid would have rigidity $E = E_0$, which means that $E_{\max} = 2E_0 - E_{\min}$. Effectively, the range of values chosen for $E_{\min}$ were from E_0 to $0.75E_0$ in intervals of $0.05E_0$ (Fig. 4.13). From the way the durotaxis term is calculated, it is expected that there is a bias in cell movement towards higher stiffness. In fact, by looking at the results, the increasing accumulation of cells on the side with the highest rigidity, and lack thereof on the opposite edge, agrees with the expected behavior.

Furthermore, when increasing the stiffness gradient, larger cell structures, aside from the accumulated cells, are smaller and less prevalent, most likely because the cell adhesion keeping those structures together is counteracted, at least in part, by the cell movement bias. Furthermore, those structures have an increasingly horizontal alignment.

4.2.2 Stiffness Interface

Now, the ECM is divided into two domains with different Young's modulus. One half of the domain will have the default stiffness, $E_1 = E_0$, and the other will have a different value, E_2 (Fig. 4.14). As expected, cells near the surface of separation move from the region with lower Young's modulus to the other, whereas cells far from it evolve into patterns normally.

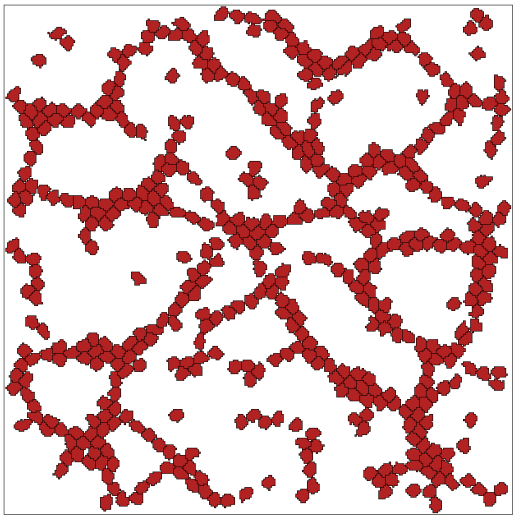

(a) $E_{\min} = 1.00E_0$; $E_{\max} = 1.00E_0$.

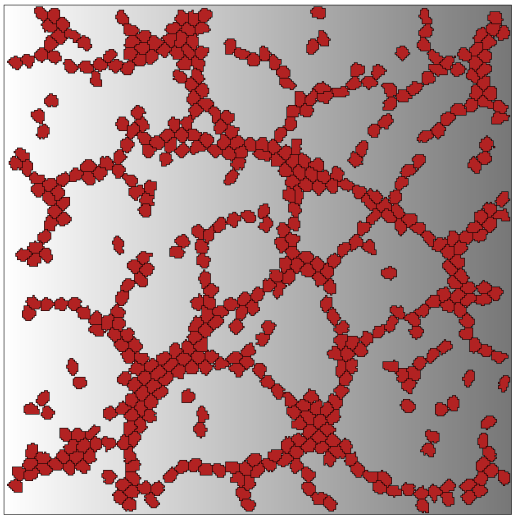

(b) $E_{\min} = 0.95E_0$; $E_{\max} = 1.05E_0$.

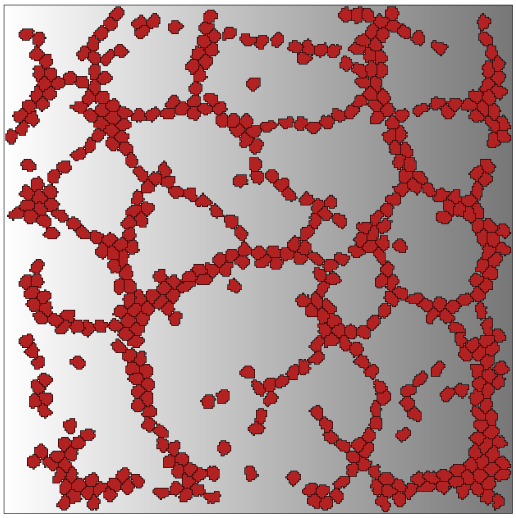

(c) $E_{\min} = 0.90E_0$; $E_{\max} = 1.10E_0$.

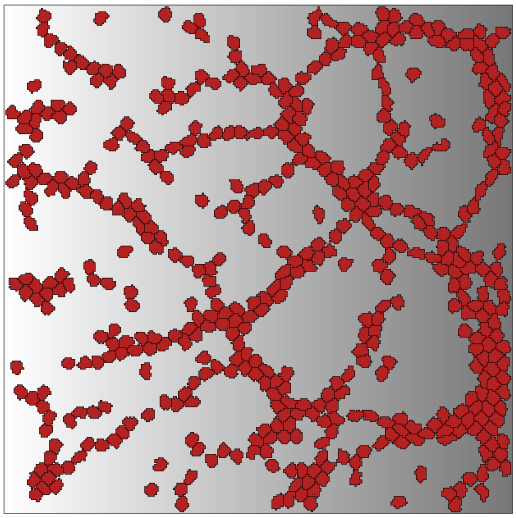

(d) $E_{\min} = 0.85E_0$; $E_{\max} = 1.15E_0$.

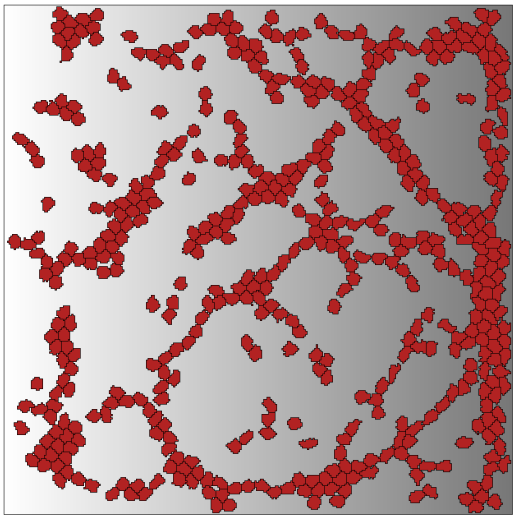

(e) $E_{\min} = 0.80E_0$; $E_{\max} = 1.20E_0$.

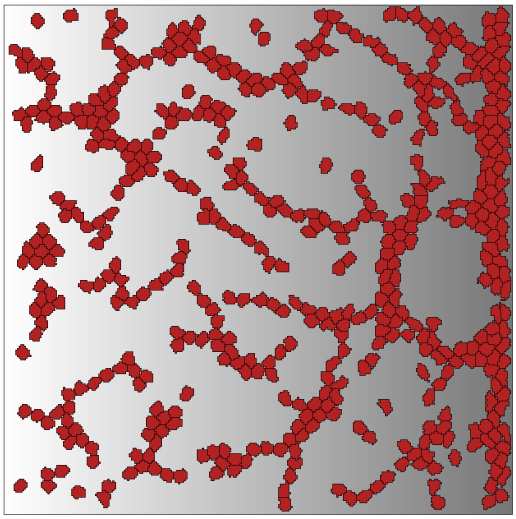

(f) $E_{\min} = 0.75E_0$; $E_{\max} = 1.25E_0$.

FIGURE 4.13: Simulation results, for a 300×300 elements grid, after five thousand Monte Carlo steps, with default parameters, except for the matrix rigidity in simulations (b)-(f), and random initial conditions. Aside from (a), the ECM has a constant stiffness gradient along the horizontal axis, fixed by the values at the vertical edges. Namely, the left side corresponds to the minimum stiffness, $E_{\min}$ (white), and the opposite side to the maximum value, $E_{\max}$ (gray).

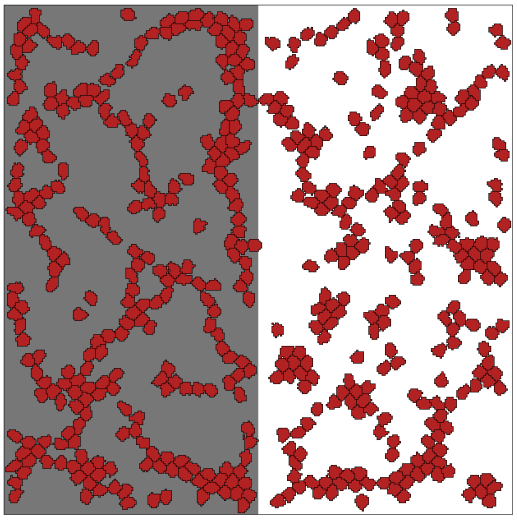

(a) $E_2 = 0.75E_0$.

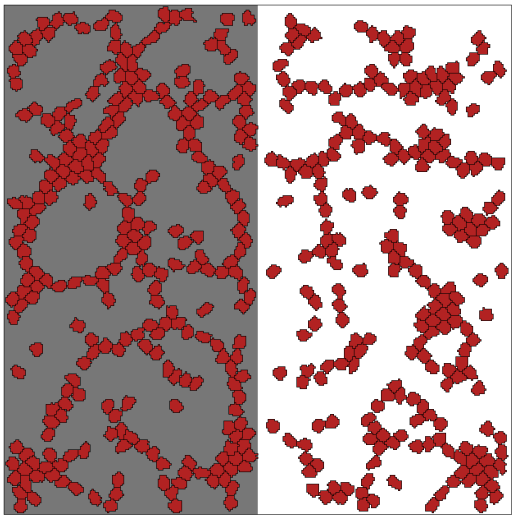

(b) $E_2 = 0.80E_0$.

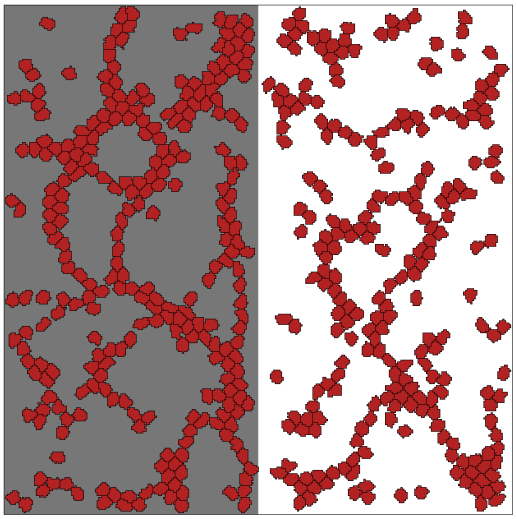

(c) $E_2 = 0.85E_0$.

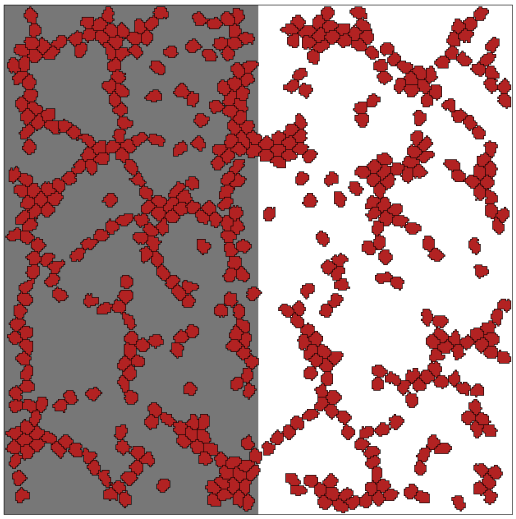

(d) $E_2 = 0.90E_0$.

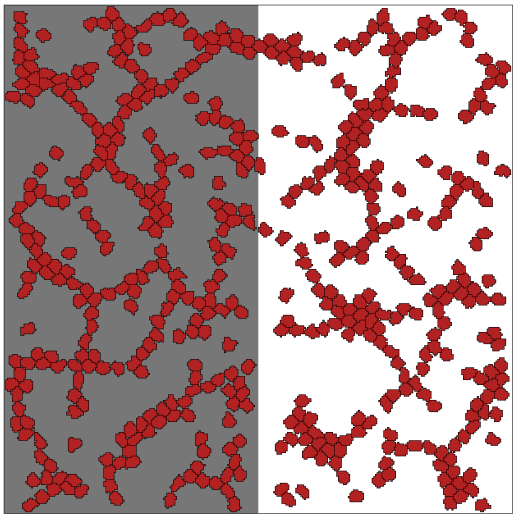

(e) $E_2 = 0.95E_0$.

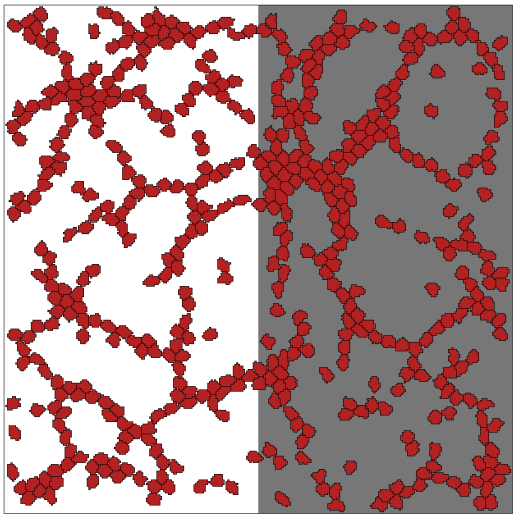

(f) $E_2 = 1.05E_0$.

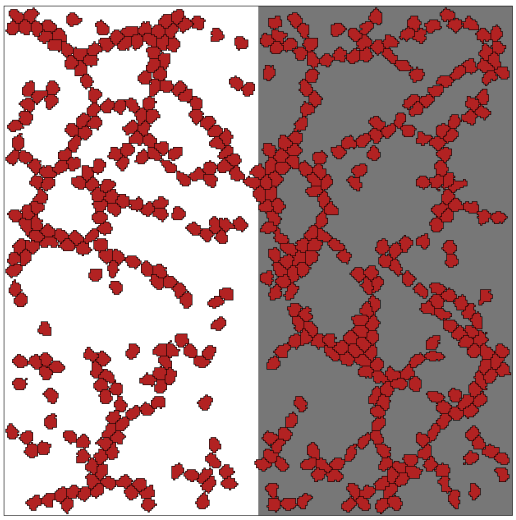

(g) $E_2 = 1.10E_0$.

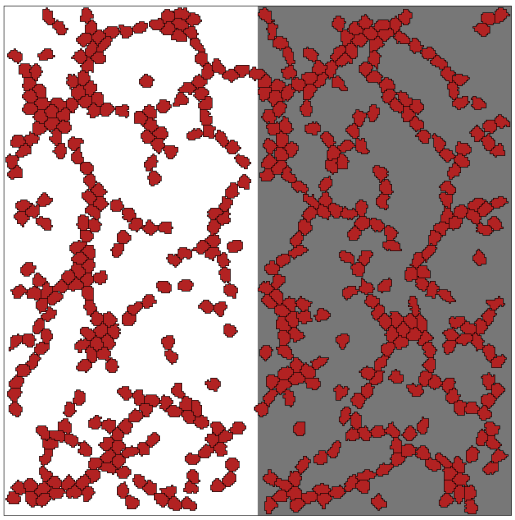

(h) $E_2 = 1.15E_0$.

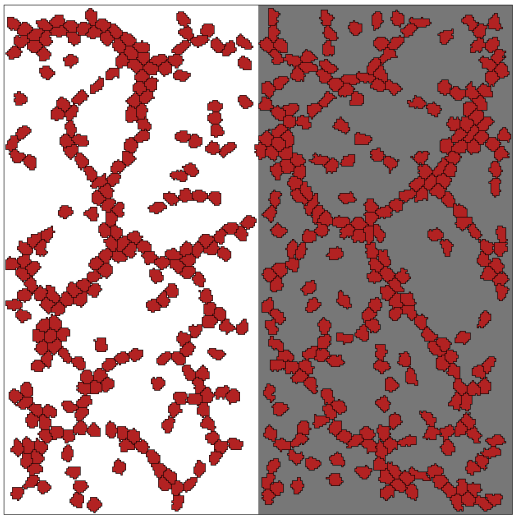

(i) $E_2 = 1.20E_0$.

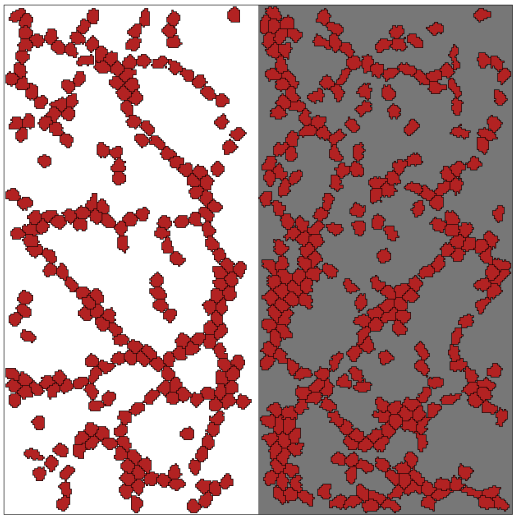

(j) $E_2 = 1.25E_0$.

FIGURE 4.14: Simulation results, for a 300×300 elements grid, after five thousand Monte Carlo steps, with default parameters, except for the matrix rigidity, and random initial conditions. The left half of the ECM has the default stiffness $E_1 = E_0$ and the stiffness of the right half varies from $E_2 = 0.75E_0$, (a), to $E_2 = 1.25E_0$, (j). In order to distinguish the domains, the ECM with larger stiffness is represented in gray.

Cells that start on or randomly come across the interface move to the region with larger rigidity. However, on both sides, cells can be guided towards the surface by strains on the ECM caused by cells on the opposite regions. Curiously, a feedback mechanism comes into play, due to the preference for higher stiffness, as cells on both regions move towards each other, they chose only one of the domains and accumulate near the surface. This accumulation enhances the strains on the ECM caused by cells on one region and increases the effect range of durotaxis on the opposite region. This leads to more cells on the lower stiffness side to wander near the surface and get captured to the other side. Therefore, there is a thin layer on each side of the surface, namely, on the stiffer side, with higher cell density and on the softer side, with lower cell population density.

Moreover, cells only continue to be near the interface with lower cell density due to adhesion

with cells on the same region, further away from the interface layer. As such, cells either dissociate and move to the other region, and deplete the layer, or remain attached and pull the neighboring cells towards the interface, when moving to the stiffer domain. This effect, provided large enough cell adhesion and stiffness difference between regions, has the potential to enable cells on the stiffer side to pull whole cell structures from the opposite region. Although this event happens more often than not in the simulated systems, its effect is quite limited for the chosen parameters, by either being too slow, or the cells breaking apart regularly, resulting in only a few cells being pulled.

4.3 Sprouting Angiogenesis

Until now, the initial cell distribution was random, however, by changing it, it is possible to study different cell systems and phenomena. For example, in order to study sprouting angiogenesis, which is the growth of new vessels from pre-existing ones, using this model two different configurations can be modeled in 2D. Either considering the plane along the vessel or the plane of its cross section.

Sprouting angiogenesis is a process that specifically requires proliferation, which is not contemplated in this model. Although it is simple to implement, it is also worth to investigate the role that mechanical cues alone play in this process.

The most straightforward initial condition for this study is a cluster of cells. This set up is similar to experimental methods used in the study of sprouting angiogenesis, namely it closely relates to a spheroid sprouting assay and, to a lesser extent, an aortic ring assay. In order to achieve this configuration, the initial conditions are four hundred cells of volume one organized in a centered square of size 20×20. Furthermore, twenty thousand Monte Carlo steps are taken in total and the default parameters will be used (Fig. 4.15a-4.15c and Fig. 4.16).

Using this set up, it is possible to ascertain that mechanical forces can drive the reorganization of the surface cells into protrusions and, by reinforcing strains on the ECM, strengthen the cell polarization causing the small protrusions to evolve into sprouts.

Effectively, in the absence of other environmental cues, this model predicts that stochasticity creates the conditions needed for initiating the feedback mechanism. Cells pulled along those preferred directions start creating narrow chains, maintained by adhesion and cell polarity. Because there is no proliferation, the sprouts will continue to grow quickly until the mechanically biased spreading of cells is counteracted by the hindrance of their migration capability caused by cell-cell adhesion. Moreover, this mechanism allows for the spontaneous bifurcation of sprouts.

Furthermore, it is also predicted that there is a minimum distance between sprouts, such that cells on the spheroid surface between them prefer to merge with the closest sprout instead.

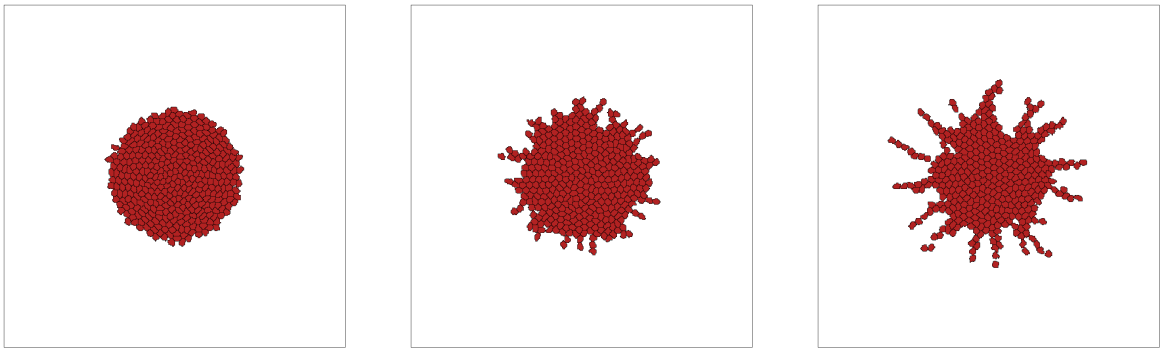

(c) 1100 Monte Carlo steps. (b) 4000 Monte Carlo steps. (c) 16400 Monte Carlo steps.

FIGURE 4.15: Simulation results, after different amounts of Monte Carlo steps, for a 400 × 400 element grid, containing four hundred cells initially placed at the center of the grid.

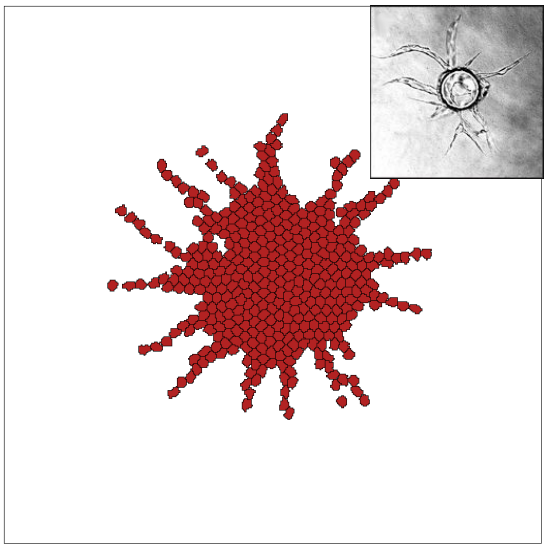

FIGURE 4.16: Simulation result for a 400×400 element grid, containing four hundred cells initially placed at the center of the grid, after 2×10^4 Monte Carlo steps. The feedback mechanism studied accounts for the polarization of cells on the surface, that leads to the formation of sprouts. Furthermore, the traction force exerted in the ECM by the cells of the sprout reinforce strains along each path, becoming well defined sprouts. On the top right corner, an experimental control result, adapted from [46], is presented for comparison purposes.

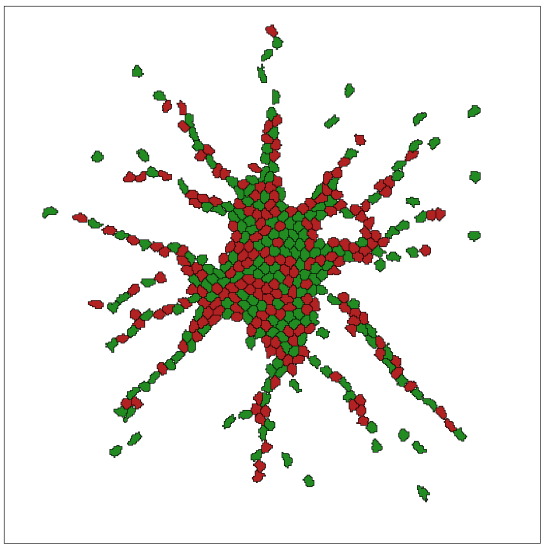

FIGURE 4.17: Simulation result for a 400×400 element grid, containing four hundred cells, of two different types, initially placed at the center of the grid after 2×10^4 Monte Carlo steps. On initialization, each cell was assigned a randomly generated type from an uniform distribution. The red cells have the default parameters and the green cells have a traction force constant of $\mu_2 = 2\ \mathrm{Nm}^{-1}$.

In this simulation, sprouts are shorter than in the experimental spheroid. This effect is, at least in part, related to the aforementioned lack of proliferation. Other possible explanation for this difference is that the default parameters may not accurately describe the same endothelial cells. Nevertheless, including proliferation should help establish the reason(s) this result does not entirely agree with the experiment.

Next, another type of cell was used with contact energies $J_{22} = J_{12} = J_{11} = 1.25\ \mathrm{side}^{-1}$ and different traction force constant $\mu_2 = 2\ \mathrm{Nm}^{-1} = 2\mu_1$. Under the same conditions of the previous simulation, except for the new type ($\tau = 2$), each cell will be one of the two types

with equal probability (Fig. 4.17).

By adding the new type of cells, the resulting spheroid undergoes morphological changes relative to the previous one. Namely, sprouts grow slightly thicker and substantially longer. Moreover, the number of bifurcations increases, eventually merging a sprout tip to another, creating a closed path; this phenomenon is called anastomosis.

However, cells of the new type dissociate from the spheroid more often than the default type. This fact, in addition to the existence of larger sprouts, implies that the traction force improves the migration capabilities of the cell. This implication is valid for values of matrix stiffness that do not saturate the sigmoid portion of the durotaxis term of the CPM, that is, values of matrix stiffness that allow strain stiffening to change pseudopodium grip appreciably.

Furthermore, under these conditions, when at the tip of a sprout, cells with larger traction force play a role akin to that of tip cells. In sprouting angiogenesis, tip cells are specialized endothelial cells in front of the sprout, as the name implies, responsible for sensing environmental cues and guiding sprout growth accordingly. Effectively, the activation of endothelial cells into the tip cell phenotype has a pivotal role in the formation of large sprouts. This suggests that tip cells exert stronger forces on the ECM than other endothelial cells and, as a result, contribute to the communication of their polarization with the cells preceding it.

4.4 Avascular Tumor Metastasis

Another system in which mechanical cues and, consequently, cell migration, take center stage is the invasion of tissues by metastatic tumor cells, that is, cells with a malignant phenotype. In contrast with normal tumor cells, metastatic cells have increased migration capabilities, allowing them to escape the tumor and form metastases (new masses of cancerous cells), possibly far away from the initial tumor if they manage to invade blood vessels and enter the blood flow.

Normal tumor cells are typically aggregated into clusters, possessing relatively high cell-cell adhesion, in comparison to endothelial cells (corresponding, to some extent, to the default value). On the other hand, metastatic cells have higher traction force [47], lower cell-cell adhesion, due to the loss of cadherin expression/activity [48] and higher integrin expression, which leads to higher cell-matrix adhesion [49].

Therefore, in order to simulate this system, the parameters chosen must reflect the properties of the designated cell types. Let $\tau = 1$ represent normal tumor cells and $\tau = 2$ metastatic cells. The values used for traction force were $\mu_1 = 0.5$ Nm^{-1} and $\mu_2 = 3\mu_1 = 1.5$ Nm^{-1}. For cell-cell adhesion, the values used were $J_{11} = 2.25$ side^{-1}, $J_{12} = 2.75$ side^{-1} and $J_{22} = 3.25$ side^{-1}. For cell-matrix adhesion of metastatic cells, the value used was $J_{02} = 1.00$ side^{-1}. For the remaining parameters the default values were used.

Each simulation was done on a 400×400 elements grid, with four hundred cells, using the initial conditions from the spheroid simulations, and stopped after 2×10^4 Monte Carlo steps. Effectively, three set ups were simulated. Firstly, using only normal tumor cells (Fig. 4.18), secondly, using only metastatic cells (Fig. 4.19) and, finally, a co-culture of both cells types (Fig. 4.20) (each cell was randomly assigned a type with equal probabilities).

The tumor made up entirely from cells of type $\tau = 1$ (Fig. 4.18) is non-invasive, also referred to as benign. Although the traction force is weaker, the surface still shows remnants of mechanically-induced protrusions. As such, the surface is slightly uneven. This roughness on the surface is often indicative of how invasive the tumor cells' phenotype is.

When all cells are metastatic (Fig. 4.19), the tumor is unable to hold together, due to a lack of adhesion. Additionally, because cells have high traction force, they are able to migrate relatively far away from the center of the grid, spreading over the whole domain.

Lastly, a culture of mixed type tumor cells was simulated (Fig. 4.20). In this case, metastatic cells, after initializing the system, get constrained by the normal tumor cells and, afterwards, try to escape to the surface. This organization is unexpected, since cell-matrix adhesion is stronger for metastatic cells and adhesion between metastatic cells is very weak. It is, perhaps, consequence of the mechanical cues and it remains confined, for an extended period of time, due to the strong cell-cell adhesion of normal tumor cells. Unfortunately, it does not appear to correspond to what is to be expected. Tweaking the initial conditions, for instance, not clustering cells too much, may be able to change this tendency. Nevertheless, metastatic cells that manage to get to the surface are able to escape the tumor, migrating outwards, and the traction forces those cells exert on the ECM cause the normal tumor cells near the surface to sense the strain stiffening of the substrate and attempt to migrate collectively. However, because they are bound to the other normal tumor cells, they are unable to dissociate from the tumor, forming protrusions on the surface. Due to the two dimensional constraint, the tumor appears to break, when metastatic cells are able to leave the tumor. In a three dimensional set up, metastatic cells would be able to get to the surface without the need to dissociate normal tumor cells.

Therefore, even if the system is not completely realistic, consequences of the mechanical feedback effect, predicted by the model, can still be observed. Namely, the development of protrusions of normal tumor cells, induced by metastatic tumor cells in a three dimensional set up can be verified experimentally [50]. In order to try to simulate 3D migration, however, models for cell locomotion and traction force need to be redesigned, and new ECM phenomena, such as degradation and remodeling of the ECM, come into play and need to be modeled.

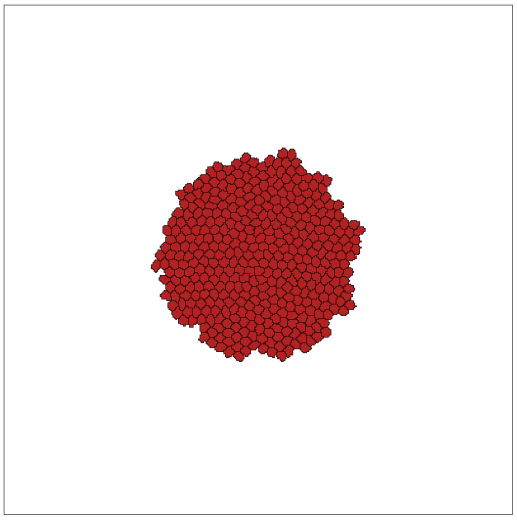

FIGURE 4.18: Simulation result after 2×10^4 Monte Carlo steps of four hundred non-malignant tumor cells ($\tau = 1$), on a 400×400 element grid, with traction force $\mu_1 = 0.5$ Nm^{-1} and cell-cell adhesion $J_{11} = 2.25$ side^{-1}. The cells organize into a cluster with very small protrusions, caused by the mechanical retroactive mechanism.

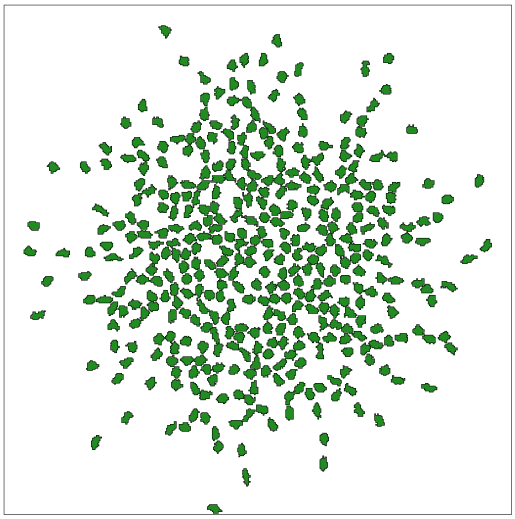

FIGURE 4.19: Simulation result after 2×10^4 Monte Carlo steps of four hundred malignant tumor cells ($\tau = 2$), on a 400×400 element grid, with traction force $\mu_2 = 1.5$ Nm^{-1}, cell-cell adhesion $J_{22} = 3.25$ side^{-1} and cell-matrix adhesion cost $J_{02} = 1.00$ side^{-1}. Because these cells prefer to be in contact with the substrate, they migrate outwards from the starting position, spreading over the ECM.

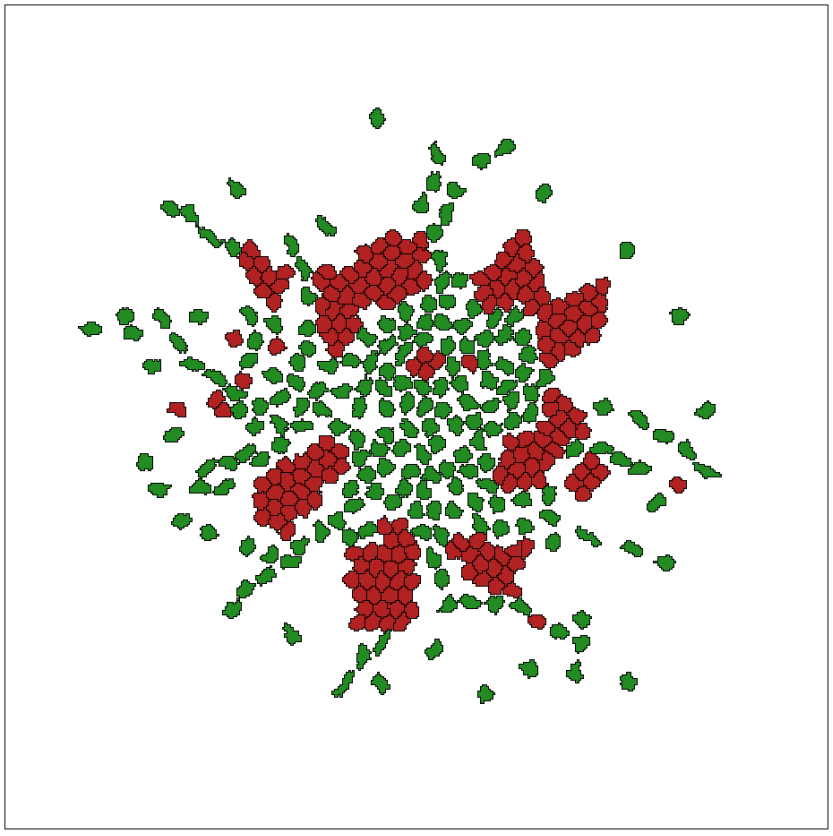

FIGURE 4.20: Simulation result after 2×10^4 Monte Carlo steps of four hundred tumor cells either non-malignant ($\tau = 1$), or malignant ($\tau = 2$), with equal probability, on a 400×400 element grid. The cell adhesion parameters used were $J_{11} = 2.25$ side^{-1}, $J_{12} = 2.75$ side^{-1}, $J_{22} = 3.25$ side^{-1} and $J_{02} = 1.00$ side^{-1}. The traction force values used were $\mu_1 = 0.5$ Nm^{-1} and $\mu_2 = 1.5$ Nm^{-1}. Normal tumor cells and restrained malignant cells form the bulk of the tumor, while malignant cells that manage to reach the surface escape it, because of their low cell-cell adhesion, and, because they have larger traction force, leading to greater strains, enable protrusions to develop and extend farther.

Chapter 5

Conclusions and Future Work

5.1 Conclusions and Outlook

In recent years, the study of the physical mechanisms in cell motion has become increasingly prevalent in the fields of cell biology and biochemistry. Traction force generation, durotaxis and mechanosensing are examples of mechanically intensive phenomena regulated by biochemical cell signaling pathways, and vice-versa. These processes have remarkably surprising consequences. However, the complexity and magnitude of these effects presents a great challenge in their understanding.

Cell pattern formation is a consequence of local interactions of individual cells. In fact, cell movement emerges from the communication between cells, which can be of various natures, for instance, contact (adhesion), chemical and mechanical. Therefore, the study of emerging patterns may provide insight into the mechanisms that regulate cell migration, namely into the mechanical processes underlying cell movement.

In fact, a model of how a process works is validated by the empirical evidence for its predictions. However, because biological systems have highly interacting components, predicting can become rather difficult. Hence, the use of computer models allows forming predictions and helps designing experimental set ups needed to disprove the assumptions made when conceptualizing the model.

The model for cell migration, proposed by Oers and Rens, is an hybrid model that consists of a FEM for calculating the deformation of the ECM coupled with a CPM for representing cells and adhesion mechanics. The interface between both is made by a predictive model of cell traction force, proposed by Lemmon and Romer, and a phenomenological model of mechanosensing. In the present work, an image analysis method, CCA, was adapted in order to extract quantitative information from the results of the computational model.

First, the model was applied to vasculogenesis, that is, vascular-like pattern formation. The quantitative methods were used in order to explore the effect that traction force and cell-cell adhesion have in the formation of the patterns. Effectively, tested cell cultures were labeled according to the fractions of cells classified into one of three categories, namely, dispersed cells, clusters and meshlike structures, according to the average number and size of the vessel-like

structure's meshes. In order for meshlike structures to emerge, according to the model, adhesion alone is not enough and mechanical cues between the cells are required. Traction force needs to be tightly regulated and cell-cell adhesion cost must be below a certain threshold, in order for large scale pattern formation to emerge. Furthermore, this model predicts that increasing the cost of cell-cell adhesion leads to an increase in number of meshes, although, in turn, it also relates to a decrease in their size. Moreover, increasing the traction force results in the formation of clusters. Cell density also plays a role in the final morphology of cell structures.

Afterwards, still on the context of vasculogenesis, the model was tested on substrates with different stiffness distributions. The first set of distributions had a constant stiffness gradient and it was observed the expected durotaxis bias. In the second group, the region near the interface displayed a region depleted of cells on the side with the lower Young's modulus and an accumulation of cells on the opposite side. This accumulation reinforces traction force near the interface and increases the effect range of durotaxis. Additionally, if adhesion is strong enough, several cells may be pulled towards the side with higher Young's Modulus by other cells.

Next, a system similar to a sprouting spheroid assay was tested. The cells on the surface of the spheroid spontaneously polarize and start creating sprouts which, after some time, stabilize in length. The result did not fully agree with the experimental sprout length, possibly because proliferation was not contemplated in the model. After that, half of the cells with the default traction force were replaced by cells with twice the value of traction force, which resulted in longer sprouts, suggesting that tip cells have increased traction force magnitude. Moreover, the number of bifurcations increased and anastomosis was observed.

Finally, a system of an avascular tumor was tested using this model. Two types of cells were simulated. Normal tumor cells and metastatic tumor cells. After adjusting the model's parameters accordingly, three simulations were executed: only normal tumor cells, only metastatic tumor cells and an even mix of both. When all cells are normal tumor cells, mechanical cues are sufficient to cause the surface of the tumor to be uneven. The metastatic type has increased migration capabilities and the tumor is not able to hold together. In the mixed tumor, when metastatic cells escape, mechanical signals are enough to promote the cells on the surface to start forming larger protrusions.

5.2 Future Work

Applying this model to more systems will help to learn about the role of cell-cell adhesion, traction force and mechanical properties of the ECM on different biological systems. For example, simulating systems embedded in a cell tissue, by including regular tissue cells. However, the model used can be improved in a number of ways. As already mentioned, proliferation could be implemented, which could be a function of the concentration of diffusible nutrients in the ECM. Diffusion of chemical signals and integrating chemotaxis could be another route and even more so when coupling it with diffusion of nutrients and proliferation, in order to study

tumor induced sprouting angiogenesis. Diffusion of chemical signals could also be improved by considering bound and unbound molecules.

Another possible improvement is to model ECM remodeling, the process by which cells affect the composition of the substrate, promoting homeostasis, and the consequences of it being defective. ECM degradation (for example by matrix metalloproteinase) could also be studied in a two-dimensional fashion, by assuming a layer of ECM surrounding the cells. Moreover, by combining remodeling and degradation, this model could help designing a three-dimensional cell migration model.

More models for durotaxis, mechanosensing and traction force generation could be implemented and tested. Additionally, the CPM could be turned into an agent-based model and other intracellular mechanisms could be implemented; for example, a region could be the lamellipodium, defined by cell polarity, and mechanosensing could be restricted to that area, or some regions could have the CAMs deactivated because of an inhibitor, or cells changing phenotypes according to internal mechanisms.

Aside from more biological approaches to the extension of the model, a more detailed description of deformations, that take into account strain stiffening, could be implemented, in order to validate the approximation being done.

Regarding experimentation, vasculogenesis in vitro, under different conditions, could validate this model's predictions for morphology. However, this could prove difficult to analyze, considering that cell-matrix adhesion, integrin expression, focal adhesion maturation and traction force are intimately related. Altering ECM stiffness and cell-cell adhesion could prove to be a less contrived procedure. The trade-off between size and number of meshes of a vascular network could, in principle, be validated and experiments with different types of substrate could provide insight into mechanical cues.

Nevertheless, this model can be used to interpret data obtained from cell migration experiments, and help improve its understanding.

In conclusion, the analysis of this model's implications serves as a stepping stone for understanding its usefulness and limitations. By doing such, it is possible to check how the models of mechanical cues are lacking and how to improve them. Regardless of what small details the model fails to describe, this analysis shows how cell-cell adhesion, substrate stiffness and cell force traction affects vasculogenesis. The model brings to light the consequences of adhesion and traction not being properly tuned and helps to traceback the cause for erroneous pattern formation. It will also permit to model other biological systems where mechanical signals play an important role in defining their dynamics.

Appendix A

Geometrical Interpretation of the Displacement Gradient

As already mentioned, the displacement gradient can be decomposed into its symmetric and antisymmetric parts. Using tensor notation, the displacement gradient becomes

$$\partial_j u_i = \frac{1}{2}\left(\partial_j u_i + \partial_i u_j\right) + \frac{1}{2}\left(\partial_j u_i - \partial_i u_j\right) = \varepsilon_{ij} + \omega_{ij}, \tag{A.1}$$

where u_i refers to $u_i\left(\mathbf{x}\right)$, and $\partial_j u_i$ represents $\frac{\partial u_i}{\partial x_j}$.

First, let's consider the antisymmetric tensor ω_{ij}:

$$\omega_{ij} = \frac{1}{2}\left(\partial_j u_i - \partial_i u_j\right). \tag{A.2}$$

In the 2D case and in order for each element of ε_{ij} to be zero, $\partial_1 u_1 = \partial_2 u_2 = 0$ and $\partial_2 u_1 = -\partial_1 u_2 = \theta$. In that particular case and in the absence of parallel translation, a point δx_i away from x_i will be transported to

$$\delta x_i \to \delta x_i + \partial_j u_i \delta x_i = \delta x_i + \omega_{ij}\delta x_j = \left(\delta_{ij} + \omega_{ij}\right)\delta x_j = \delta x_i',$$

where δ_{ij} is the Kronecker delta is

$$\delta_{ij} = \begin{cases} 0 & \text{if } i \neq j, \\ 1 & \text{if } i = j. \end{cases} \tag{A.3}$$

Therefore, this can be written as a linear transformation such that, in matrix form:

$$\mathbb{A}\delta\mathbf{x} = \delta\mathbf{x}', \qquad \text{where } \mathbb{A} = \begin{pmatrix} 1 & -\theta \\ \theta & 1 \end{pmatrix}.$$

Furthermore, given that a rotation of a rigid body by a small angle θ is given by

$$\mathbb{R} = \begin{pmatrix} \cos\theta & -\sin\theta \\ \sin\theta & \cos\theta \end{pmatrix} \approx \begin{pmatrix} 1 & -\theta \\ \theta & 1 \end{pmatrix}.$$

It becomes clear that the antisymmetric tensor ω_{ij} is the portion of displacement due to rotation only.

On the other hand, the tensor ε_{ij}, also called the infinitesimal strain tensor, is

$$\varepsilon_{ij} = \frac{1}{2}\left(\partial_j u_i + \partial_i u_j\right). \tag{A.4}$$

The diagonal elements of ε_{ij} are called the normal strains. In the case of a diagonal strain tensor, the point δx_i away from x_i, without translation and rotation, is mapped to

$$\delta x_i \to \delta x_i + \varepsilon_{ij}\delta x_j = \left(\delta_{ij} + \varepsilon_{ij}\right)\delta x_j = \delta x_i'.$$

Similarly, the transformation matrix associated to this mapping (in 2D) is

$$\mathbb{A} = \begin{pmatrix} 1+\varepsilon_{11} & 0 \\ 0 & 1+\varepsilon_{22} \end{pmatrix}.$$

For example, a bar in 1D with length L_0, after this transformation, it would have length

$$L = \left(1+\varepsilon_{11}\right)L_0 \Leftrightarrow \varepsilon_{11} = \frac{L-L_0}{L_0} = \frac{\delta L}{L_0}.$$

Therefore, normal strains defined in this manner refer to the relative expansion and contraction of the element in the direction of the base vectors. In fact, the trace of ε_{ij} is directly related to change in volume,

$$\mathrm{tr}\left(\varepsilon_{ij}\right) = \frac{\delta V}{V_0} = \varepsilon_{11} + \varepsilon_{22} + \varepsilon_{33}. \tag{A.5}$$

Similarly, the off-diagonal elements of ε_{ij} map δx_i to $\delta x_i'$ through

$$\mathbb{A} = \begin{pmatrix} 1 & \varepsilon_{12} \\ \varepsilon_{12} & 1 \end{pmatrix}.$$

Applying this transformation to a square of side L_0 (Fig. A.1), we can relate the angle θ to the strain ε_{12}. For small angles,

$$\theta \approx \tan\theta = \frac{\varepsilon_{12}L_0}{L_0} = \varepsilon_{12}.$$

As a result, ε_{12} represents the angle between a material line originally along the direction of a basis vector and the same line after the deformation due to shear. Therefore, ε_{12} is called shear strain[1].

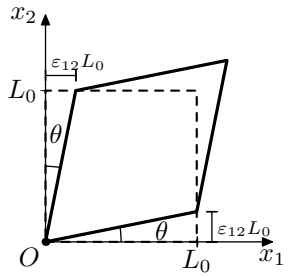

FIGURE A.1: Diagram representing a pure shear deformation.

Lastly, for representation purposes, it is useful to consider the eigenvalue decomposition of the strain tensor. In index notation, the eigenvalue problem is

$$\varepsilon_{ij}n_j = \lambda n_j, \tag{A.6}$$

[1]Not to be conflated with engineering shear strain, which is defined as the change in angle between two previously orthogonal lines: $\gamma_{12} = 2\varepsilon_{12}$.

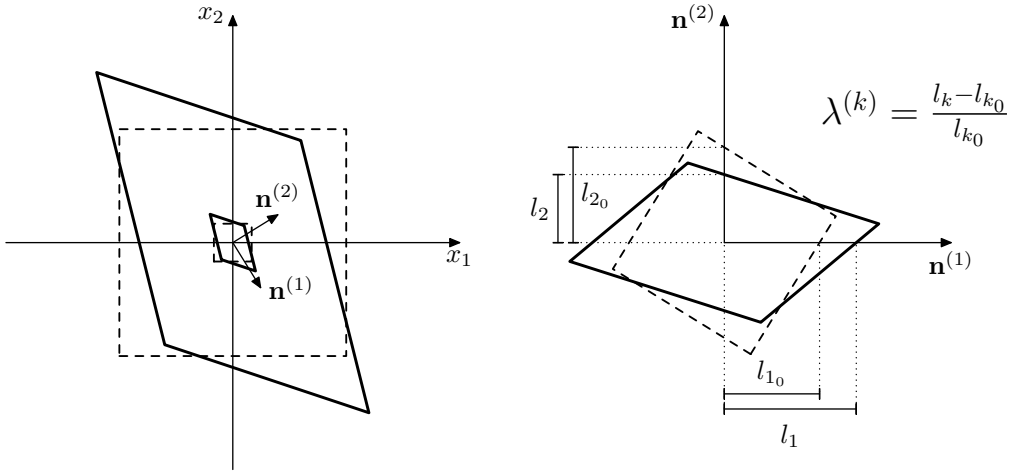

FIGURE A.2: Diagram representing a square after some deformation and the corresponding eigenvectors $\mathbf{n}^{(1)}$ and $\mathbf{n}^{(2)}$. These vectors represent the principal axis of strain on the right. It can also be observed the effect of the principal strains $\lambda^{(1)}$ and $\lambda^{(2)}$.

which the solution is obtained by writing

$$(\varepsilon_{ij} - \lambda\delta_{ij})\, n_j = 0. \tag{A.7}$$

For a non trivial solution to exist, the determinant must vanish, therefore

$$|\varepsilon_{ij} - \lambda\delta_{ij}| = 0. \tag{A.8}$$

This gives a set of eigenvalues $\lambda^{(k)}$, one for each dimension. Substituting each eigenvalue in equation (A.7) yields the corresponding normalized eigenvectors $n_j^{(k)}$.

After finding the eigenvalues and eigenvectors, we can decompose the strain tensor with the symmetric eigenvalue decomposition

$$\varepsilon_{ij} = U_{i\alpha}\Lambda_{\alpha\beta}U_{j\beta}, \tag{A.9}$$

where

$$\Lambda_{\alpha\beta} = \lambda^{(\alpha)}\delta_{\alpha\beta} \tag{A.10}$$

is a diagonal matrix (no implicit sum in (A.10)), and

$$U_{i\alpha} = n_j^{(k)}\delta_{ij}\delta_{\alpha k} \tag{A.11}$$

is orthogonal because ε_{ij} is symmetric.

This decomposition implies that any deformation can be decomposed in a rotation and/or reflection (unitary transformation), followed by normal strains corresponding to the eigenvalues (principal strains) and ending with the inverse unitary transformation (Fig. A.2).

This way, it is possible to uniquely represent the strain tensor on a 2D surface by plotting an

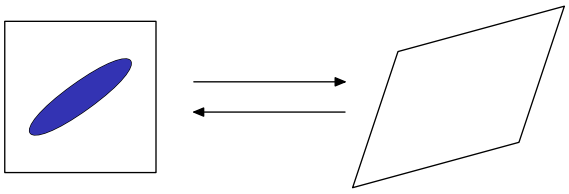

FIGURE A.3: Representation of the strain tensor through eigenvalue decomposition. This is the visualization method that is going to be used when mapping strains on a grid.

ellipse whose axis are in the direction of $\mathbf{n}^{(k)}$ and radii are $1+\lambda^{(k)}$, in each of those directions, respectively (Fig. A.3).

Appendix B

Equilibrium Consequences for the Stress Tensor

Under the assumption that the body in question is at rest, the sum of all forces acting on the body must vanish. Consider a body occupying a volume V and with a surface S under both volume and surface forces b_i and T_i, per unit volume and area, respectively. The equilibrium equation would be

$$\oint_S T_i^{(\mathbf{n})}\, dS + \int_V b_i\, dV = 0, \tag{B.1}$$

and, using the definition of the stress tensor (2.5), becomes

$$\oint_S \sigma_{ji} n_j\, dS + \int_V b_i\, dV = 0, \tag{B.2}$$

which, using the Gauss's divergence theorem, gives

$$\int_V \left(\partial_j \sigma_{ji} + b_i\right)\, dV = 0, \tag{B.3}$$

for any arbitrary V. Therefore the integrand must be null, giving the equilibrium equation

$$\partial_j \sigma_{ji} + b_i = 0, \tag{B.4}$$

in regards to linear momentum.

However, for a body to be in a state of equilibrium, aside from force balance, the sum of the moments of force ($\mathbf{M} = \mathbf{x} \times \mathbf{F}$) must also be null. Using the tensor notation, the moment of force can be written as

$$\mathbf{M} = \mathbf{x} \times \mathbf{F} = \varepsilon_{ijk} x_i F_j, \tag{B.5}$$

where ε_{ijk} is known as the Levi-Civita symbol in three dimensions, given by

$$\varepsilon_{ijk} = \begin{cases} +1 & \text{if} \quad (i,j,k) = (1,2,3),\ (2,3,1) \text{ or } (3,1,2), \\ 0 & \text{if} \quad i = j,\ j = k \text{ or } k = i, \\ -1 & \text{if} \quad (i,j,k) = (1,3,2),\ (1,2,3) \text{ or } (2,1,3). \end{cases} \tag{B.6}$$

That is, for the same body,

$$\oint_S \varepsilon_{ijk} x_i T_j^{(\mathbf{n})}\, dS + \int_V \varepsilon_{ijk} x_i b_j\, dV = 0. \tag{B.7}$$

Using the stress tensor definition (2.5), the equation becomes

$$\oint_S \varepsilon_{ijk} x_i \sigma_{\alpha j} n_\alpha \, dS + \int_V \varepsilon_{ijk} x_i b_j \, dV = 0, \tag{B.8}$$

that, by applying the Gauss's theorem, gives

$$\int_V \left[\partial_\alpha \left(\varepsilon_{ijk} x_i \sigma_{\alpha j}\right) + \varepsilon_{ijk} x_i b_j\right] \, dV = 0, \tag{B.9}$$

in which, by the same argument as before, the integrand must vanish, giving

$$\varepsilon_{ijk} \left[\delta_{i\alpha} \sigma_{\alpha j} + x_i \left(\partial_\alpha \sigma_{\alpha j} + b_j\right)\right] = 0. \tag{B.10}$$

The second term contains the balance equation (B.4), therefore

$$\varepsilon_{ijk} \sigma_{ij} = 0, \tag{B.11}$$

Which, expanding, gives the three equations:

$$\sigma_{12} - \sigma_{21} = 0; \tag{B.12}$$

$$\sigma_{23} - \sigma_{32} = 0; \tag{B.13}$$

$$\sigma_{31} - \sigma_{13} = 0. \tag{B.14}$$

Or, in general,

$$\sigma_{ij} = \sigma_{ji}, \tag{B.15}$$

which means that, in order for the body to be in equilibrium, the stress tensor must be symmetric. Therefore, there are only 6 independent components (in 3D).

An object under stress responds by exhibiting displacements. The total work done by the surface and volume forces, T_i and b_i, with a displacement field u_i, on a body of volume V with surface S, is given by

$$\oint_S u_i T_i^{(\mathbf{n})} \, dS + \int_V u_i b_i \, dV.$$

Using the definition of the stress tensor (2.5) and Gauss's theorem, yields

$$\oint_S u_i \sigma_{ji} n_j \, dS + \int_V u_i b_i \, dV = \int_V \left[\partial_j \left(u_i \sigma_{ji}\right) + u_i b_i\right] \, dV,$$

using the equilibrium equation (B.4), gives

$$\int_V \left[\sigma_{ji} \partial_j u_i + u_i \partial_j \sigma_{ji} - u_i \partial_j \sigma_{ji}\right] \, dV = \int_V \sigma_{ji} \partial_j u_i \, dV,$$

which, by equation (2.2), becomes

$$\int_V \left[\sigma_{ji} \varepsilon_{ij} + \sigma_{ji} \omega_{ij}\right] \, dV.$$

Noting that the Frobenius product ($a_{ij}b_{ij}$) of a symmetric by an antisymmetric tensor is null, we arrive at the following equation

$$\oint_S u_i T_i^{(\mathbf{n})}\, dS + \int_V u_i b_i\, dV = \int_V \varepsilon_{ij}\sigma_{ij}\, dV, \tag{B.16}$$

that relates external forces with internal strains and stresses.

Appendix C

Constitutive Equation

As implied in equation (2.9), a real variation in strain $\delta\varepsilon_{ij}$ leads to a variation of energy per unit volume

$$\delta u = \delta\varepsilon_{ij}\,\sigma_{ij}, \tag{C.1}$$

yielding

$$\sigma_{ij} = \frac{\partial u}{\partial \varepsilon_{ij}}. \tag{C.2}$$

By developing a model for the energy density u, one could derive the constitutive equations, that is, the relation between stress and strain. Considering the most general linear connection between the components of both tensors yields

$$\sigma_{ij} = C_{ijkl}\varepsilon_{kl}, \tag{C.3}$$

where C_{ijkl} is the stiffness tensor. This equation is the generalized Hooke's law. Therefore, the expression in (C.3) is the constitutive equation for a linear elastic material and can, in fact, be obtained using the energy density of an harmonic oscillator

$$u = \frac{1}{2}C_{ijkl}\varepsilon_{ij}\varepsilon_{kl}. \tag{C.4}$$

Regrading the stiffness tensor, because the stress tensor is symmetric,

$$C_{ijkl} = C_{jikl}, \tag{C.5}$$

reducing the number of independent constants from $3^4 = 81$ to $3 \times 3 \times 6 = 54$ (3×3 for kl and 6 for ij). Moreover, since the strain tensor is also symmetric,

$$C_{ijkl} = C_{ijlk}, \tag{C.6}$$

then for each of the 6 independent configurations of ij there are other 6 independent configurations of kl, giving a total of 36 independent constants. Furthermore, given (C.2),

$$\frac{\partial\sigma_{ij}}{\partial\varepsilon_{kl}} = \frac{\partial^2 u}{\partial\varepsilon_{kl}\varepsilon_{ij}} = \frac{\partial\sigma_{kl}}{\partial\varepsilon_{ij}} \tag{C.7}$$

therefore, using equation (C.3),

$$C_{ijkl} = C_{klij} \tag{C.8}$$

further reduces the number of independent constants to 21.

For an isotropic material and assuming total symmetry, the elements of C_{ijkl} must be scalars. In order for the energy to also be scalar, in the expression (C.4), the product $\varepsilon_{ij}\varepsilon_{kl}$ must be a scalar. The only two ways a product between two tensors can produce a scalar is either $\varepsilon_{ii}\varepsilon_{kk}$, or $\varepsilon_{ik}\varepsilon_{ik}$. This implies that it must be possible to write C_{ijkl} in terms of Kronecker delta products. The most general form C_{ijkl} can take is

$$C_{ijkl} = \lambda\delta_{ij}\delta_{kl} + \mu\delta_{ik}\delta_{jl} + \zeta\delta_{il}\delta_{jk}. \tag{C.9}$$

The symmetry $C_{ijkl} = C_{klij}$ is already satisfied. The other two symmetries ($C_{ijkl} = C_{jikl} = C_{ijlk}$) force the condition $\mu = \zeta$.

Therefore, for an isotropic material, the most general stiffness matrix is of the form

$$C_{ijkl} = \lambda\delta_{ij}\delta_{kl} + \mu\left(\delta_{ik}\delta_{jl} + \delta_{il}\delta_{jk}\right), \tag{C.10}$$

where λ and μ are called the Lamé constants. Equation (C.3), becomes

$$\sigma_{ij} = \lambda\delta_{ij}\varepsilon_{kk} + 2\mu\varepsilon_{ij}. \tag{C.11}$$

It is convenient to rewrite the constitutive equation in terms of other two parameters: the Young's modulus (E) and the Poisson ratio (ν).

Given a stress along the x-axis, for example, the Young's modulus is defined as

$$\sigma_{11} = E\varepsilon_{11}, \tag{C.12}$$

and the Poisson ratio is

$$\varepsilon_{22} = \varepsilon_{33} = -\nu\varepsilon_{11}. \tag{C.13}$$

For this system, the constitutive equations (C.11) are:

$$\sigma_{11} = \lambda\varepsilon_{ii} + 2\mu\varepsilon_{11}; \tag{C.14}$$

$$0 = \lambda\varepsilon_{ii} + 2\mu\varepsilon_{22}; \tag{C.15}$$

$$0 = \lambda\varepsilon_{ii} + 2\mu\varepsilon_{33}. \tag{C.16}$$

Summing all three equations gives

$$\sigma_{11} = (3\lambda + 2\mu)\,\varepsilon_{ii}, \tag{C.17}$$

that, by substituting on (C.14), arrives at

$$\varepsilon_{11} = \frac{\lambda + \mu}{\mu}\varepsilon_{ii}. \tag{C.18}$$

Using the equation (C.12), the expression for the Young modulus becomes

$$E = \frac{\mu\,(3\lambda + 2\mu)}{\lambda + \mu}. \tag{C.19}$$

Also, for the Poisson ratio (C.13), using equation (C.15), we have

$$\varepsilon_{22} = -\frac{1}{2}\frac{\lambda}{\mu}\varepsilon_{ii}, \tag{C.20}$$

that, by combining with equation (C.18), leads to

$$\nu = \frac{1}{2}\frac{\lambda}{\lambda+\mu}. \tag{C.21}$$

It is possible to invert both expressions and to write the constitutive equation in terms of E and ν.

From (C.21), we can isolate λ:

$$2\nu\left(\lambda+\mu\right) = \lambda \Leftrightarrow 2\nu\mu = \lambda\left(1-2\nu\right).$$

Rearranging, gives

$$\lambda = \frac{2\nu\mu}{1-2\nu}. \tag{C.22}$$

Substituting the previous expression on (C.19), yields

$$E = \frac{\mu\left(\frac{6\nu\mu}{1-2\nu}+2\mu\right)}{\frac{2\nu\mu}{1-2\nu}+\mu} = \frac{\frac{\mu}{1-2\nu}\left(6\nu\mu+2\mu-4\nu\mu\right)}{\frac{\mu}{1-2\nu}\left(2\nu+1-2\nu\right)} = 2\mu\left(1+\nu\right),$$

therefore

$$\mu = \frac{1}{2}\frac{E}{1+\nu} \tag{C.23}$$

and, from (C.22), we get

$$\lambda = \frac{\nu E}{\left(1+\nu\right)\left(1-2\nu\right)}. \tag{C.24}$$

Finally, equation (C.11) becomes

$$\sigma_{ij} = \frac{E}{\left(1+\nu\right)\left(1-2\nu\right)}\left(\nu\delta_{ij}\varepsilon_{kk} + \left(1-2\nu\right)\varepsilon_{ij}\right). \tag{C.25}$$

Finally, by inverting the aforementioned relations, in a matrix representation, for 3D, equation (C.11) can be rewritten as

$$\begin{pmatrix}\sigma_{11}\\ \sigma_{22}\\ \sigma_{33}\\ \sigma_{23}\\ \sigma_{31}\\ \sigma_{12}\end{pmatrix} = \frac{E}{\left(1+\nu\right)\left(1-2\nu\right)}\begin{pmatrix}1-\nu & \nu & \nu & 0 & 0 & 0\\ \nu & 1-\nu & \nu & 0 & 0 & 0\\ \nu & \nu & 1-\nu & 0 & 0 & 0\\ 0 & 0 & 0 & \frac{1}{2}\left(1-2\nu\right) & 0 & 0\\ 0 & 0 & 0 & 0 & \frac{1}{2}\left(1-2\nu\right) & 0\\ 0 & 0 & 0 & 0 & 0 & \frac{1}{2}\left(1-2\nu\right)\end{pmatrix}\begin{pmatrix}\varepsilon_{11}\\ \varepsilon_{22}\\ \varepsilon_{33}\\ 2\varepsilon_{23}\\ 2\varepsilon_{31}\\ 2\varepsilon_{12}\end{pmatrix}, \tag{C.26}$$

where the shear components of the strain vector have an explicit factor of two, in order to write the Frobenius product $\varepsilon_{ij}\sigma_{ij}$ as a simple inner product.

A special case of (C.26) is when the stress vector applied on a particular surface is zero. Under these conditions, a material is said to be under plane stress conditions. For example,

if the components $\sigma_{33} = \sigma_{13} = \sigma_{23} = \sigma_{31} = \sigma_{32} = 0$, then we have $\varepsilon_{23} = \varepsilon_{31} = 0$ trivially and the equation for σ_{33} reads:

$$0 = \nu\varepsilon_{11} + \nu\varepsilon_{22} + (1-\nu)\,\varepsilon_{33}. \tag{C.27}$$

Which becomes

$$\varepsilon_{33} = -\frac{\nu}{1-\nu}\left(\varepsilon_{11} + \varepsilon_{22}\right), \tag{C.28}$$

therefore, for equations of σ_{11} and σ_{22}, we have

$$\sigma_{11} = \frac{E}{(1+\nu)(1-2\nu)}\left[(1-\nu)\,\varepsilon_{11} + \nu\varepsilon_{22} - \frac{\nu^2}{1-\nu}\left(\varepsilon_{11} + \varepsilon_{22}\right)\right], \tag{C.29}$$

$$\sigma_{22} = \frac{E}{(1+\nu)(1-2\nu)}\left[\nu\varepsilon_{11} + (1-\nu)\,\varepsilon_{22} - \frac{\nu^2}{1-\nu}\left(\varepsilon_{11} + \varepsilon_{22}\right)\right], \tag{C.30}$$

which, rearranged and in matrix form, becomes

$$\begin{pmatrix}\sigma_{11}\\ \sigma_{22}\\ \sigma_{12}\end{pmatrix} = \frac{E}{1-\nu^2}\begin{pmatrix}1 & \nu & 0\\ \nu & 1 & 0\\ 0 & 0 & \frac{1}{2}(1-\nu)\end{pmatrix}\begin{pmatrix}\varepsilon_{11}\\ \varepsilon_{22}\\ 2\varepsilon_{12}\end{pmatrix}. \tag{C.31}$$

Appendix D

Shape Functions

It is going to be exemplified the process by which it is derived the shape functions for an element composed of, first, three nodes and, after that, four nodes. To reiterate, a FEM element is composed of N nodes. There is a quantity $q(\mathbf{x})$, which we are interested in interpolating inside the element, whose value is known at the nodes, that is $q^{(n)} = q(\mathbf{x}_n)$, where $\mathbf{x}_n$ is the position of the n-th node.

First, we need appropriate local coordinates (ξ, η, ζ). For example, for a 2D triangular element, the mapping, according to Fig. D.1, is

$$
\begin{aligned}
&(x^{(1)}, y^{(1)}) \to (0,0),\\
&(x^{(2)}, y^{(2)}) \to (1,0),\\
&(x^{(3)}, y^{(3)}) \to (0,1).
\end{aligned}
$$

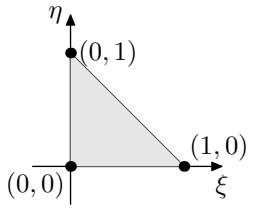

FIGURE D.1: Representation of the element using the new coordinates, that is, under the transformation on the left.

Using a Taylor series, equation (2.13), one can approximate the quantity $q(\xi, \eta)$ to the polynomial

$$q(\xi, \eta) \approx c_1 + c_2\xi + c_3\eta. \tag{D.1}$$

For each node there is an equation. In this case,

$$q(0,0) = q^{(1)} = c_1, \tag{D.2}$$
$$q(1,0) = q^{(2)} = c_1 + c_2, \tag{D.3}$$
$$q(0,1) = q^{(3)} = c_1 + c_3. \tag{D.4}$$

Inverting the relation yields

$$c_1 = q^{(1)}, \tag{D.5}$$
$$c_2 = q^{(2)} - q^{(1)}, \tag{D.6}$$
$$c_3 = q^{(3)} - q^{(1)}, \tag{D.7}$$

and, by inserting them back on (D.1), we have

$$q(\xi, \eta) \approx (1 - \xi - \eta)\, q^{(1)} + \xi q^{(2)} + \eta q^{(3)} \tag{D.8}$$

which, comparing with (2.14), means that

$$\phi^{(1)}(\xi,\eta) = 1 - \xi - \eta, \tag{D.9}$$
$$\phi^{(2)}(\xi,\eta) = \xi, \tag{D.10}$$
$$\phi^{(3)}(\xi,\eta) = \eta, \tag{D.11}$$

represented in Fig. D.3.

Similarly, for an element with four nodes (Fig. D.2), where

$$(x^{(1)}, y^{(1)}) \to (-1,-1),$$
$$(x^{(2)}, y^{(3)}) \to (+1,-1),$$
$$(x^{(3)}, y^{(3)}) \to (+1,+1),$$
$$(x^{(4)}, y^{(4)}) \to (-1,+1),$$

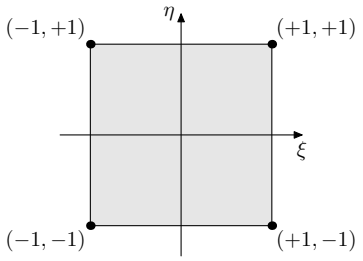

FIGURE D.2: Representation of the element using the new coordinates, that is, under the transformation on the left.

it is possible to derive the shape functions. Though the nodes could be mapped to $(0,0)$, $(1,0)$, $(1,1)$ and $(0,1)$, the choice of ± 1 is a little bit more convenient.

The Taylor expansion becomes

$$q(\xi,\eta) \approx c_1 + c_2\xi + c_3\eta + c_4\xi\eta, \tag{D.12}$$

and the equation system is now

$$q^{(1)} = c_1 - c_2 - c_3 + c_4, \tag{D.13}$$
$$q^{(2)} = c_1 + c_2 - c_3 - c_4, \tag{D.14}$$
$$q^{(3)} = c_1 + c_2 + c_3 + c_4, \tag{D.15}$$
$$q^{(4)} = c_1 - c_2 + c_3 - c_4. \tag{D.16}$$

Summing all equations we get

$$c_1 = \frac{1}{4}\left(q^{(1)} + q^{(2)} + q^{(3)} + q^{(4)}\right), \tag{D.17}$$

summing the first and fourth equations, we have

$$c_2 = \frac{1}{4}\left(-q^{(1)} + q^{(2)} + q^{(3)} - q^{(4)}\right), \tag{D.18}$$

summing the first and second equations, yields

$$c_3 = \frac{1}{4}\left(-q^{(1)} - q^{(2)} + q^{(3)} + q^{(4)}\right), \tag{D.19}$$

lastly, for the first and third equations,

$$c_4 = \frac{1}{4}\left(q^{(1)} - q^{(2)} + q^{(3)} - q^{(4)}\right). \tag{D.20}$$

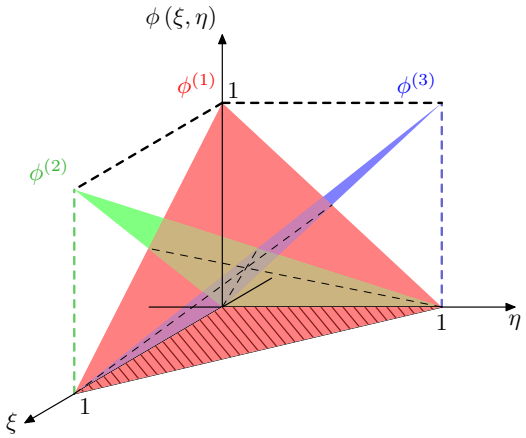

FIGURE D.3: Representation of the shape functions (D.9) in light red, (D.10) in light blue and (D.11) in light green. The plane $\xi O\eta$ contains the element.

Finally, we get

$$q(\xi,\eta) \approx \frac{1}{4}(1-\xi)(1-\eta)q^{(1)} + \frac{1}{4}(1+\xi)(1-\eta)q^{(2)} + \frac{1}{4}(1+\xi)(1+\eta)q^{(3)} + \frac{1}{4}(1-\xi)(1+\eta)q^{(4)} \quad \text{(D.21)}$$

Similarly, the shape functions for an element with four nodes are

$$\phi^{(1)}(\xi,\eta) = \frac{1}{4}(1-\xi)(1-\eta), \quad \text{(D.22)}$$

$$\phi^{(2)}(\xi,\eta) = \frac{1}{4}(1+\xi)(1-\eta), \quad \text{(D.23)}$$

$$\phi^{(3)}(\xi,\eta) = \frac{1}{4}(1+\xi)(1+\eta), \quad \text{(D.24)}$$

$$\phi^{(4)}(\xi,\eta) = \frac{1}{4}(1-\xi)(1+\eta), \quad \text{(D.25)}$$

represented in Fig. D.4.

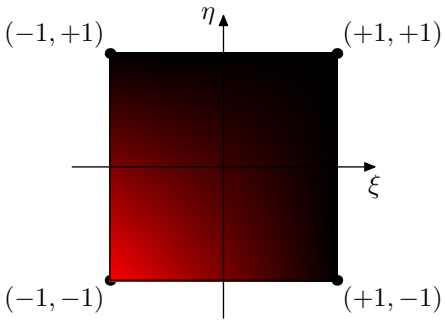

FIGURE D.4: Value of the shape function $\phi^{(1)}$ regarding the local coordinates, where red corresponds to the value 1 and black to the value 0. The rest of the shape functions are very similar and can be obtained through rotation of $\phi^{(1)}$.

Appendix E

Variational Formulation

It is easier to illustrate this procedure using an example. For the Poisson equation,

$$\nabla^2 u = f, \tag{E.1}$$

where $u = u(x, y)$ is the unknown function and $f = f(x, y)$ is a known function of the coordinates. Multiplying by a test function $v = v(x, y)$ and integrating over a volume V, the Poisson equation becomes

$$\int_V v\nabla^2 u \, dV = \int_V vf \, dV. \tag{E.2}$$

Using the identity,

$$\nabla \cdot (v\nabla u) = (\nabla v) \cdot (\nabla u) + v\nabla^2 u, \tag{E.3}$$

the previous expression becomes,

$$\int_V \nabla \cdot (v\nabla u) \, dV - \int_V (\nabla v) \cdot (\nabla u) \, dV = \int_V vf \, dV, \tag{E.4}$$

which, using Gauss's theorem, yields

$$\oint_S v\nabla u \, dS - \int_V (\nabla v) \cdot (\nabla u) \, dV = \int_V vf \, dV. \tag{E.5}$$

Regarding v, it is an arbitrary function taken from a specific set of square integrable functions with value $v = 0$ at the boundary of V. Therefore, the first term vanishes, leading to

$$\int_V (\nabla v) \cdot (\nabla u) \, dV = -\int_V vf \, dV. \tag{E.6}$$

This method is equivalent to virtual work formulation with the test function being a virtual change in u. For an electric field ($\mathbf{E}$), which must obey $\nabla^2 V = -\frac{\rho}{\epsilon_0}$, the energy inside a volume Ω is given by

$$U = \frac{\epsilon_0}{2} \int_\Omega \mathbf{E} \cdot \mathbf{E} \, d\Omega, \tag{E.7}$$

where ϵ_0 is the vacuum permittivity. Under a change $\delta\mathbf{E}$, the variation of energy is

$$\delta U = \epsilon_0 \int_\Omega \mathbf{E} \cdot \delta\mathbf{E} \, d\Omega, \tag{E.8}$$

due to the fact that $\mathbf{E} = -\nabla V$, this expression leads to,

$$\delta U = \epsilon_0 \int_\Omega (\nabla V) \cdot (\nabla \delta V)\, d\Omega, \tag{E.9}$$

where δV is a virtual electric potential.

Note that the change in energy due to a charge distribution is

$$\delta W = \int_\Omega \rho \delta V\, d\Omega. \tag{E.10}$$

Under the principle of virtual work, the internal energy variation and the change of external work must be equal, therefore,

$$\int_\Omega (\nabla V) \cdot (\nabla \delta V)\, d\Omega = \int_\Omega \frac{\rho}{\epsilon_0} \delta V\, d\Omega. \tag{E.11}$$

By comparing with (E.6), the weak form of the Poisson equation is recovered when $u = V$,$v = \delta V$ and $f = -\frac{\rho}{\epsilon_0}$. Furthermore, by comparing with (E.1), recovers the strong form $\nabla^2 V = -\frac{\rho}{\epsilon_0}$.

Appendix F

Assembly of the Global Stiffness Matrix

Here it will be illustrated the direct stiffness method for joining individual element's stiffness matrices. Given the example in Fig. F.1, suppose we have the stiffness matrices for each element $K_{ij}^{(I)}$, $K_{ij}^{(II)}$, $K_{ij}^{(III)}$, $K_{ij}^{(IV)}$.

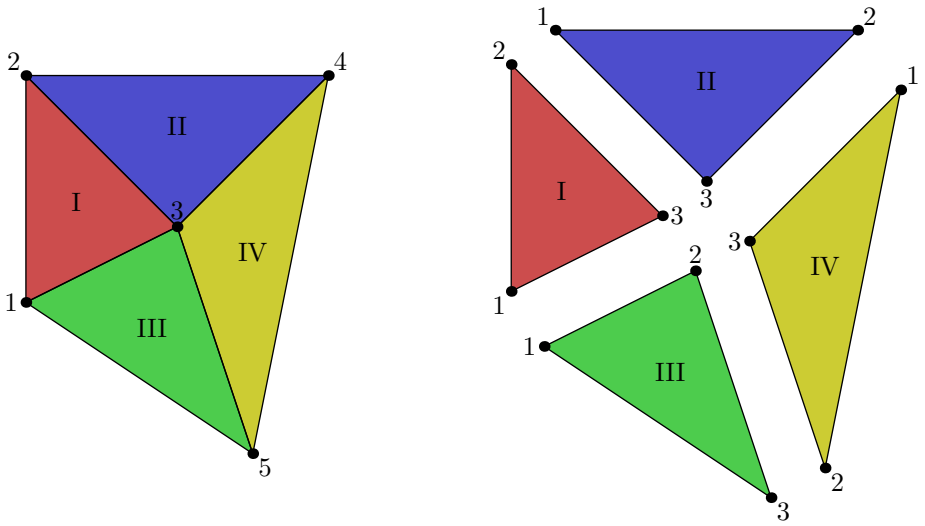

FIGURE F.1: A very small mesh with only four elements (I, II, III and IV) and five nodes. On the left the nodes have globally numbered indices. On the right, however, each element has nodes with local indices one through three.

By the direct stiffness method we have,

$$K_{\alpha\beta} = \sum_e K_{ij}^{(e)} = K_{ij}^{(I)} + K_{ij}^{(II)} + K_{ij}^{(III)} + K_{ij}^{(IV)}. \tag{F.1}$$

where $\alpha, \beta = 1, 2, 3, 4, 5$ are global indices and $i, j = 1, 2, 3$ are local indices. For an element e, the stiffness matrix, using the local indices, is

$$K_{ij}^{(e)} = \begin{pmatrix} K_{11}^{(e)} & K_{12}^{(e)} & K_{13}^{(e)} \\ K_{21}^{(e)} & K_{22}^{(e)} & K_{23}^{(e)} \\ K_{31}^{(e)} & K_{32}^{(e)} & K_{33}^{(e)} \end{pmatrix}. \tag{F.2}$$

Using the global indices, however, for element I,

$$K_{\alpha\beta}^{(I)} = \begin{pmatrix} K_{11}^{(I)} & K_{12}^{(I)} & K_{13}^{(I)} & 0 & 0 \\ K_{21}^{(I)} & K_{22}^{(I)} & K_{23}^{(I)} & 0 & 0 \\ K_{31}^{(I)} & K_{32}^{(I)} & K_{33}^{(I)} & 0 & 0 \\ 0 & 0 & 0 & 0 & 0 \\ 0 & 0 & 0 & 0 & 0 \end{pmatrix}. \tag{F.3}$$

Summing the second matrix, paying close attention to the indices,

$$K_{\alpha\beta}^{(I)} + K_{\alpha\beta}^{(II)} = \begin{pmatrix} K_{11}^{(I)} & K_{12}^{(I)} & K_{13}^{(I)} & 0 & 0 \\ K_{21}^{(I)} & K_{22}^{(I)} + K_{11}^{(II)} & K_{23}^{(I)} + K_{13}^{(II)} & K_{12}^{(II)} & 0 \\ K_{31}^{(I)} & K_{32}^{(I)} + K_{31}^{(II)} & K_{33}^{(I)} + K_{33}^{(II)} & K_{32}^{(II)} & 0 \\ 0 & K_{21}^{(II)} & K_{23}^{(II)} & K_{22}^{(II)} & 0 \\ 0 & 0 & 0 & 0 & 0 \end{pmatrix}. \tag{F.4}$$

Summing the third matrix,

$$K_{\alpha\beta}^{(I)} + K_{\alpha\beta}^{(II)} + K_{\alpha\beta}^{(III)} = \begin{pmatrix} K_{11}^{(I)} + K_{11}^{(III)} & K_{12}^{(I)} & K_{13}^{(I)} + K_{12}^{(III)} & 0 & K_{13}^{(III)} \\ K_{21}^{(I)} & K_{22}^{(I)} + K_{11}^{(II)} & K_{23}^{(I)} + K_{13}^{(II)} & K_{12}^{(II)} & 0 \\ K_{31}^{(I)} + K_{21}^{(III)} & K_{32}^{(I)} + K_{31}^{(II)} & K_{33}^{(I)} + K_{33}^{(II)} + K_{22}^{(III)} & K_{32}^{(II)} & K_{23}^{(III)} \\ 0 & K_{21}^{(II)} & K_{23}^{(II)} & K_{22}^{(II)} & 0 \\ K_{31}^{(III)} & 0 & K_{32}^{(III)} & 0 & K_{33}^{(III)} \end{pmatrix}. \tag{F.5}$$

Finally,

$$K_{\alpha\beta} = K_{\alpha\beta}^{(I)} + K_{\alpha\beta}^{(II)} + K_{\alpha\beta}^{(III)} + K_{\alpha\beta}^{(IV)} = \begin{pmatrix} K_{11}^{(I)}+K_{11}^{(III)} & K_{12}^{(I)} & K_{13}^{(I)}+K_{12}^{(III)} & 0 & K_{13}^{(III)} \\ K_{21}^{(I)} & K_{22}^{(I)}+K_{11}^{(II)} & K_{23}^{(I)}+K_{13}^{(II)} & K_{12}^{(II)} & 0 \\ K_{31}^{(I)}+K_{21}^{(III)} & K_{32}^{(I)}+K_{31}^{(II)} & K_{33}^{(I)}+K_{33}^{(II)}+K_{22}^{(III)}+K_{33}^{(IV)} & K_{32}^{(II)}+K_{31}^{(IV)} & K_{23}^{(III)}+K_{32}^{(IV)} \\ 0 & K_{21}^{(II)} & K_{23}^{(II)}+K_{13}^{(IV)} & K_{22}^{(II)}+K_{11}^{(IV)} & K_{12}^{(IV)} \\ K_{31}^{(III)} & 0 & K_{32}^{(III)}+K_{23}^{(IV)} & K_{21}^{(IV)} & K_{33}^{(III)}+K_{22}^{(IV)} \end{pmatrix}. \tag{F.6}$$

This matrix is rather dense, however, in this case, most elements share sides with each other. In the cases where the number of elements is large, most of them will not even share a node, therefore the matrix becomes increasingly sparse.

Appendix G

Preconditioned Conjugate Gradient

The equation to be solved is (2.52), which is of the form $\mathbb{A}\mathbf{x} = \mathbf{b}$, after imposing boundary conditions. For that effect, it is going to be used a method called preconditioned conjugate gradient (PCG), which is an iterative method that, taking an initial guess at $\mathbf{x}_0$, it produces another vector closer to the solution, converging towards it, that is, until the difference between the successive vectors is smaller than some precision parameter. Firstly, however, it is going to be discussed its predecessor, the Conjugate Gradient (CG).

Following the derivation done in [51], let

$$f(\mathbf{x}) = -\frac{1}{2}\mathbf{x^T}\mathbb{A}\mathbf{x} + \mathbf{x^T}\mathbf{b} \tag{G.1}$$

be a function we want to minimize. Its gradient is,

$$\nabla f(\mathbf{x}) = \mathbf{b} - \mathbb{A}\mathbf{x}, \tag{G.2}$$

and we are looking for $\mathbf{x}^*$, such that,

$$\nabla f(\mathbf{x}^*) = \mathbf{b} - \mathbb{A}\mathbf{x}^* = 0, \tag{G.3}$$

which is the equation we want to solve.

Supposing we are at position $\mathbf{x_i}$ and we want to advance towards $\mathbf{x}^*$, step by step. Let $\mathbf{p_i}$ be the direction in which we are advancing, such that,

$$\mathbf{x_{i+1}} = \mathbf{x_i} + \alpha_i \mathbf{p_i}, \tag{G.4}$$

where α_i is the step size. By minimizing $f(\mathbf{x_{i+1}})$ with respect to α_i, along the direction $\mathbf{p_i}$, the value of α_i can be found,

$$\begin{aligned}\frac{\partial f(\mathbf{x_{i+1}})}{\partial \alpha_i} = \frac{\partial \mathbf{x_{i+1}}^{\mathbf{T}}}{\partial \alpha_i}\nabla f(\mathbf{x_{i+1}}) = \mathbf{p_i}^{\mathbf{T}}\left(\mathbf{b} - \mathbb{A}\mathbf{x_{i+1}}\right) = \mathbf{p_i}^{\mathbf{T}}\left(\mathbf{b} - \mathbb{A}\left(\mathbf{x_i} + \alpha_i\mathbf{p_i}\right)\right) \\ = \mathbf{p_i}^{\mathbf{T}}\nabla f\left(\mathbf{x_i}\right) - \alpha_i \mathbf{p_i}^{\mathbf{T}}\mathbb{A}\mathbf{p_i} = 0,\end{aligned} \tag{G.5}$$

rewriting in terms of α_i, renaming the gradient as the residual, $\mathbf{r_i} = \nabla f(\mathbf{x_i})$,

$$\alpha_i = \frac{\mathbf{p_i}^{\mathbf{T}}\mathbf{r_i}}{\mathbf{p_i}^{\mathbf{T}}\mathbb{A}\mathbf{p_i}}. \tag{G.6}$$

Note that, in equation (G.5), it is required that,

$$\mathbf{p_i}^{\mathbf{T}}\mathbf{r_{i+1}} = 0. \tag{G.7}$$

Additionally, the calculation of the next residual is,

$$\mathbf{r_{i+1}} = \mathbf{b} - \mathbb{A}\mathbf{x_{i+1}} = \mathbf{b} - \mathbb{A}\mathbf{x_i} - \alpha_i \mathbb{A}\mathbf{p_i} = \mathbf{r_i} - \alpha_i \mathbb{A}\mathbf{p_i} \tag{G.8}$$

The steepest descent method is obtained when the directions $\mathbf{p_i}$ are equal to the gradient in the position $\mathbf{r_i}$. However, in the conjugate gradient (CG) method, we minimize along $\mathbb{A}$-orthogonal (conjugate) directions, that is,

$$\mathbf{p_i}^{\mathbf{T}}\mathbb{A}\mathbf{p_j} = 0,\ i \neq j. \tag{G.9}$$

With a set of n mutually conjugate directions, $\mathbf{p_i}$, by spanning a basis according to this set, the solution $\mathbf{x}^*$ can be written as,

$$\mathbf{x}^* = \sum_{i=1}^{n} \alpha_i \mathbf{p_i}, \tag{G.10}$$

where n is the dimension of the matrix. Therefore,

$$\mathbb{A}\mathbf{x}^* = \mathbf{b}, \tag{G.11}$$

becomes,

$$\mathbb{A}\sum_{i=1}^{n} \alpha_i \mathbf{p_i} = \sum_{i=1}^{n} \alpha_i \mathbb{A}\mathbf{p_i} = \mathbf{b}, \tag{G.12}$$

which, multiplying by $\mathbf{p_j}^{\mathbf{T}}$, on the left, yields,

$$\sum_{i=1}^{n} \alpha_i \mathbf{p_j}^{\mathbf{T}}\mathbb{A}\mathbf{p_i} = \alpha_j \mathbf{p_j}^{\mathbf{T}}\mathbb{A}\mathbf{p_j} = \mathbf{p_j}^{\mathbf{T}}\mathbf{b}, \tag{G.13}$$

Therefore,

$$\alpha_i = \frac{\mathbf{p_i}^{\mathbf{T}}\mathbf{b}}{\mathbf{p_i}^{\mathbf{T}}\mathbb{A}\mathbf{p_i}}, \tag{G.14}$$

which, in terms of $\mathbf{r_i}$, becomes,

$$\alpha_i = \frac{\mathbf{p_i}^{\mathbf{T}}\left(\mathbb{A}\mathbf{x_i} + \mathbf{r_i}\right)}{\mathbf{p_i}^{\mathbf{T}}\mathbb{A}\mathbf{p_i}} = \frac{\mathbf{p_i}^{\mathbf{T}}\left(\mathbb{A}\sum_{j=1}^{i-1}\alpha_j\mathbf{p_j} + \mathbf{r_i}\right)}{\mathbf{p_i}^{\mathbf{T}}\mathbb{A}\mathbf{p_i}} = \frac{\mathbf{p_i}^{\mathbf{T}}\mathbf{r_i}}{\mathbf{p_i}^{\mathbf{T}}\mathbb{A}\mathbf{p_i}}, \tag{G.15}$$

recovering equation (G.6).

Moreover, because of conjugation conditions and (G.7), for $i > j$,

$$\mathbf{p_j}^{\mathbf{T}}\mathbf{r_i} = \mathbf{p_j}^{\mathbf{T}}\left(\mathbf{r_{j+1}} - \alpha_{\mathbf{j+1}}\mathbb{A}\mathbf{p_{j+1}} - \cdots - \alpha_{\mathbf{i-1}}\mathbb{A}\mathbf{p_{i-1}}\right) = \mathbf{p_j}^{\mathbf{T}}\mathbf{r_{j+1}} = 0. \tag{G.16}$$

Suppose we try to choose a new direction, such that it is conjugate to all previous directions,

$$\mathbf{p_i} = \mathbf{u_i} + \sum_{j=1}^{i-1} \beta_{ij} \mathbf{p_j}, \tag{G.17}$$

where $\mathbf{u}_1, \mathbf{u}_2, \ldots, \mathbf{u}_n$ are a set of linearly independent vectors. By imposing the conjugation condition,

$$\mathbf{p_k}^\mathbf{T} \mathbb{A} \mathbf{p_i} = \mathbf{p_k}^\mathbf{T} \mathbb{A} \mathbf{u_i} + \sum_{j=1}^{i-1} \beta_{ij} \mathbf{p_k}^\mathbf{T} \mathbb{A} \mathbf{p_j} = 0,\ k < i, \tag{G.18}$$

implies,

$$\mathbf{p_k}^\mathbf{T} \mathbb{A} \mathbf{u_i} + \beta_{ik} \mathbf{p_k}^\mathbf{T} \mathbb{A} \mathbf{p_k} = 0,\ k < i, \tag{G.19}$$

which leads to,

$$\beta_{ij} = -\frac{\mathbf{p_j}^\mathbf{T} \mathbb{A} \mathbf{u_i}}{\mathbf{p_j}^\mathbf{T} \mathbb{A} \mathbf{p_j}}. \tag{G.20}$$

According to this construction, we can write,

$$\mathbf{p_j}^\mathbf{T} \mathbf{r_i} = \mathbf{u_j}^\mathbf{T} \mathbf{r_i} + \sum_{k=1}^{j-1} \beta_{jk} \mathbf{p_k}^\mathbf{T} \mathbf{r_i},\ j < i, \tag{G.21}$$

which by equation (G.16), becomes

$$\mathbf{u_j}^\mathbf{T} \mathbf{r_i} = 0,\ j < i. \tag{G.22}$$

And, for the same reason,

$$\mathbf{p_i}^\mathbf{T} \mathbf{r_i} = \mathbf{u_i}^\mathbf{T} \mathbf{r_i} + \sum_{j=1}^{i-1} \beta_{ij} \mathbf{p_j}^\mathbf{T} \mathbf{r_i} = \mathbf{u_i}^\mathbf{T} \mathbf{r_i}. \tag{G.23}$$

Choosing the basis as the successive residuals, we get,

$$\mathbf{r_j}^\mathbf{T} \mathbf{r_i} = 0,\ i \neq j, \tag{G.24}$$

$$\alpha_i = \frac{\mathbf{r_i}^\mathbf{T} \mathbf{r_i}}{\mathbf{p_i}^\mathbf{T} \mathbb{A} \mathbf{p_i}}. \tag{G.25}$$

Furthermore,

$$\mathbf{r_i}^\mathbf{T} \mathbf{r_{j+1}} = \mathbf{r_i}^\mathbf{T} \mathbf{r_j} - \alpha_j \mathbf{r_i}^\mathbf{T} \mathbb{A} \mathbf{p_j} \Leftrightarrow \mathbf{r_i}^\mathbf{T} \mathbb{A} \mathbf{p_j} = \frac{1}{\alpha_j} \left(\mathbf{r_i}^\mathbf{T} \mathbf{r_j} - \mathbf{r_i}^\mathbf{T} \mathbf{r_{j+1}} \right), \tag{G.26}$$

and, according to (G.20) and (G.24), becomes

$$\beta_{ij} = \begin{cases} -\frac{1}{\alpha_i} \frac{\mathbf{r_i}^\mathbf{T} \mathbf{r_i}}{\mathbf{p_i}^\mathbf{T} \mathbb{A} \mathbf{p_i}} & j = i, \\ \frac{1}{\alpha_{i-1}} \frac{\mathbf{r_i}^\mathbf{T} \mathbf{r_i}}{\mathbf{p_{i-1}}^\mathbf{T} \mathbb{A} \mathbf{p_{i-1}}} & j = i-1, . \\ 0 & j < i \end{cases} \tag{G.27}$$

Therefore, the next direction can be written as, according to (G.17),

$$\mathbf{p_i} = \mathbf{r_i} + \beta_{ii-1}\mathbf{p_{i-1}} = \mathbf{r_i} + \beta_i \mathbf{p_{i-1}}, \tag{G.28}$$

where $\beta_i = \beta_{ii-1}$ is the only nonzero term in the summation. and β_i can be simplified further,

$$\beta_i = \frac{\mathbf{p_{i-1}}^\mathbf{T}\mathbb{A}\mathbf{p_{i-1}}}{\mathbf{r_{i-1}}^\mathbf{T}\mathbf{r_{i-1}}} \frac{\mathbf{r_i}^\mathbf{T}\mathbf{r_i}}{\mathbf{p_{i-1}}^\mathbf{T}\mathbb{A}\mathbf{p_{i-1}}} = \frac{\mathbf{r_i}^\mathbf{T}\mathbf{r_i}}{\mathbf{r_{i-1}}^\mathbf{T}\mathbf{r_{i-1}}} \tag{G.29}$$

This way, we find a new direction along which we minimize the function f. The final algorithm is simply:

1. start at a position $\mathbf{x_1}$;
2. calculate first direction equal to residual at $\mathbf{x_1}$: $\mathbf{p_1} = \mathbf{r_1} = \mathbf{b} - \mathbb{A}\mathbf{x_1}$;
3. let $i = 1$;
4. $\alpha_i = \frac{\mathbf{r_i}^\mathbf{T}\mathbf{r_i}}{\mathbf{p_i}^\mathbf{T}\mathbb{A}\mathbf{p_i}}$;
5. $\mathbf{x_{i+1}} = \mathbf{x_i} + \alpha_i \mathbf{p_i}$;
6. $\mathbf{r_{i+1}} = \mathbf{r_i} - \alpha_i \mathbb{A}\mathbf{p_i}$;
7. $\beta_{i+1} = \frac{\mathbf{r_{i+1}}^\mathbf{T}\mathbf{r_{i+1}}}{\mathbf{r_i}^\mathbf{T}\mathbf{r_i}}$;
8. $\mathbf{p_{i+1}} = \mathbf{r_{i+1}} + \beta_{i+1}\mathbf{p_i}$;
9. $i = i + 1$;
10. go to step 4. until $i = n$, or there is enough precision for the result, $\mathbf{x_i}$.

The precision can be measured by various different methods, for example,

$$\mathbf{r_i}^\mathbf{T}\mathbf{r_i} < \delta\ \mathbf{r_0}^\mathbf{T}\mathbf{r_0},$$
$$\mathbf{r_i}^\mathbf{T}\mathbf{r_i} < \delta\ \mathbf{b}^\mathbf{T}\mathbf{b},$$

where δ is some sort of threshold value, are both valid choices.

The PCG consists of finding $\mathbf{x}$ indirectly by solving

$$\mathbb{M}^{-1}\mathbb{A}\mathbf{x} = \mathbb{M}^{-1}\mathbf{b}, \tag{G.30}$$

where $\mathbb{M}$ is the preconditioning matrix. When $\mathbb{M}^{-1} = \mathbf{I}$, that is, when $\mathbb{M}^{-1}$ is the identity matrix, the equation system $\mathbb{A}\mathbf{x} = \mathbf{b}$ is recovered, however, when $\mathbb{M}^{-1} = \mathbb{A}^{-1}$, the problem, the value of $\mathbf{x}$ is automatically solved. The idea behind the PCG method is to use $\mathbb{M}^{-1}$ as an easily computable matrix somewhere between $\mathbf{I}$ and $\mathbb{A}^{-1}$, in order to improve convergence.

Let the matrix,

$$\mathbb{M} = \mathbb{E}\mathbb{E}^\mathbf{T}, \tag{G.31}$$

be the preconditioning matrix, built from the unknown matrix $\mathbb{E}$.

Transforming the system into,

$$\mathbb{E}^{-1}\mathbb{A}\mathbb{E}^{-\mathbf{T}}\widehat{\mathbf{x}} = \mathbb{E}^{-1}\mathbf{b}, \tag{G.32}$$

$$\hat{\mathbf{x}} = \mathbb{E}^{\mathbf{T}}\mathbf{x}, \tag{G.33}$$

the CG algorithm for the first equation is,

1. start at a position $\widehat{\mathbf{x}}_\mathbf{1} = \mathbb{E}^{\mathbf{T}}\mathbf{x}_\mathbf{1}$;
2. calculate first direction equal to residual at $\widehat{\mathbf{x}}_\mathbf{1}$: $\widehat{\mathbf{p}}_\mathbf{1} = \widehat{\mathbf{r}}_\mathbf{1} = \mathbb{E}^{-1}\mathbf{b} - \mathbb{E}^{-1}\mathbb{A}\mathbb{E}^{-\mathbf{T}}\widehat{\mathbf{x}}_\mathbf{1}$;
3. let $i = 1$;
4. $\alpha_i = \frac{\widehat{\mathbf{r}}_\mathbf{i}^{\mathbf{T}}\widehat{\mathbf{r}}_\mathbf{i}}{\widehat{\mathbf{p}}_\mathbf{i}^{\mathbf{T}}\mathbb{E}^{-1}\mathbb{A}\mathbb{E}^{-\mathbf{T}}\widehat{\mathbf{p}}_\mathbf{i}}$;
5. $\widehat{\mathbf{x}}_{\mathbf{i+1}} = \widehat{\mathbf{x}}_\mathbf{i} + \alpha_i\widehat{\mathbf{p}}_\mathbf{i}$;
6. $\widehat{\mathbf{r}}_{\mathbf{i+1}} = \widehat{\mathbf{r}}_\mathbf{i} - \alpha_i\mathbb{E}^{-1}\mathbb{A}\mathbb{E}^{-\mathbf{T}}\widehat{\mathbf{p}}_\mathbf{i}$;
7. $\beta_{i+1} = \frac{\widehat{\mathbf{r}}_{\mathbf{i+1}}^{\mathbf{T}}\widehat{\mathbf{r}}_{\mathbf{i+1}}}{\widehat{\mathbf{r}}_\mathbf{i}^{\mathbf{T}}\widehat{\mathbf{r}}_\mathbf{i}}$;
8. $\widehat{\mathbf{p}}_{\mathbf{i+1}} = \widehat{\mathbf{r}}_{\mathbf{i+1}} + \beta_{i+1}\widehat{\mathbf{p}}_\mathbf{i}$;
9. $i = i + 1$;
10. go to step 4. until $i = n$, or there is enough precision for the result, $\widehat{\mathbf{x}}_\mathbf{i}$;
11. solve $\widehat{\mathbf{x}}_\mathbf{i} = \mathbb{E}^{\mathbf{T}}\mathbf{x}_\mathbf{i}$ for $\mathbf{x}_\mathbf{i}$.

However, having no expression for $\mathbb{E}$, this seems very unpractical. Luckily, there is a carefully thought out transformation which allows the elimination of $\mathbb{E}$ in the equations. Effectively, substituting,

$$\widehat{\mathbf{r}}_\mathbf{i} = \mathbb{E}^{-1}\mathbf{r}_\mathbf{i}, \tag{G.34}$$

$$\widehat{\mathbf{p}}_\mathbf{i} = \mathbb{E}^{\mathbf{T}}\mathbf{p}_\mathbf{i}, \tag{G.35}$$

and remembering that,

$$\widehat{\mathbf{x}}_\mathbf{i} = \mathbb{E}^{\mathbf{T}}\mathbf{x}_\mathbf{i}, \tag{G.36}$$

$$\mathbb{M}^{-1} = \mathbb{E}^{-\mathbf{T}}\mathbb{E}^{-1}, \tag{G.37}$$

the PCG algorithm becomes, finally,

1. start at a position $\mathbf{x}_\mathbf{1}$;
2. calculate first residual at $\mathbf{x}_\mathbf{1}$: $\mathbf{r}_\mathbf{1} = \mathbf{b} - \mathbb{A}\mathbf{x}_\mathbf{1}$;
3. calculate the first direction: $\mathbf{p}_\mathbf{1} = \mathbb{M}^{-1}\mathbf{r}_\mathbf{1}$;
4. let $i = 1$;
5. $\alpha_i = \frac{\mathbf{r}_\mathbf{i}^{\mathbf{T}}\mathbb{M}^{-1}\mathbf{r}_\mathbf{i}}{\mathbf{p}_\mathbf{i}^{\mathbf{T}}\mathbb{A}\mathbf{p}_\mathbf{i}}$;

6. $\mathbf{x_{i+1}} = \mathbf{x_i} + \alpha_i \mathbf{p_i}$;
7. $\mathbf{r_{i+1}} = \mathbf{r_i} - \alpha_i \mathbb{A}\mathbf{p_i}$;
8. $\beta_{i+1} = \frac{\mathbf{r_{i+1}}^{\mathbf{T}} \mathbb{M}^{-1} \mathbf{r_{i+1}}}{\mathbf{r_i}^{\mathbf{T}} \mathbb{M}^{-1} \mathbf{r_i}}$;
9. $\mathbf{p_{i+1}} = \mathbb{M}^{-1}\mathbf{r_{i+1}} + \beta_{i+1}\mathbf{p_i}$;
10. $i = i + 1$;
11. go to step 5. until $i = n$, or there is enough precision for the result, $\mathbf{x_i}$.

One value typically used for $\mathbb{M}^{-1}$ is the inverse of the diagonal of $\mathbb{A}$, i.e., $\mathbb{M}^{-1} = [\mathrm{diag}\,(\mathbb{A})]^{-1}$. Another example often used, is the incomplete Cholesky preconditioning, derived from Cholesky factorization, or other more sophisticated and quickly computable approximations to $\mathbb{A}^{-1}$.

Glossary

Actin Filament One of the major type of components of the cytoskeleton, often called microfilament. It is a thin linear polymer made from the actin protein and participates in cell signaling, cell migration, transport of material and in the contraction of the cell.

Anastomosis In the context of sprouting angiogenesis, this term refers to connection between two sprouts.

Angiogenesis The formation of new blood vessels from pre-existing ones. Sprouting angiogenesis is a specific type of angiogenesis in which cells of the initial vessel rearrange into small sprouts. The sprout's leading cell is of a specific phenotype called tip cell and is responsible for orienting the sprout. Following the tip cell, the stalk cells correspond to a more proliferative phenotype.

Cadherin A class of transmembrane proteins that intermediate cell-cell adhesion.

Chemotaxis Directed cell migration according to the gradient of concentration of a certain chemical signal.

Durotaxis Directed cell migration towards greater rigidity of the surrounding extracellular matrix.

Extracellular Matrix A collection of fibrous proteins secreted by cells which fills up the space between cells. This structure provides mechanical and biochemical stability to the cells it surrounds.

Focal Adhesion A macromolecular structure composed of a large collection of integrin molecules and their respective intracellular auxiliary proteins. By being connected to the actin cytoskeleton, this structure allows for strong cell-matrix adhesion, signaling and traction force generation.

Homeostasis The active regulation towards a somewhat stable, hence favorable, state of equilibrium of a system.

Integrin Transmembrane protein complex composed of two subunits responsible for cell-matrix adhesion. By recruiting adapter proteins and connecting to the cytoskeleton, it is also able to transmit signals from the ECM.

Mechanosensing The biochemical and mechanical processes of converting physical cues into biochemical signals.

Metastasis Cancer cells break away from the initial tumor and for new masses of cancer cells in other regions of the body. This process is associated with a more invasive phenotype, typically referred to as metastatic.

Morphogenesis The process by which cells rearrange into tissues in the development of the embryo, sometimes referred to as embryogenesis.

Strain Stiffening The phenomenon when certain materials, when stretched, respond by increasing their rigidity.

Vasculogenesis The formation of a network of blood vessels *de novo*, that is, without pre-existing blood vessels.

Bibliography

[1] Stuart A. Kauffman. *The Origins of Order: Self-Organization and Selection in Evolution*. Oxford University Press, 1993. ISBN: 0195058119.

[2] A. J. Koch and H. Meinhardt. "Biological pattern formation: from basic mechanisms to complex structures". In: *Reviews of Modern Physics* 66.4 (1994), pp. 1481–1507. DOI: 10.1103/revmodphys.66.1481.

[3] D.S Charnock-Jones, P Kaufmann, and T.M Mayhew. "Aspects of Human Fetoplacental Vasculogenesis and Angiogenesis. I. Molecular Regulation". In: *Placenta* 25.2–3 (2004), pp. 103 –113. ISSN: 0143-4004. DOI: 10.1016/j.placenta.2003.10.004.

[4] Markus Loeffler and Ingo Roeder. "Tissue Stem Cells: Definition, Plasticity, Heterogeneity, Self-Organization and Models – A Conceptual Approach". In: *Cells Tissues Organs* 171.1 (2002), pp. 8–26. DOI: 10.1159/000057688.

[5] C. Damiani et al. "Cell–cell interaction and diversity of emergent behaviours". In: *IET Systems Biology* 5.2 (2011), pp. 137–144. DOI: 10.1049/iet-syb.2010.0039.

[6] Barry M Gumbiner. "Cell Adhesion: The Molecular Basis of Tissue Architecture and Morphogenesis". In: *Cell* 84.3 (1996), pp. 345–357. DOI: 10.1016/s0092-8674(00)81279-9.

[7] H.-B. Wang et al. "Focal adhesion kinase is involved in mechanosensing during fibroblast migration". In: *Proceedings of the National Academy of Sciences* 98.20 (2001), pp. 11295–11300. DOI: 10.1073/pnas.201201198.

[8] S. J. Singer and G. L. Nicolson. "The Fluid Mosaic Model of the Structure of Cell Membranes". In: *Science* 175.4023 (1972), pp. 720–731. DOI: 10.1126/science.175.4023.720.

[9] Harvey Lodsih et al. *Molecular Cell Biology*. W H Freeman & Co (Sd), 1999. ISBN: 0716731363.

[10] Gary J. Doherty and Harvey T. McMahon. "Mediation, Modulation, and Consequences of Membrane-Cytoskeleton Interactions". In: *Annu. Rev. Biophys.* 37.1 (2008), pp. 65–95. DOI: 10.1146/annurev.biophys.37.032807.125912.

[11] Bill Wickstead and Keith Gull. "The evolution of the cytoskeleton". In: *J Cell Biol* 194.4 (2011), pp. 513–525. DOI: 10.1083/jcb.201102065.

[12] C. Frantz, K. M. Stewart, and V. M. Weaver. "The extracellular matrix at a glance". In: *Journal of Cell Science* 123.24 (2010), pp. 4195–4200. DOI: 10.1242/jcs.023820.

[13] Daniel A. Fletcher and R. Dyche Mullins. "Cell mechanics and the cytoskeleton". In: *Nature* 463.7280 (2010), pp. 485–492. DOI: 10.1038/nature08908.

[14] William P. Daley, Sarah B. Peters, and Melinda Larsen. “Extracellular matrix dynamics in development and regenerative medicine”. In: *Journal of Cell Science* 121.3 (2008), pp. 255–264. ISSN: 0021-9533.

[15] S M Albelda and C A Buck. “Integrins and other cell adhesion molecules.” In: *The FASEB Journal* 4.11 (1990), pp. 2868–80.

[16] D. B. Ivanov, M. P. Philippova, and V. A. Tkachuk. “Structure and Functions of Classical Cadherins”. In: *Biochemistry (Moscow)* 66.10 (2001), pp. 1174–1186. ISSN: 1608-3040.

[17] Bing-Hao Luo, Christopher V. Carman, and Timothy A. Springer. “Structural Basis of Integrin Regulation and Signaling”. In: *Annual Review of Immunology* 25.1 (2007), pp. 619–647. DOI: 10.1146/annurev.immunol.25.022106.141618.

[18] Michele A Wozniak et al. “Focal adhesion regulation of cell behavior”. In: *Biochimica et Biophysica Acta (BBA) - Molecular Cell Research* 1692.2-3 (2004), pp. 103–119. DOI: 10.1016/j.bbamcr.2004.04.007.

[19] A. J. Ridley. “Cell Migration: Integrating Signals from Front to Back”. In: *Science* 302.5651 (2003), pp. 1704–1709. DOI: 10.1126/science.1092053.

[20] Laurent Lamalice, Fabrice Le Boeuf, and Jacques Huot. “Endothelial Cell Migration During Angiogenesis”. In: *Circulation Research* 100.6 (2007), pp. 782–794. DOI: 10.1161/01.RES.0000259593.07661.1e.

[21] James H-C. Wang and Jeen-Shang Lin. “Cell traction force and measurement methods”. In: *Biomechanics and Modeling in Mechanobiology* 6.6 (2007), pp. 361–371. DOI: 10.1007/s10237-006-0068-4.

[22] Ben Harland, Sam Walcott, and Sean X Sun. “Adhesion dynamics and durotaxis in migrating cells”. In: *Phys. Biol.* 8.1 (2011), p. 015011. DOI: 10.1088/1478-3975/8/1/015011.

[23] Douglas Hanahan and Robert A Weinberg. “The Hallmarks of Cancer”. In: *Cell* 100.1 (2000), pp. 57–70. DOI: 10.1016/s0092-8674(00)81683-9.

[24] G. Wayne Brodland. “How computational models can help unlock biological systems”. In: *Seminars in Cell & Developmental Biology* 47-48 (2015), pp. 62–73. DOI: 10.1016/j.semcdb.2015.07.001.

[25] D Aubry et al. “Mechanical link between durotaxis, cell polarity and anisotropy during cell migration”. In: *Phys. Biol.* 12.2 (2015), p. 026008. DOI: 10.1088/1478-3975/12/2/026008.

[26] R. Allena, M. Scianna, and L. Preziosi. “A Cellular Potts Model of single cell migration in presence of durotaxis”. In: *Mathematical Biosciences* 275 (2016), pp. 57–70. DOI: 10.1016/j.mbs.2016.02.011.

[27] Jan Poleszczuk and Heiko Enderling. “A High-Performance Cellular Automaton Model of Tumor Growth with Dynamically Growing Domains”. In: *AM* 05.01 (2014), pp. 144–152. DOI: 10.4236/am.2014.51017.

[28] Zhihui Wang et al. “Simulating cancer growth with multiscale agent-based modeling”. In: *Seminars in Cancer Biology* 30 (2015), pp. 70–78. DOI: 10.1016/j.semcancer.2014.04.001.

[29] Louise Dyson and Ruth E. Baker. "The importance of volume exclusion in modelling cellular migration". In: *J. Math. Biol.* 71.3 (2014), pp. 691–711. DOI: 10.1007/s00285-014-0829-0.

[30] Patrícia Santos-Oliveira et al. "The Force at the Tip - Modelling Tension and Proliferation in Sprouting Angiogenesis". In: *PLOS Computational Biology* 11.8 (2015). Ed. by Hans Van Oosterwyck, e1004436. DOI: 10.1371/journal.pcbi.1004436.

[31] Maren Freutel et al. "Finite element modeling of soft tissues: Material models, tissue interaction and challenges". In: *Clinical Biomechanics* 29.4 (2014), pp. 363–372. DOI: 10.1016/j.clinbiomech.2014.01.006.

[32] Sara Checa et al. "The emergence of extracellular matrix mechanics and cell traction forces as important regulators of cellular self-organization". In: *Biomechanics and Modeling in Mechanobiology* 14.1 (2014), pp. 1–13. DOI: 10.1007/s10237-014-0581-9.

[33] Roeland M. H. Merks et al. "Contact-Inhibited Chemotaxis in De Novo and Sprouting Blood-Vessel Growth". In: *PLoS Comput Biol* 4.9 (2008). Ed. by Philip E. Bourne, e1000163. DOI: 10.1371/journal.pcbi.1000163.

[34] Marco Scianna, Luca Munaron, and Luigi Preziosi. "A multiscale hybrid approach for vasculogenesis and related potential blocking therapies". In: *Progress in Biophysics and Molecular Biology* 106.2 (2011), pp. 450–462. DOI: 10.1016/j.pbiomolbio.2011.01.004.

[35] Andras Szabo, Erica D. Perryn, and Andras Czirok. "Network Formation of Tissue Cells via Preferential Attraction to Elongated Structures". In: *Phys. Rev. Lett.* 98.3 (2007). DOI: 10.1103/physrevlett.98.038102.

[36] René F. M. van Oers et al. "Mechanical Cell-Matrix Feedback Explains Pairwise and Collective Endothelial Cell Behavior In Vitro". In: *PLoS Comput Biol* 10.8 (2014). Ed. by Anand R. Asthagiri, e1003774. DOI: 10.1371/journal.pcbi.1003774.

[37] Christopher A. Lemmon and Lewis H. Romer. "A Predictive Model of Cell Traction Forces Based on Cell Geometry". In: *Biophysical Journal* 99.9 (2010), pp. L78–L80. DOI: 10.1016/j.bpj.2010.09.024.

[38] G. Beaune et al. "How cells flow in the spreading of cellular aggregates". In: *Proceedings of the National Academy of Sciences* 111.22 (2014), pp. 8055–8060. DOI: 10.1073/pnas.1323788111.

[39] Stephanie Wong, Wei-Hui Guo, and Yu-Li Wang. "Fibroblasts probe substrate rigidity with filopodia extensions before occupying an area". In: *Proceedings of the National Academy of Sciences* 111.48 (2014), pp. 17176–17181. DOI: 10.1073/pnas.1412285111.

[40] Casey M. Kraning-Rush et al. "Microfabricated collagen tracks facilitate single cell metastatic invasion in 3D". In: *Integr. Biol.* 5 (3 2013), pp. 606–616. DOI: 10.1039/C3IB20196A.

[41] M. H. Zaman et al. "Migration of tumor cells in 3D matrices is governed by matrix stiffness along with cell-matrix adhesion and proteolysis". In: *Proceedings of the National Academy of Sciences* 103.29 (2006), pp. 10889–10894. DOI: 10.1073/pnas.0604460103.

[42] Robert W. Style et al. “Traction force microscopy in physics and biology”. In: *Soft Matter* 10.23 (2014), p. 4047. DOI: 10.1039/c4sm00264d.

[43] Clive L. Dym and Irving H. Shames. *Solid Mechanics: A Variational Approach, Augmented Edition*. Springer, 2013. ISBN: 1461460336.

[44] A. J. Davies. *The Finite Element Method: An Introduction with Partial Differential Equations*. Oxford University Press, 2011. ISBN: 0199609136.

[45] R.L. Graham et al. “Dense packings of congruent circles in a circle”. In: *Discrete Mathematics* 181.1-3 (1998), pp. 139–154. DOI: 10.1016/s0012-365x(97)00050-2.

[46] K. M. Welch-Reardon et al. “Angiogenic sprouting is regulated by endothelial cell expression of Slug”. In: *Journal of Cell Science* 127.9 (2014), pp. 2017–2028. DOI: 10.1242/jcs.143420.

[47] Casey M. Kraning-Rush, Joseph P. Califano, and Cynthia A. Reinhart-King. “Cellular Traction Stresses Increase with Increasing Metastatic Potential”. In: *PLoS ONE* 7.2 (2012). Ed. by Elizabeth G. Laird, e32572. DOI: 10.1371/journal.pone.0032572.

[48] Ugo Cavallaro and Gerhard Christofori. “Cell adhesion and signalling by cadherins and Ig-CAMs in cancer”. In: *Nature Reviews Cancer* 4.2 (2004), pp. 118–132. DOI: 10.1038/nrc1276.

[49] Kurt R. Gehlsen, George E. Davis, and P. Sriramarao. “Integrin expression in human melanoma cells with differing invasive and metastatic properties”. In: *Clin Exp Metast* 10.2 (1992), pp. 111–120. DOI: 10.1007/bf00114587.

[50] Shawn P. Carey et al. “Leading malignant cells initiate collective epithelial cell invasion in a three-dimensional heterotypic tumor spheroid model”. In: *Clin Exp Metastasis* 30.5 (2013), pp. 615–630. DOI: 10.1007/s10585-013-9565-x.

[51] J. R. Shewchuk. *An Introduction to the Conjugate Gradient Method Without the Agonizing Pain*. 1994.